TECTONOMETAMORPHIC EVOLUTION OF THE LOWER NAR VALLEY, CENTRAL NEPAL HIMALAYA

by

Tom P. Gleeson
B.Sc., University of Victoria, 2000

A THESIS SUBMITTED IN PARTIAL FULFILLMENT OF THE REQUIREMENTS FOR THE DEGREE OF

MASTER OF SCIENCE

In the Department of Earth Sciences

SIMON FRASER UNIVERSITY

August 2003

APPROVAL

Name: **Tom Gleeson**

Degree: Master of Science

Title of Thesis: Tectonometamorphic evolution of the lower Nar Valley, central Nepal Himalaya

Examining Committee:

Chair: **John Clague**
Professor

Dr. Laurent Godin
Senior Supervisor
Assistant Professor

Dr. Jim Monger
Supervisor
SFU Adjunct Professor

Dr. Dan Marshall
Supervisor
Assistant Professor

Dr. Stephen Johnston
ExternalExaminer
Associate Professor
School of Earth & Ocean Sciences
University of Victoria

Date Approved: August 5, 2003

PARTIAL COPYRIGHT LICENCE

I hereby grant to Simon Fraser University the right to lend my thesis, project or extended essay (the title of which is shown below) to users of the Simon Fraser University Library, and to make partial or single copies only for such users or in response to a request from the library of any other university, or other educational institution, on its own behalf or for one of its users. I further agree that permission for multiple copying of this work for scholarly purposes may be granted by me or the Dean of Graduate Studies. It is understood that copying or publication of this work for financial gain shall not be allowed without my written permission.

Title of Thesis/Project/Extended Essay:

Tectonometamorphic evolution of the lower Nar Valley, central Nepal Himalaya

Author:

(Signature) ______________________

(Name) ______________________

Aug. 13/03

(Date)

ABSTRACT

The Chako gneisses outcrop in the Nar Valley, north of the Annapurna massif in central Nepal. Previous reconnaissance mapping recognised an enigmatic outcropping of the Greater Himalayan sequence, called the Chako Dome, surrounded by rocks correlated with the Tethyan sedimentary sequence. A new, detailed map of the Nar Valley with a significant re-interpretation is presented. The map area is divisible into two different structural levels. The Lower Level is characterised by rock types, high-strain zones with south-verging shear-sense indicators, and high-grade metamorphism which suggest that the Lower Level is part of the Greater Himalayan sequence. The rocks of Upper Level, previously mapped as the sub-greenschist or zeolite facies Tethyan sedimentary sequence, are garnet-bearing schists. Petrography and garnet-biotite thermometry imply the Upper Level equilibrated at amphibolite facies (500-650°C). Amphibolite facies peak metamorphic temperatures suggest that the Upper Level is a previously undescribed component of the Greater Himalayan sequence. Unmetamorphosed sediments of the Tethyan sedimentary sequence structurally overly the Upper Level and are separated by the uppermost fault of the South Tibetan detachment system.

Differences in structural style and possible differences in peak metamorphic grade suggest that each level may have unique early tectonometamorphic history. Upper Level structures suggest it was deformed at considerably higher structural levels. The lack of cross-cutting isograds or temperature constraints from the Lower Level make it impossible to determine if both levels experienced similar peak metamorphic conditions.

The Lower and Upper Levels both experienced D_1 deformation and peak metamorphism before ~20 Ma. The Lower and Upper Levels are juxtaposed along the synmetamorphic Chame detachment at ~20 Ma during retrograde metamorphism. After ~19 Ma, the Phu detachment juxtaposed the unmetamorphosed Tethyan sedimentary sequence above the Lower and Upper Levels. The entire package was folded, after 19 Ma, by a non-cylindrical antiform-synform pair with a ~25 km wavelength.

same-same but different.

-Modern Nepali proverb and MSc. thesis in four words

ACKNOWLEDGEMENTS

This MSc. was a dream project that slid into my hands. So first and foremost I would like to thank Laurent Godin, as senior advisor, for conceiving this project and for offering it to me. Both in the field and at school, Laurent is a hard-working and ethical scientist who enjoys doing quality work and the finer points of life – I hope just a little of this has rubbed off on me.

I also appreciate Dan Marshall, Jim Monger, and Stephen Johnston for being an excellent committee and teaching me much about communicating science. Dan elucidated the path to peak metamorphism and is thanked for the TWEEQU calculations. Jim provided the initial inspiration to skip out of the Cordillera to study in the Himalaya. Stephen is thanked for his thorough editing and questioning.

Numerous people made field work, which ranged from bamboo forests to 5000 m high glaciers, a breeze. Pasang Tamang - guide, master logistician and friend - made everything look easy. Without Pasang, Norbu, Little Pasang, Dawa, Partap and Little Dawa, field work would have been inconceivable. I am grateful to Charlotte Olsen for field assistance. Map making assistance from Audrey Gleeson and Natalie Portelance helped me not get lost.

Along the way I have been inspired and taught by innumerable geologists. A field visit by Mike Searle greatly enhanced this project. For keeping me sane at school, I can thank Pierre Nadeau, my stalwart labmate, John Laughton, Alberto Reyes, Jenn Sabean, Tyler Beatty, Majid Al-Suwaidi, Dan Utting and the rest of the Earth Sciences department. Early geological inspiration, which still keeps me going, came from the Cordilleran crowd of Mitch Mihalynuk, JoAnne Nelson, Stephen Johnston, Kathy Gillis and Larry Diakow.

For keeping me sane and loving life, I thank my family and friends, both close by and far away. Without you the Himalaya might never have been studied (by me at least)!

This project was funded by a NSERC grant to Laurent Godin.

TABLE OF CONTENTS

LIST OF FIGURES

Figure

LIST OF TABLES

Table

CHAPTER 1
INTRODUCTION

Introduction

The metamorphic core of the Himalayan orogen, the Greater Himalayan sequence, is a south-facing wedge of amphibolite-facies rocks (Hodges et al. 1996; Grujic et al. 2002). The Tethyan sedimentary sequence is a lesser metamorphosed sedimentary package, which structurally overlies the Greater Himalayan sequence (Figure 1.1; Searle et al. 1987; Godin 2003). The contact between the metamorphic core and the overlying sedimentary package is a complex transition zone punctuated by north-dipping normal faults of the South Tibetan detachment system (Burchfiel et al. 1992). The evolution of the contact between the metamorphic core and the overlying sedimentary package helps constrain the timing and style of exhumation during orogenesis (Burchfiel and Royden 1985). In many orogens, subsequent deformation and metamorphism or extensive exhumation commonly obscures the contact between the metamorphic core and the overlying sediments (Brown et al. 1986). Studying the contact between the metamorphic core and the overlying sediments in the Himalayan orogen provides insight for the understanding of older orogenic belts.

In the Annapurna region of central Nepal (Figure 1.2), the transition zone between the Greater Himalayan sequence and Tethyan sedimentary sequence has seen many studies at various scales (Colchen et al. 1986; Brown and Nazarchuk 1993; Coleman 1996; Godin et al. 1999a; Searle and Godin 2003). The study area is located in the lower Nar valley where the transition zone between the Greater Himalayan Sequence and the Tethyan sedimentary sequence is well-exposed (Figure 1.3; Searle and Godin 2003). The transition zone was previously interpreted as part of the Tethyan sedimentary sequence but was recently re-interpreted as part of the Greater Himalayan sequence (Colchen et al. 1986; Searle and Godin 2003). The Marsyandi valley, south of the Nar valley, provides a well-studied reference section of the Greater Himalayan sequence (Figure 1.3; Bordet et al. 1975; Colchen et al. 1986; Coleman 1996). Detailed mapping and an integration of lithological, structural and metamorphic data allow tests of whether the rocks outcropping in the lower Nar Valley are part of the Greater Himalayan sequence or the Tethyan sedimentary sequence. Lithological, structural and metamorphic data are then combined with previous age constraints to develop a cohesive tectonometamorphic evolution model for the transition zone from the metamorphic core to the overlying sediments.

The Himalayan Orogen

The Himalayan orogen formed during Tertiary continental collision between the Eurasian and Indian plates. The orogen consists of four major tectonostratigraphic units, all derived from the Indian plate (Figure 1.1A). Each unit is a discrete fault slice bounded by north-dipping Cenozoic fault systems called, from south to north, the Main Frontal thrust, the Main Boundary thrust, the Main Central thrust, and the South Tibetan detachment system (Figure 1.1B). The Main Frontal thrust is the youngest structure associated with Himalayan deformation. Below the Main Frontal thrust is the Indian foreland basin and Indian basement. The lowest thrust slice consists of the Siwalik Formation composed of openly folded, Miocene to Pleistocene synorogenic molasse. The Lesser Himalayan sequence is thrust over this and comprises

Proterozoic to Eocene sedimentary and volcanic rocks, typically penetratively deformed and metamorphosed at zeolite to upper greenschist facies (Hodges 2000). Structurally above the Lesser Himalayan sequence, the Greater Himalayan sequence is carried by the Main Central thrust over the Lesser Himalayan sequence. The Greater Himalayan sequence consists of Proterozoic to Paleozoic sedimentary and granitic rocks, polydeformed and metamorphosed at upper greenschist to upper amphibolite facies (LeFort 1975; Burchfiel et al. 1992; Hodges 2000). Synmetamorphic Miocene leucogranites, including the Manaslu leucogranite and various smaller bodies and dykes, intrude the Greater Himalayan sequence (Searle et al. 1987). The Tethyan sedimentary sequence is structurally higher, and carried on the South Tibetan detachment system, a top-down-to-the-north normal fault system (Burchfiel et al. 1992). It consists of Neoproterozoic to Tertiary sediments deposited on the northern passive margin of the Indian paleocontinent (Searle et al. 1987; Hodges 2000). To the north, the Tethyan sedimentary sequence is bounded by the Indus-Yarlung suture zone, which marks the suture between the Indian subcontinent and Asia (Yin and Harrison 2000, and references therein). This chapter outlines the salient features of: 1) the Greater Himalayan sequence; 2) the Tethyan sedimentary sequence; 3) the South Tibetan detachment system; and 4) the Manaslu leucogranite.

The Indian subcontinent collided with Eurasia during the Late Eocene to Oligocene, altering plate motion and sedimentation regimes and initiating deformation and crustal thickening in the Himalayan and central Asian region (Yin and Harrison 2000, and references therein; Najman et al. 2001). Time constraints for important structural features and farfield effects are controversial and variable along strike (Copeland et al. 1991; Guillot et al. 1999; Hodges 2000). Within the Greater Himalayan sequence, metamorphism occurred in two phases: the Oligocene Eohimalayan amphibolite-facies phase and the dominant Miocene Neohimalayan greenschist to amphibolite-facies phase (Coleman 1996; Vannay and Hodges 1996; Godin et al. 2001). Pre-Miocene folding within the Tethyan sedimentary sequence led to crustal thickening and may have triggered Eohimalayan and/or Neohimalayan metamorphism (Godin et al. 1999b; Weismayr and Grasemann 2002). The South Tibetan detachment system is a complex family of north-dipping normal faults commonly with older, ductile strands and younger, brittle strands (Burchfiel et al. 1992; Hodges et al. 1996; Searle and Godin 2003). The ductile component of the South Tibetan detachment system was active in the Miocene, coeval with the Main Central thrust (Hodges et al. 1996; Godin et al. 2001).

Greater Himalayan sequence

The Proterozoic to Lower Paleozoic Greater Himalayan sequence outcrops almost continuously along the entire length of the Himalayan orogen (Figure 1.1). In the Annapurna region, the Greater Himalayan sequence is traditionally divided into three lithologicaly distinct packages: Formation I, Formation II, and Formation III (Figure 1.2A; Colchen et al. 1986). Searle and Godin (2003) used the term 'Unit' rather than 'Formation' because these "Formations" are interlayered, metamorphosed and deformed (Figure 1.2C). Unit I consists of interlayered kyanite-sillimanite grade pelitic schist, gneiss and migmatite. Unit II is a heterolithic package of calc-silicate gneiss, marble and psammitic schist and gneiss. The dominant and most distinctive lithology of Unit II is a calc-silicate gneiss with dark diopside-hornblende-biotite rich layers and light quartz-feldspar-calcite rich layers (Coleman 1996; Hodges et al. 1996). Unit III is a distinctive augen orthogneiss, characterized by 1-4 cm feldspar augens, that has been dated isotopically at 500-480 Ma (Hodges et al. 1996; Godin et al. 2001). Searle and Godin (2003) suggest that the lower Tethyan sedimentary sequence is a possible protolith for the meta-sedimentary rocks of the Greater Himalayan sequence.

Syn-metamorphic to post-metamorphic deformation within the Greater Himalayan sequence produced a homoclinal north-eastward dipping transposition foliation and meso- to microscopic south-verging structures (Brunel 1986; Hodges et al. 1996). Folds at all scales are tight to isoclinal, and are commonly asymmetric with a south vergence. Microstructural shear-sense indicators include mantled porphyroblasts, mica fish, C' planes and S-C fabrics (Grujic et al. 1996; Grasemann et al. 1999). Quartz c-axis measurements suggest complex flow kinematics within the Greater Himalayan sequence with zones of both south directed general-shear and pure-shear (Bouchez and Pêcher 1981; Grujic et al. 1996; Grasemann et al. 1999; Law 2003).

In the Marsyandi valley, microstructural shear-sense indicators have only been studied within the Chame detachment (Figure 1.2). S-C fabrics and C' shear bands suggest top-down to the north sense of motion (Coleman 1996).

In the central Himalaya, the metamorphic evolution of the Greater Himalayan sequence is divided into an early, enigmatic Eohimalayan event and a dominant Neohimalayan event. Evidence for the Eohimalayan event include petrographic observations (Hodges et al. 1988), Ar-Ar ages (Vannay and Hodges 1996), U-Pb monazite ages and zircon lower intercept ages (Hodges et al. 1996; Godin et al. 2001). Eohimalayan geothermobarometry suggest peak temperature of 600°± 50° C and maximum burial depth of 30-40 km (Vannay and Hodges 1996). The Neohimalayan event is responsible for the predominant metamorphic signature within the Greater Himalayan sequence. Above the Main Central thrust, the Greater Himalayan sequence is characterized by an inverted Neohimalayan isograd sequence (Hubbard and Harrison 1989; Stephenson et al. 2001). Temperatures typically increase structurally upwards from 550°C to 750°C (Hubbard and Harrison 1989; Vannay and Grasemann 2001). The highest grade metamorphic assemblage, sillimanite and K-feldspar, and the highest metamorphic equilibrium temperature of ~750°C, are found 1 to 5 km above the Main Central thrust (Hubbard and Harrison 1989; Vannay and Grasemann 2001). The upper part of the Greater Himalayan sequence exhibits a normal isograd sequence. In the upper section, metamorphic equilibrium temperatures are constant or decrease slightly with increasing structural levels. Peak metamorphic pressure, indicating burial up to ~30 km, does not vary with temperature but rather remains constant or decreases up-structure in the Greater Himalayan sequence (Hubbard and Harrison 1989; Vannay and Grasemann 2001).

In the Marsyandi valley, the Greater Himalayan sequence displays an Eohimalayan thermal history (Coleman and Hodges 1998) and inverted Neohimalayan metamorphic isograds (LeFort 1975). However the absolute metamorphic conditions of the Greater Himalayan sequence in the Marsyandi valley are poorly unconstrained. Calcite-dolomite solvus thermometry of the upper Greater Himalayan sequence suggests peak metamorphic temperatures of >510°C (Schneider and Masch 1993).

Tethyan sedimentary sequence

The Paleozoic to Mesozoic Tethyan sedimentary sequence structurally overlies the Greater Himalayan sequence (Figure 1.1B and 1.2). In the Annapurna region, the lowest exposed Tethyan sedimentary sequence unit is the Sanctuary-Pi Formation, a 500m package of heterogeneous biotite-muscovite schist and metamorphosed sandstone (Colchen et al. 1986; Gradstein et al. 1992; Garzanti 1999). In the Marsyandi valley of the Annapurna region, the lowest exposed Tethyan sedimentary sequence formations are the Ordovician carbonate sequence of the Annapurna-Yellow Formation and the Nilgiri Formation (Colchen et al. 1986). The Annapurna-Yellow Formation is a 800m thick psammite with muscovite and phlogopite defining the foliation and giving the formation its pale yellow patina (Bordet et al. 1975). The Nilgiri Formation is a 1500m thick, massive, brachiopod-rich, unmetamorphosed limestone (Bordet et al. 1975). The North Face quartzite forms the upper 400m of the Nilgiri Formation and consists of calcareous arkoses and siltstones, with rare primary sedimentary features, such as cross bedding (Coleman 1996). Overlying the Ordovician sequence are shales and gritty limestones of the Silurian-Devonian Sombre Formation and black shales and massive limestones of the Permo-Carboniferous Lake Tilicho and Thini Chu Formations (Colchen et al. 1986). The massive Triassic to Jurassic carbonate sequences of the Thini, Jomsom, and Bagung Formations are overlain by the Late Jurassic Lupra Formation shales (Gradstein et al. 1992). The overlying Cretaceous stratigraphy is not exposed in Marsyandi valley.

The deformation and metamorphism of the Tethyan sedimentary sequence distinguish it from the Greater Himalayan sequence. The Tethyan sedimentary sequence commonly exhibits multiple folding phases with oblique and readily differentiable fabrics (Godin 2003). The lowermost Tethyan sedimentary sequence is metamorphosed to zeolite or lowest greenschist grade with a foliation typically outlined by muscovite. The metamorphic grade decreases upwards to the epizone-archizone boundary (Garzanti et al. 1994).

South Tibetan detachment system

The nature of the contact between the Greater Himalayan sequence and the Tethyan sedimentary sequence is complex. Early workers interpreted the contact as conformable because they found similar rock types and metamorphic grades on either side (Gansser 1964). However, the contact marks a break in structural styles. Detailed mapping has revealed families of top-down-to-the-north high strain zones, called the South Tibetan detachment system, near or at the upper boundary of the Greater Himalayan sequence (Figure 1.1; Burchfiel et al. 1992; Brown and Nazarchuk 1993; Godin et al. 1999a). Recent work suggests that the South Tibetan detachment system consists of a lower, ductile strand and an upper, brittle strand (Table 1.1; Hodges et al. 1996, Searle & Godin 2003). The ductile segment is older (~22 Ma), and is coeval with Neohimalayan metamorphism. The brittle segments are younger (<19 Ma) and define a metamorphic break between the Greater Himalayan sequence and Tethyan sedimentary sequence.

In the Marsyandi valley, the Chame detachment forms part of the ductile segment of the South Tibetan detachment system (Figure 1.2; Coleman 1996). The Chame detachment juxtaposes Unit II of the Greater Himalayan sequence in its footwall against the metamorphosed Nilgiri Formation in its hanging wall.

The peak metamorphic temperature inferred from prograde assemblages and calcite-dolomite geothermometry are indiscernible across the contact (Schneider and Masch 1993). Structurally above the Chame detachment, subsequent brittle strands of the South Tibetan detachment system, such as the Phu detachment, developed between 19 Ma and 14 Ma, and juxtapose rocks of different metamorphic grade (Searle and Godin 2003).

Manaslu Leucogranite

The well studied Manaslu leucogranite is a peraluminous granite. Cross-cutting relationships and contact metamorphism originally suggested the Manaslu leucogranite intrudes the Greater Himalayan sequence and the Tethyan sedimentary sequence (LeFort 1975; Guillot et al. 1994; Harrison et al. 1999; LeFort et al. 1999). However, recent mapping suggests the South Tibetan detachment system deforms the top of the Manaslu pluton, implying that the pluton is cut by the South Tibetan detachment system rather than cross-cutting it (Searle and Godin 2003). U-Th monazite ages suggest two main phases of crystallization at 22.9 ± 0.6 Ma and 19.3 ± 0.3 Ma (Harrison et al. 1999).

Previous work in the study area

The lower Nar valley study area is located north of the Marsyandi valley in central Nepal (Figure 1.3). The lower Nar valley was closed to foreigners until 1992 with restricted access until 2002. The mouth of the Nar is reached after a 3-4 day trek up the Marsyandi valley (Figure 1.3). The map area is broken into the forested, lower Phu Khola (khola is Nepali for river) with sparse outcrop and the upper Phu, Nar and Labse Kholas which are above tree line and offer >60% outcrop.

The valley was first mapped at 1:200 000 scale by French workers (Bordet et al. 1975; Colchen et al. 1986). Bordet et al. (1975) identified the Chako dome, a 2 km wide structure of gneiss, correlated with the Greater Himalayan sequence, surrounded by the lower grade Tethyan sedimentary sequence (Figure 1.2A). Subsequent regional work concentrated on the more accessible Marsyandi valley (Schneider and Masch 1993; Coleman 1996).

A systematic study of prograde mineral assemblages and calcite-dolomite solvus thermometry from Marsyandi valley samples illustrated that the peak metamorphic temperatures decrease systematically from the upper Greater Himalayan sequence to the upper Paleozoic members of the Tethyan sedimentary sequence (Schneider and Masch 1993). Metamorphic continuity across the contact between the Greater Himalayan sequence and the Tethyan sedimentary sequence suggests this is a synmetamorphic structure (Figure 1.2B).

Coleman (1996) interpreted the contact between the Greater Himalayan sequence Unit II and the Nilgiri Formation as the sole segment of the South Tibetan detachment system in the Marsyandi valley (Figure 1.2B and 1.3; Table 1.1). This interpretation was based on top-down to the north shear sense indicators and contrasting thermal history in the footwall and hanging wall (Coleman 1998; Coleman and Hodges 1998). If the Chame detachment is interpreted as the sole segment of the South Tibetan detachment system, then the Chako dome is in the hanging wall of the South Tibetan detachment system.

Reconnaissance mapping by Godin (2001) partly elucidated the structural complexities of the Chako dome, recognizing pervasive internal and bounding south-verging structures. The map area was separated into three structural levels, each consisting of two to three lithologies, with internal and bounding high strain zones (Godin 2001). Searle & Godin (2003) recently acknowledged the metamorphic grade of these rocks, previously considered to be part of the Tethyan sedimentary sequence, and re-interpreted them as Lower Paleozoic components of the Greater Himalayan sequence (Figure 1.2C). Searle and Godin (2003) also interpreted the Phu detachment as the upper, younger brittle South Tibetan detachment fault and the Chame detachment as the lower, older ductile South Tibetan detachment fault (Table 1.1). This interpretation implies that the entire Chako dome is positioned within the Greater Himalayan sequence, in the footwall of the upper, South Tibetan detachment fault.

This study

The lower Nar valley field area extends from the homoclinal Greater Himalayan sequence in the Marsyandi valley to the unmetamorphosed Tethyan sedimentary sequence in the upper Nar Valley. The goal of this study is to constrain the structural and metamorphic evolution of the Chako dome area by addressing the following questions:

1) What are the Chako Dome rocks, and what tectonostratigraphic unit(s) do they correlate with? Two important correlations are addressed. Do the Chako gneisses correlate with the Greater Himalayan sequence? Can the rock units overlying the Chako

gneisses be correlated with the Tethyan sedimentary sequence? Field data collected during two mapping seasons provide three important tests of correlation: rock type, structural style, and metamorphic assemblage. Detailed laboratory study of metamorphic assemblages and thermal constraints on peak metamorphic conditions strengthen field-based correlations.

2) What is the geometry and relative timing that characterises the structures of the Chako dome rocks? The structural evolution of the domal structure is constrained by both outcrop and microstructural observations.

3) What constraints can be derived for the metamorphic evolution of the Chako dome rocks? The metamorphic evolution is constrained by petrography and thermometry. A detailed petrographic survey of the study area is used to constrain the timing and constituents of metamorphic assemblages. Scanning electron microscope analysis is used to identify accessory minerals. Garnet-biotite thermometry is employed to constrain peak metamorphic temperatures.

Table 1.1. Comparison of characteristics of the upper and lower strands of the South Tibetan detachment system in the Annapurna Region. Shear sense indicators suggest predominantly top-to-north movement.

UPPER BRITTLE STRAND	1. Annapurna detachment (Godin et al. 1999b, 2001)	2. Machhapuchare detachment (Hodges et al. 1996)	3. Bhratang/Phu detachment (Searle & Godin 2003)	4. Upper Dudh Khola detachment?
Shear sense indicators	?	S-C fabrics, C' bands, folds	None except low-angle, brittle faults	?
Timing (Ma)	~14	19-14	<19-18	?
Metamorphic contrast: **hanging wall** / **footwall**	zeolite / greenschist-amphibolite	greenschist / amphibolite facies	zeolite / greenschist-amphibolite	?
Thickness	Multiple fault zones of <3 m	?	350-400 m	?
LOWER DUCTILE STRAND	5. Annapurna detachment (Godin et al. 1999b, 2001)	6. Deorali detachment (Hodges et al. 1996)	7. Chame detachment (Coleman 1996, 1998)	8. Dudh Khola detachment (Coleman 1996)
Shear sense indicators	S-C fabrics, C' bands, folds, rotated dyke array, quartz petrofabrics	None (obscured by Modi Khola shear zone)	S-C fabrics, C' bands	none
Timing (Ma)	~22	~22.5	24-18	>21
Metamorphic contrast **hanging wall** / **footwall**	Bt + Ms / Ky + Sil + Grt	None	None	?
Thickness	1500 m	300 m	1200 m	300 m

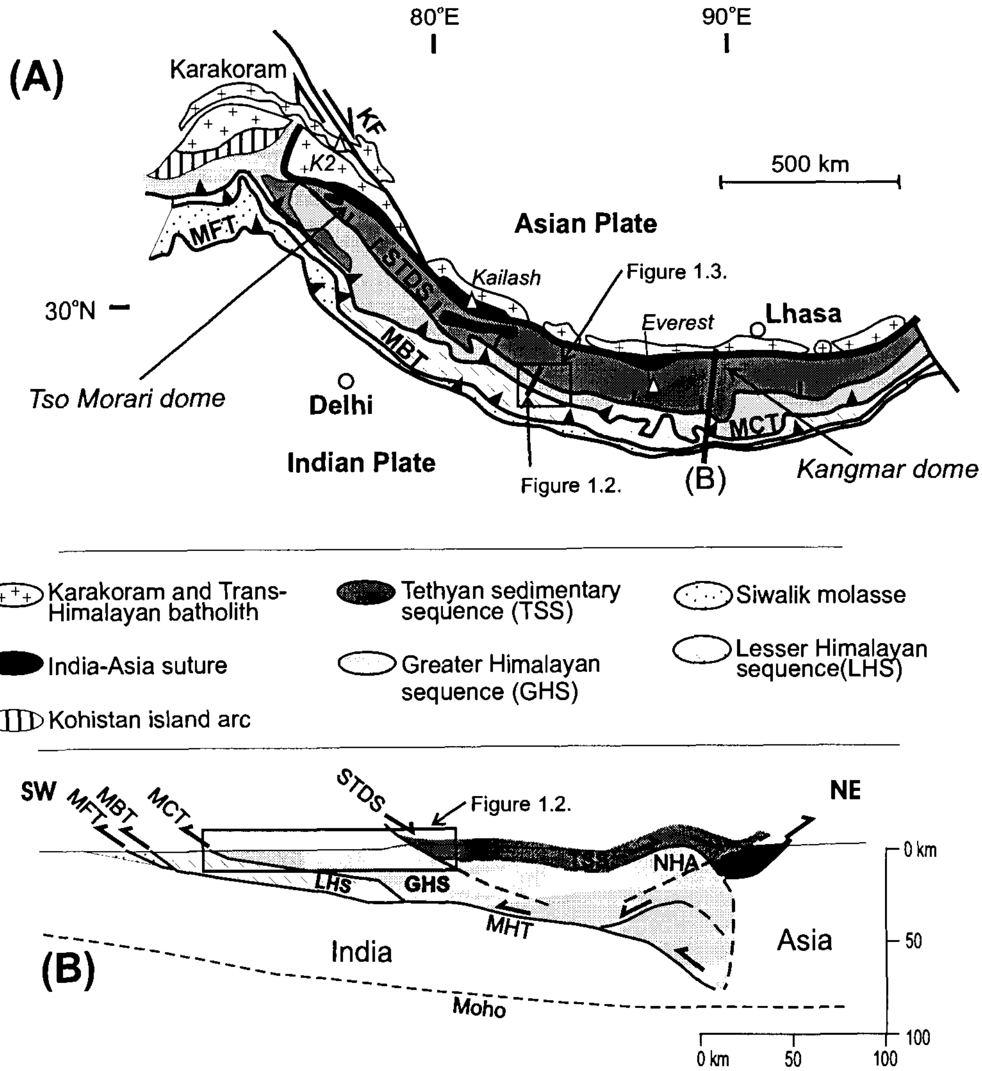

Figure 1.1. Himalayan tectonostratigraphy. (A) Simplified orogen-scale map highlighting major features including the Karakoram fault (KF), the Main Frontal thrust (MFT), the Main Boundary thrust (MBT), the Main Central thrust (MCT), and the South Tibetan detachment system (STDS). (B) Simplified crustal-scale structure of the central Himalaya (90°E) interpreted from INDEPTH reflection data and surficial geology showing fault structure and Main Himalayan thrust (MHT) and North Himalayan anticline (NHA; modified from Hauck et al. 1998).

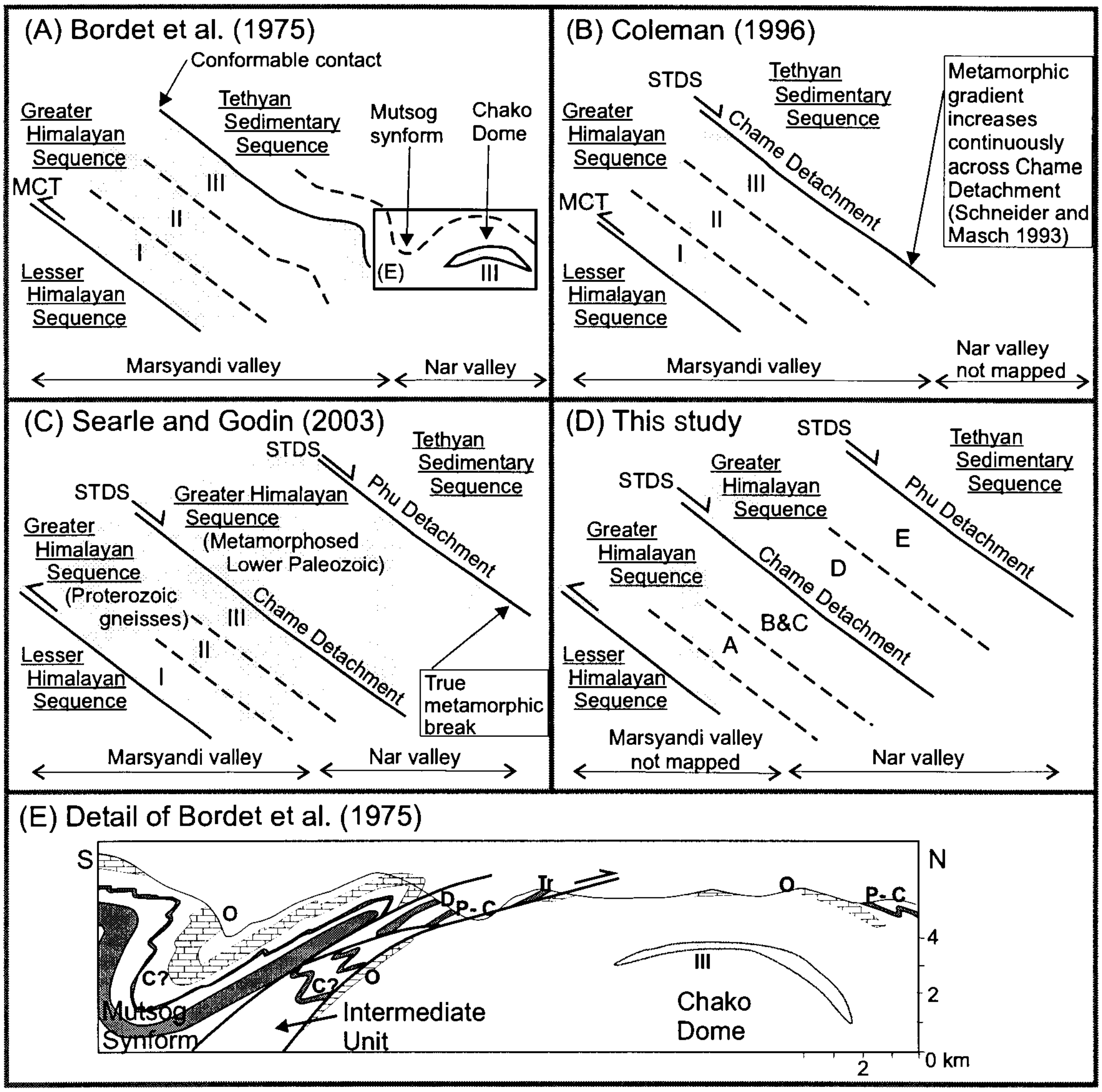

Figure 1.2. Interpretations and nomenclature of previous workers and this study summarized by schematic cross sections (A-D). In (A)-(D), all views look west and unit thicknesses are not to scale. The bounding structures of the Greater Himalayan sequence are the Main Central thrust (MCT) and the South Tibetan detachment system (STDS). The Greater Himalayan sequence is shown in light grey and subdivided into Unit I, II, and III by Bordet et al. (1975) and Coleman (1996). Searle and Godin (2003) interpreted rocks above the Chame detachment as part fo the Greater Himalayan Sequence. Unit I does not outcrop in the Nar valley; in this study the Greater Himalayan sequence above Unit I is subdivided into Units A, B, C, D, and E. (E) Detail of previous interpretation of the Nar Valley (after Bordet et al. 1975). Tethyan sedimentary sequence units are dark grey except the Ordovocian (O) Nilgiri marker horizon which is in the boxed pattern. C, Cambrian; D, Devonian; P-C, Permo-Carboniferous; Tr, Triassic. Unit III of the Greater Himalayan sequence is shown in light grey.

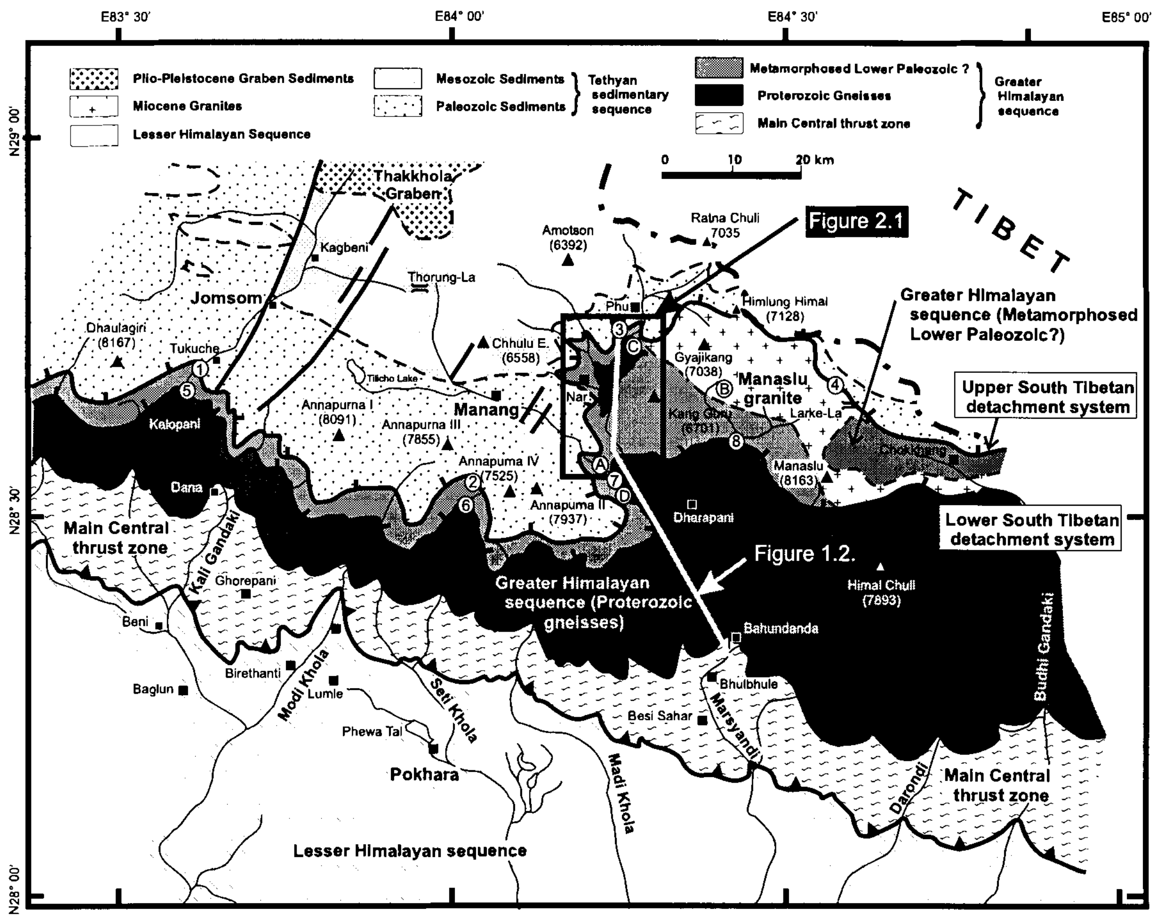

Figure 1.3. Regional geology map (modified from Searle and Godin 2003). Numbers on the lower and upper strands of the South Tibetan detachment system refer to the various localities outlined in Table 1.1. Sample locations for age constrains from other authors: (A) Ar-Ar phologopite cooling ages (Coleman and Hodges 1998); (B) U-Th monazite ages from the Manaslu pluton (Guillot et al. 1994; Harrison et al. 1999); (C) a U-Pb age of a dyke (L.Godin and R.Parrish pers.comm. 2002); and (D) a U-Pb age of an undeformed dyke (Coleman 1998). See Chapter 5 for further description of age constraints.

CHAPTER 2
LOCAL GEOLOGY

Introduction

The Nar Valley map area is divisible into two sub-Tethyan structural levels, based on lithology, metamorphic grade, and deformation history (Figures 2.1 and 2.2). The Lower Level is an interlayered package of three rock types: a hornblende-biotite schist Unit A; a biotite schist Unit B; and an augen gneiss Unit C. Lower Level units are intruded by numerous pegmatitic dykes. The Upper Level consists of a micaceous marble Unit D and a garnet phyllite-schist Unit E. The unmetamorphosed Tethyan sedimentary sequence overlies the Upper Level. This chapter focuses on the lithology, thickness, mineralogy and texture of each unit of the Lower and Upper Levels. Rock descriptions are used to discuss Upper and Lower Level correlations and protoliths. The overlying Tethyan sedimentary sequence units and the contacts within and between levels are also introduced. Mineral abbreviations follow Kretz (1983).

Lower Level

Unit A: Hornblende-biotite schist

Two indistinguishable layers of pistachio to dark green weathering hornblende-biotite schist comprise Unit A and are separated by a layer of Unit B biotite schist (Figure 2.2; Figure 2.3A). Unit A consists of a ~2000 m thick upper layer and a >600 m thick lower layer. As described below, Unit B is interpreted as a deformed equivalent of Unit C. Unit B and C are interpreted as an Ordovician granite intruding Unit A before Himalayan deformation. Similar relationships of granitic augen gneiss intruding schist is documented elsewhere in the Greater Himalayan Sequence (Godin et al. 2001).

The primary metamorphic assemblage consists of Cpx + Qtz + Pl ± Ttn ± Ep ± Kfs with more retrogressed samples containing the assemblage Qtz + Hbl + Bt ± Pl ± Chl ± Ttn ± Ep ± Cpx (Figure 2.2; Appendix A.1, A.2). Well-layered, transposed foliations at lower structural levels grade into massive, mottled schist at higher structural levels. Primary and retrogressed layers are interlayered at millimetre- to centimetre-scale in the well-layered schist. The massive schist is characterized by anastomosing foliations devoid of compositional interlayering. Variations in the mineralogy and texture of Unit A are controlled by retrograde replacement and transposition by high strain zones.

Unit B: Biotite schist

Unit B is a banded black and white biotite schist (Figure 2.3B) containing pods of Unit C augen gneiss. Unit B is a ~650 m layer flanked above and below by Unit A schist. The mineral assemblage consists of Bt + Qtz + Ttn ± Hbl ± Pl with rare Chl ± Kfs ± Ms. The foliation of this mica-rich lithology is outlined by biotite, and locally by proto-gneissic compositional layering.

Unit C: Augen gneiss

Unit C is a coarse grained, white granitic augen gneiss (Figure 2.3C). Three pods of this deformed granite are found within Unit B (Figure 2.1). The pod above Chako is ~200 m thick and the two pods near Dzonum are 5-10 m thick. The gneiss contains conspicuous 2-5 centimetre long feldspar porphyroclasts within a Pl + Qtz + Bt + Ttn ± Kfs ± Chl ± Hbl ± Ms assemblage.

Pegmatitic dykes

Coarse-grained to pegmatitic layer-parallel and cross-cutting dykes intrude all three units of the Lower Level. Dykes are most common in the Unit B biotite schist, and locally comprise up to 40% of Unit B volumetrically. The mineral assemblage of the pegmatitic dykes consists of Qtz + Pl + Hbl ± Kfs ± Ms. Dykes display synkinematic intrusive relationships, as described in Chapter 3.

Upper Level

Unit D: Phlogopite marble

Unit D is a yellow-grey weathering biotite to phlogopite marble. It is a 500 m thick recrystallised, unfossiliferous marble containing the mineral assemblage Cal + Qtz + Bt + Ms ± Chl, with uncommon Grt ± Hbl ± Pl (Figure 2.3D; 2.3E). The foliation is outlined by moderately well developed phlogopite and biotite partings with recrystallised intrafolial calcite.

Unit E: Garnet-biotite phyllite and schist

Unit E consists of silver to black phyllite and schist. It is a 500 m thick unit lying above Unit D. The mineral assemblage Bt + Qtz + Ms + Grt + Pl ± Chl and Hbl ± Ep ± Ttn characterizes this unit. Garnet porphyroblasts (1-3 mm) differentiate this unit from others (Figure 2.3F). Unit E is interlayered at the decimetre-scale with phyllite and schist layers and locally gneiss layers near Chhacha. In all cases the foliation is outlined by biotite and muscovite.

Poorly preserved fossils within Unit E provide depositional and age constraints. The phyllite locally contains 2-3 millimetre echinoderms (photo in Chapter 3), which restrict deposition of Unit E to a Paleozoic back lagoon to lower slope environment (T. Beatty pers. comm. 2003).

Tethyan sedimentary sequence

Within the map area, the Tethyan sedimentary sequence consists of two unmetamorphosed units above the Upper Level. The Upper Triassic Thini Formation is a >200 m thick, black to grey shale (Colchen et al. 1986). The Lower Jurassic Jomsom Formation is a ~500 m thick, grey to dun micritic limestone (Colchen et al. 1986). A mountain-scale anticline overturns this stratigraphy (Bordet et al. 1975; Colchen et al. 1986).

Bedding is preserved within the Tethyan sedimentary sequence (Table B.1). Bedding is outlined in the Thini Formation by millimetre-scale silty layers. Rare, 10 centimetre thick marly sandstone layers in the Jomsom Formation outline bedding.

Contacts

Contacts within the Lower Level are transposed, high strain zones with millimetre- to centimetre-scale interlayers of each unit (Table 2.1; Figure 2.2). The contacts are 50-100 m thick except the contact between Unit B and Unit C, which is 1-2 m thick. The contacts may be transposed stratigraphy. Contacts are positioned where the two interlayered units are volumetrically equal.

Contacts within the Upper Level are sharp rather than transposed high strain zones. The contact between Unit D and Unit E displays centimetre-scale interlayering, suggesting that it may be an original stratigraphic contact.

Discussion

Lithological correlation of the Lower and Upper Levels

The Lower Level was mapped as a 'gneiss à plaquettes' and 'migmatites,' equivalent to Units II and III, respectively, of the Greater Himalayan sequence (Bordet et al. 1975). In a subsequent compilation, a small outcropping of the 'migmatite' was correlated with Greater Himalayan sequence Unit III, and the surrounding units were considered Tethyan sedimentary sequence (Colchen et al. 1986). Godin (2001) described the Lower Level as calc-silicate and garnet-biotite-sillimanite augen gneiss.

The Lower Level units directly correlate with the Greater Himalayan sequence units exposed in the Marsyandi valley. Unit A correlates with Unit II calc-silicate because of the similarities in mineralogy, texture and outcrop appearance (Bordet et al. 1975). Unit II of the Greater Himalayan sequence is called a calc-silicate schist because of the presence of calcium minerals, such as diopside (Bordet et al. 1975; Colchen et al. 1986; Godin 2001). However, the term hornblende-biotite schist is preferred for Unit A because of the paucity of carbonate minerals. Unit B biotite schist correlates with the biotite-rich 'gneiss à plaquettes' described by Bordet et al. (1975) based on mineralogy and texture. The biotite schist was previously incorporated with the distinct augen gneiss as part of Unit III (Colchen et al. 1986; Coleman 1996). However, Unit B is a distinct map unit and is thus considered a separate lithology. Unit C correlates, based on mineralogy and texture, with the Unit III granitic augen gneiss found in the Marsyandi valley near Chame (Colchen et al. 1986; Godin 2001).

The Upper Level was mapped as the Ordovician Annapurna-Yellow, Pi and Nilgiri Formations (Bordet et al. 1975; Colchen et al. 1986). However, the Upper Level units consist of metamorphic rocks, and are described in this study using metamorphic nomenclature, rather than the formation nomenclature which assumes knowledge of the unmetamorphosed protoliths.

The Upper Level, previously described as Tethyan sedimentary sequence, is interpreted as a previously undescribed part of the Greater Himalayan sequence because Units D and E are medium-grade metamorphic rocks. The metamorphic study described in Chapter 4 further constrains the metamorphic conditions of the Upper Level.

Protoliths of the Lower and Upper Levels

Mineralogy and texture suggest the protoliths for Units A, D and E are sedimentary rocks. The Paleozoic Tethyan sedimentary sequence is the probable protolith for the Greater Himalayan sequence meta-sediments because it is the closest sedimentary package (L.Godin pers. comm. 2003). Searle and Godin (2003) suggest the protoliths for Units A and D are the Annapurna-Yellow Formation and the Nilgiri Formation, respectively. The Annapurna-Yellow Formation is an 800 m thick psammite. The bulk composition of the Annapurna-Yellow Formation suggests it is an appropriate protolith for the siliceous Unit A. However, if the Annapurna-Yellow Formation is the protolith for Unit A, it was structurally duplicated because Unit A is 2000 m thick. The

1500 m thick Nilgiri Formation is the only major limestone in the Lower Paleozoic Tethyan sedimentary sequence. The Nilgiri Formation has an appropriate bulk composition to be the protolith of Unit D. However, Unit D is only 500 m thick. The protolith of Unit E is previously unconstrained. Echinoderms within the 500 m thick Unit E preclude a Proterozoic or unfossiliferous protolith. The 1200 m thick Sombre Formation overlies the Nilgiri Formation (Bordet et al. 1975; Colchen et al. 1986). The Sombre Formation, a graptolite and tentaculite-rich shale, is a possible protolith for Unit E. Echinoderms may not have been reported for the Sombre Formation because they are a common fossils that do not provide age constraints (T.Beatty pers. comm. 2003). For each Lower Level unit, the unit thickness is not consistent with the protolith thickness suggesting that subsequent deformation affected unit thicknesses.

Mineralogy and texture suggest the protoliths for Units B and C are igneous rocks based on mineralogy and texture. Unit C correlates with Unit III, which is interpreted as an Ordovician granite intruding the Greater Himalayan Sequence (Godin et al. 2001). Unit B and C outcrop together in the Nar valley. In a 1-2 m contact above Chako, Unit C augen gneiss progressively becomes finer grained, grading into Unit B (L.Godin pers. comm. 2002; Table 2.1). Outcrop patterns, grain size and mineralogical similarities suggest that Unit B is a high stain equivalent of Unit C.

Table 2.1. Contact characteristics.

Contact	Interlayered or sharp	Thickness (metre)	Best exposure
Unit A - Unit B	Interlayered	50-100	Above Chako or Dzonum
Unit B - Unit C	Interlayered	1-2	Above Chako
Unit A - Unit D	Interlayered	~75	North of Kyang
Unit D - Unit E	Interlayered	~10	Above Namya
Unit E- Jomsom Formation	Sharp	<1	Above Nar

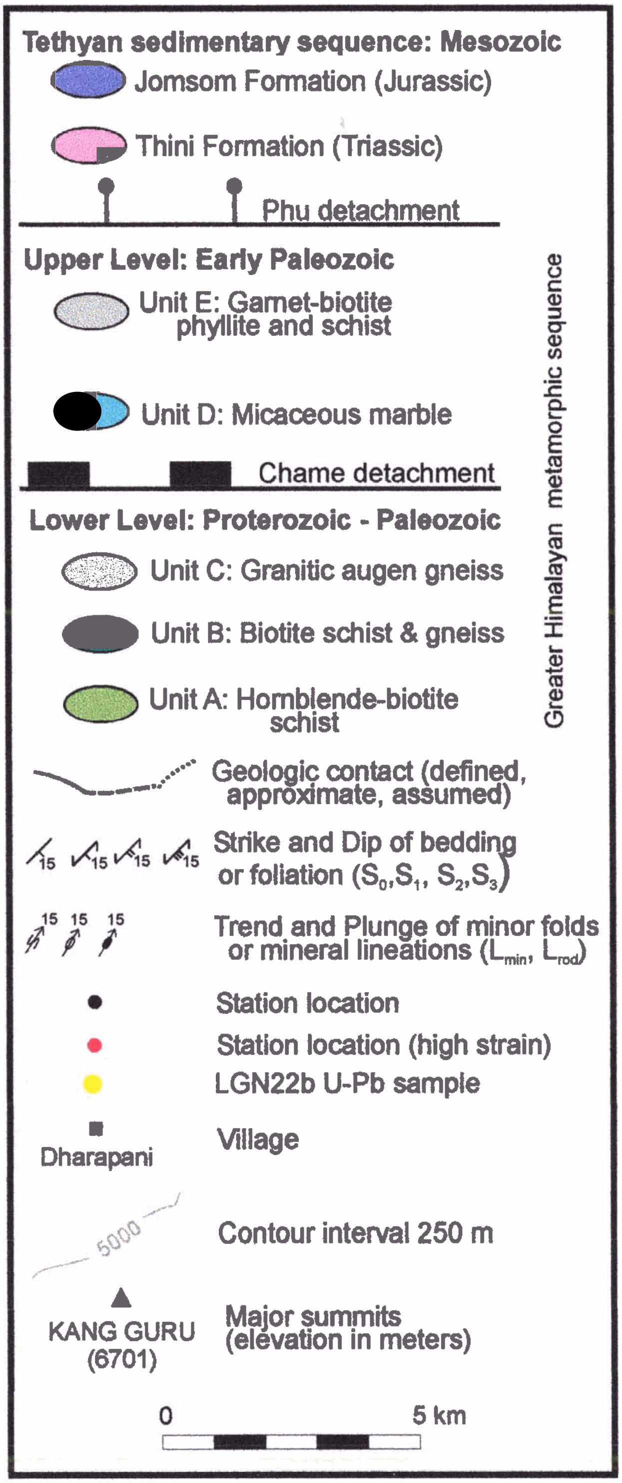

Figure 2.1. Geologic map of the lower Nar valley. Lines of section A-A' and B-B' are shown in Figure 3.3 and 3.5.

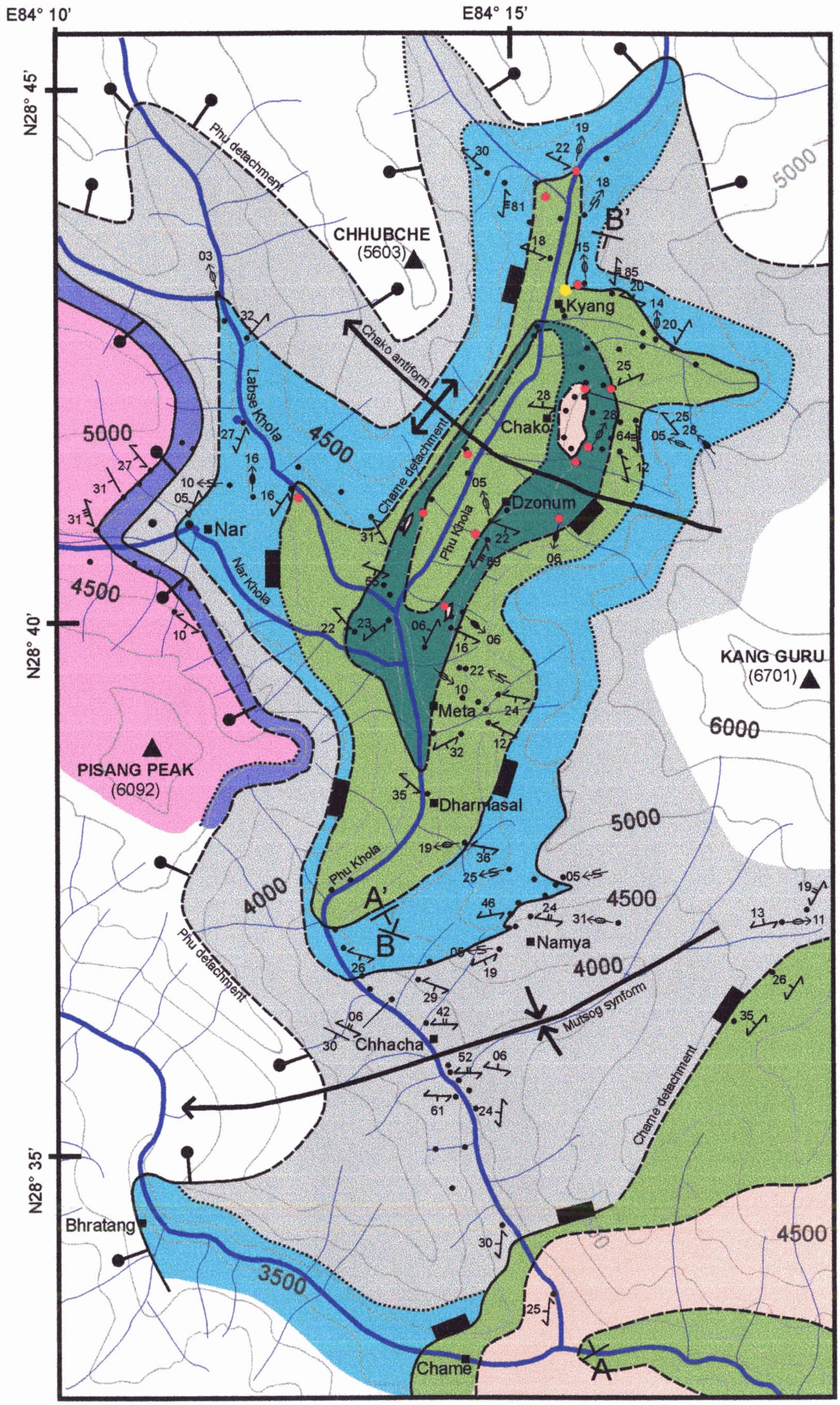
E84° 10'
E84° 15'
N28° 45'
N28° 40'
N28° 35'
Phu detachment
CHHUBCHE
(5603)
Chako antiform
Chame detachment
Labse Khola
Nar Khola
Phu Khola
B'
Kyang
Chako
Dzonum
Nar
Meta
Dharmasal
PISANG PEAK
(6092)
KANG GURU
(6701)
A'
B
Namya
Chhacha
Mutsog synform
Chame detachment
Bhratang
Chame
A
5000
4500
4000
3500
6000

25b

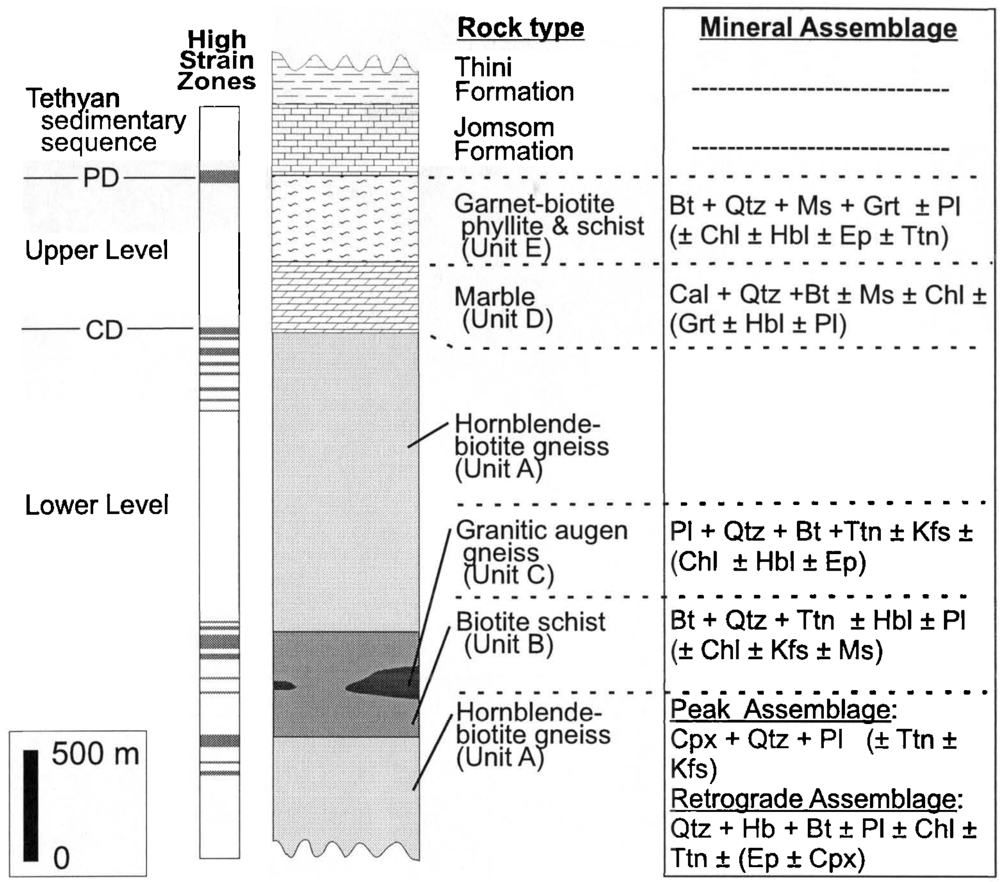

Figure 2.2. Structural section showing position and thickness of each unit and high strain zones. High strain zones display a well developed foliation (typically transposed) and a weakly to moderated developed mineral lineation. Important structural boundaries are the Chame detachment (CD) and the Phu detachment (PD).

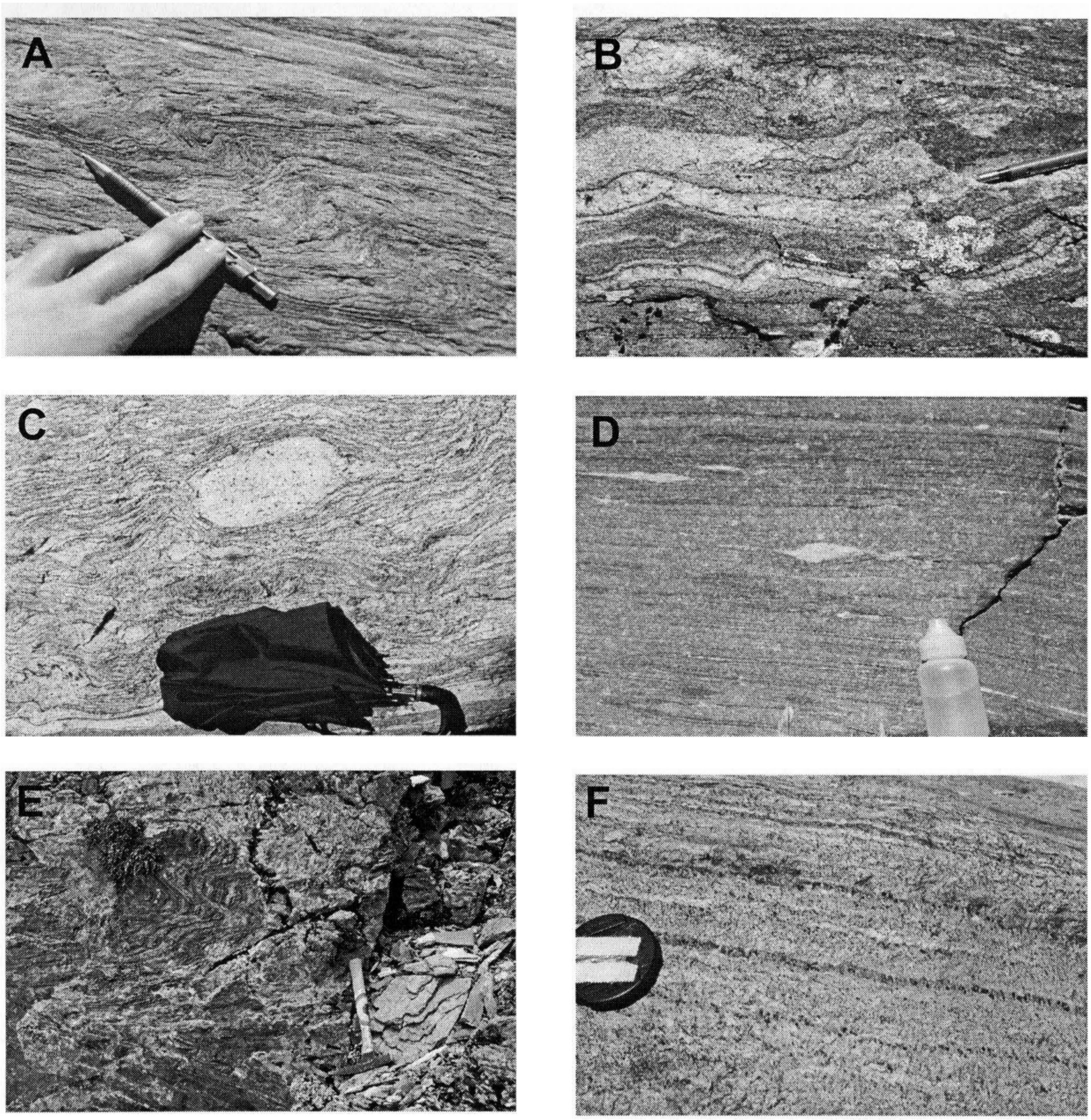

Figure 2.3. Outcrop appearance of each unit. A) banded Unit A hornblende-biotite schist; B) biotite schist Unit B with layer parallel dykelets; C) Unit C granitic augen gneiss; D) strained Unit D micaceous marble; E) folded Unit D micaceous marble; F) Unit E garnet schist. Pencil is 15 cm length; umbrella is 25 cm length; bottle is 9 cm length; hammer is 20 cm length; lens cap diameter is 6 cm.

CHAPTER 3
STRUCTURAL GEOLOGY

Introduction

There are four generations of structures in the lower Nar valley: an early, foliation-producing event, D_1 ; a folding and locally foliation-producing event, D_2; crustal-scale folding, D_3; and a late, brittle event, D_4. As described in Chapter 2, the area is divisible into Lower and Upper Levels. The levels are separated by a high strain zone. Differences in D_1 and D_2 features suggest that the different levels may have been separated during the first two phases of deformation. First, D_1 and D_2 features in the Lower Level are described and differentiated using the subscript 'L' for lower (*i.e.* D_{1L}). Second, D_1 and D_2 features in the Upper Level are described and differentiated using the subscript 'U' for upper (*i.e.* D_{1U}). D_3 deformation is not assigned to a specific level because Lower and Upper Levels are affected. The only observed D_4 feature is a locally developed spaced brittle cleavage. The structural history of each of the levels and the intermediary contact are discussed. Field structural measurements are provided in Table B.1.

Sense of shear indicators are observed at the outcrop-scale on a plane perpendicular to foliation and parallel to the elongation lineation (Hanmer and Passchier 1991). At a regional scale, mineral lineations are too dispersed to define a systematic sense of shear plane. For kinematic analysis, the following assumptions are made: the flow plane parallels the shear plane and the elongation lineation marks the flow direction (Passchier and Trouw 1998).

Lower Level (D_{1L} and D_{2L})

Within the Lower Level, S_{1L} is the main planar fabric and a product of D_{1L} deformation (Figure 2.1; Table B.1). S_{1L} is a penetrative, spaced schistosity of aligned cleavage domain minerals (Bt ± Hbl ± Ms; Figure 3.1; Table B.2), compositional layering within Unit A hornblende-biotite schist, and a weak quartz grain shape foliation and quartz ribbons within Unit C augen gneiss (Figure 3.2A). No folds or lineations are observed in association with S_{1L} fabric development.

D_{2L} is partitioned into 1-100 m thick high strains zones with intermediary lower strain zones (Figure 3.1). High strain zones are characterised by a transposition foliation, mineral lineation, and by shear sense indicators. High strain zones are concentrated at contacts, suggesting that lithological, and possibly rheological, contrasts control their localization. Between high strain zones, the rocks exhibit anastomosing fabrics, and lack mineral lineations and shear sense indicators.

The first characteristic of the D_{2L} high strain zones is transposition. D_{2L} deformation is interpreted to transpose S_{1L} fabrics into a S_{2L} transposition fabric for three reasons. First, rock units and different S_{1L} fabrics are interlayered. Second, shear sense indicators, described below, deform S_{1L} fabrics and suggest a simple shear component to deformation. Third, macroscopic folds, which are common between high strain zones are not present.

The second characteristic of the high strain zones is the development of mineral lineations on S_{2L} surfaces. Quartz mineral rods are rare mineral elongation lineations (L_{rod} on Figures 3.1; 3.3). Mineral aggregate lineations of biotite and hornblende are more common (L_{min} on Figures 3.1; 3.3). Both types of lineation show a large dispersal of trends with a mean orientation plunging 14° towards N333° (Figure 3.3G). However, the limited data set precludes statistical interpretation (Table B.1). No lineation cross-cutting relationships were observed, suggesting all the lineations are one generation. Lineations are interpreted as coeval to D_{2L} because the lineations are only developed in D_{2L} high strain zones. Different mechanisms may have caused the dispersal of lineations. First, a component of pure shear, as described below, would decrease the alignment of lineations. Second, the different lineations may have resulted from different processes. For example, quartz rods form parallel to the axis of extension but also form parallel to fold hinges as a product of open space filling (Davis and Reynolds 1996). Third, lineations may have been variably rotated during transposition.

The third characteristic of the high strain zones is shear sense indicators. High strain zones exhibit both asymmetric and symmetric D_{2L} structures which affect S_{1L} fabrics. Asymmetric shear sense indicators suggesting simple shear are described first, followed by a description of symmetric features suggesting pure shear. Asymmetric features that verge south include well developed sigma porphyroblasts (Figure 3.4A) and poorly developed C-S fabrics and C' shear bands. Pervasive folds are open to closed, centimetre-scale to metre-scale and overturned to the south (Figure 3.4B; Figure 3.5C, sketch 3 and 5) with fold hinge lines plunging 08° towards N300° (Figure 3.3F). The folds are elliptical to teardrop shaped, suggesting ductile flow during folding. Common symmetric structures are alpha tails on diopside porphyroblast and feldspar porphyroclasts. Symmetric strain shadows are also common.

Between high strain zones, asymmetric folds and composite fabrics are developed. The asymmetric folds between high strain zones have a similar style and orientation to the asymmetric folds within high strain zones. The asymmetric folds between high strain zones, with an amplitude up to 20 m, are larger than the asymmetric folds within the high strain zones (Figure 3.4B). Unit B biotite schist shows a composite fabric defined by biotite grains. To test whether the composite fabric is symmetric or asymmetric, the orientation of the biotite long axis relative to the compositional layering was measured (n=312; Figure 3.2B). The orientation is asymmetric with grains preferentially oriented top-down-to-the-northwest (Figure 3.2B). The composite biotite fabric can not be linked with observable C-S fabrics and has two possible interpretations. The oblique foliation may represent a hybrid of the instantaneous and finite strain ellipse suggesting south-directed deformation (Hanmer 1984; Davis and Reynolds 1996). Alternatively, the oblique foliation may represent a poorly developed S_{2L} axial planar cleavage.

Pegmatite dykes

Two generations of pegmatitic dykes intrude the Lower Level: a layer-parallel generation, and a cross-cutting, south-dipping generation. The first generation is boudinaged and does not cut across S_{1L} fabrics. The second generation cuts across S_{1L} fabrics at high angles and consistently dips to the south. The consistent dip of the cross-cutting dykes is interpreted to reflect the extensional field of the strain ellipse, suggesting south-directed deformation. At an outcrop-scale, complex intrusive relationships suggest the second generation is synkinematic to D_{2L} deformation (Figure 3.4D). It is commonly observed that a single dyke cuts across S_{1L}, is layer-parallel to S_{1L} and is also folded by F_{2L} folds. Furthermore, apophyses of the same dyke cut across the same F_{2L} folds. The age of the second generation of dykes is thus interpreted as the minimum age of D_{1L} deformation and the maximum age of D_{2L} deformation (~20 Ma; L.Godin pers. comm. 2003).

Contact between levels in the Nar valley

In the lower Nar valley, the contact between the Lower and Upper Levels is a high strain zone exposed at three localities. At each locality, the zone is characterised by a moderately developed transposition foliation with a mineral aggregate lineation. In the south, near Dharmasal, the contact between the Lower and Upper Level displays decimetre-scale to outcrop-scale, north-verging F_2 asymmetric folds (Figure 3.5C, sketch 2). In the west, below Nar, the contact displays symmetric structures, including 1-3 centimetre porphyroblasts with complex and symmetric tails (Figure 3.4C). In the north, near Kyang, the contact displays a variety of D_2 shear-sense indicators, including asymmetric folds and boudinaged cross-cutting dykes in which the boudin train progressively rotate south towards the flow plane (Figure 3.5C, sketch 5). Within one boudin train, an individual boudin displays drag folds, indicating 180° rotation to the south (Figure 3.4E). Well developed C-S fabrics provide additional, microstructural evidence for south verging, non-coaxial deformation (Figure 3.2C).

D_2 deformation within the contact between the Lower and Upper Levels is interpreted as coeval with D_{2L}: it is a high strain zone with the same characteristics as the D_{2L} high strain zones (transposition, mineral lineation and shear sense indicators); the dykes cross-cut S_1 fabrics and are deformed by D_2 structures like the second generation of dykes and D_{2L} structures; the dykes are absent from the Upper Level.

Upper Level (D_{1U} and D_{2U})

Within the Upper Level, S_{1U} is the main planar fabric (Figure 2.1; Table B.1). Within Unit D micaceous marble, S_{1U} is defined by aligned muscovite ± biotite grains (Figure 3.1) and a weak calcite grain shape foliation. Unit E is texturally variable from phyllite to schist to, locally, gneiss. The continuous to spaced foliation of Unit E is defined by muscovite ± biotite. No folds or lineations were observed in association with S_{1U} fabric development.

The phyllitic S_{1U} cleavage is overgrown by syntectonic garnets. Sub-euhedral to euhedral, 1-3 millimetre garnets preserve the S_{1U} cleavage as inclusion trails. Garnet growth is interpreted as having been coeval with the growth of the S_{1U} phyllitic cleavage based on: the direct continuity between the inclusion trails and the cleavage outside the porphyroblast; and the curvature of inclusion trails which is evidence for porphyroblast modification during growth (Figure 3.2D). The curved inclusion trail and cleavage outside the porphyroblast suggest southward rotation relative to the cleavage. The southward rotating kinematic interpretation is supported by strain caps (Passchier and Trouw 1998) in the upper-north and lower-south corners of the garnets (Figure 3.2D&E).

In the Upper Level, D_{2U} deformation is characterised by asymmetric folds, and the development of S_{2U} axial planar cleavage and hinge-parallel mineral lineations. The folds are open to closed, centimetre- to metre-scale (Figure 3.4F) and overturned to the south with a mean fold hinge plunging 07° towards N278° (Figure 3.3D). Upper Level folds exhibit angular hinge zones and chevron fold shapes, especially in Unit E, suggesting that they formed at higher structural levels than Lower Level folds. S_{2U} foliation, a crenulation cleavage developed axial planar to F_{2U} folds (Figure 3.5C, sketch 1), dips north and is defined by aligned biotite and muscovite (Figure 3.3D; 3.2F). Biotite and muscovite mineral aggregates are a mineral lineation with a mean orientation plunging 03° towards N271° (L_{min} on Figure 3.1; 3.3E). The mineral lineations are quite dispersed. However, Upper Level mineral lineations are considered coeval to D_{2U} deformation because their orientations are similar to F_{2U} fold axis (Figure 3.3D) and to rare S_{1U}-S_{2U} intersection lineations (Table B.1).

D_3 deformation

Lower and Upper Levels are equally deformed by a pair of megascopic folds that control the outcrop pattern (Figure 3.1) and the S_1 orientations (Figure 3.3B&C). This pair of folds was previously described as the Mutsog synform in the south and as the Chako dome in the north (Bordet et al. 1975; Coleman 1996). The term Chako antiform is preferred over the Chako dome because there are no east-dipping foliations to suggest the northern structure is a dome. The orientations of fold axes are well constrained with the pi fold axis of S_{1L} and S_{1U} foliations. The hinge of the Mutsog synform plunges 10° towards N272° (Figure 3.3B). The Chako antiform is oblique to the Mutsog synform with a hinge plunging 08° towards N303° (Figure 3.3C). Cross-section and map constraints suggest both folds are upright, open folds (Figure 3.5C). The amplitude (~4 km) and wavelength (~25 km) of the Mutsog synform-Chako antiform implies crustal scale folding. Crustal-scale folding is considered D_3 deformation since it folds D_2 structures (i.e. the contact between levels) and locally rotates S_{2U} fabrics in the core of the Mutsog synform.

D_4 deformation

D_{2L} and D_{2U} features are deformed by a locally developed brittle spaced S_4 cleavage. This cleavage is spaced on millimetre- to centimetre-scale and has minor (<1 centimetre) offset. The cleavage is oriented north-south with a steep dip (Figure 3.3H). Near Dharmasal, north-verging F_{2L} folds are cross cut by a localized southwest-dipping, brittle fault with minor (<1m) offset.

Discussion

Comparing Lower and Upper Levels

Various D_1 features differentiate the Lower and Upper Levels. The Lower Level has a S_{1L} schistosity with 1-5 millimetre cleavage spacing. The Upper Level S_{1U} exhibits textural variability from phyllite with continuous cleavage to schist with >2 millimetre cleavage spacing (Table B.2). Additionally, D_{1U} is characterised by southward rotated synkinematic garnets, whereas D_{1L} is devoid of sense of shear microstructures.

D_2 features further differentiate the Lower and Upper Levels. In the Lower Level, D_{2L} strain is partitioned into distinct, transposed high strain zones, while in the Upper Level D_{2U} strain is not. South-verging asymmetric folds characterise both levels. However ductile flow folds characterise the Lower Level while chevron to cuspate folds characterise the Upper Level. Additionally, a S_{2L} axial planar cleavage differentiates the Upper Level from the Lower Level.

The style of folding and the lack of transposed high strain zones suggest that the Upper Level was deformed at higher structural levels than the Lower Level and that deformation may not be coeval in those two structural levels. The Upper Level is presently juxtaposed on the Lower Level. If the Lower and Upper Levels were deformed at different structural levels, it is unclear if both levels are part of the Greater Himalayan sequence, as suggested in Chapter 2, and how they were juxtaposed.

Structural Correlation of the Lower and Upper Levels

Both the Greater Himalayan sequence and the Tethyan sedimentary sequence exhibit a characteristic structural history, which can be used to test the correlations discussed in Chapter 2. The upper Greater Himalayan sequence is characterised by two phases of deformation. The only commonly observed D_1 feature is a S_1 schistosity (Schneider and Masch 1993; Coleman 1996). D_2 deformation is characterised by non-coaxial high strain zones with predominantly south-verging asymmetry (Coleman 1996; Grujic et al. 1996; Godin et al. 1999a; Vannay and Grasemann 2001; Law 2003). The Tethyan sedimentary sequence exhibits multiple folding phases with oblique and readily differentiable fabrics and geometries (Godin 2003).

The structures of Lower and Upper Levels can be compared to the structural histories of the Greater Himalayan sequence and the Tethyan sedimentary sequence. The structural history of the Lower Level (an early foliation overprinted by non-coaxial high strain zones) exhibits the characteristic structural history of the Greater Himalayan sequence, supporting the correlation of these units. The Upper Level exhibits a different structural history, suggesting it may not correlate with the Greater Himalayan sequence. However, the Upper Level also does not exhibit the poly-phase folding characteristic of the Tethyan sedimentary sequence (Godin 2003). If the previous tentative correlation of the Upper Level with the Greater Himalayan sequence is robust, the different structural history of the Upper Level, suggests that different components of the Greater Himalayan sequence may have different structural histories.

Chame detachment

North of Kyang in the lower Nar valley, the contact between the Lower and Upper Levels is a high strain zone with south-verging sense of shear indicators. If the correlations outlined in Chapter 2 are correct, the contact between the Lower and Upper Levels in the Marsyandi valley is the Chame detachment, a 1200 m wide high strain zone, exhibiting top-down to north sense of shear (Coleman 1996).

Therefore, the Lower and Upper Level contact displays a north-verging sense of shear at the southern locality (Chame) and a south-verging sense of shear at the northern locality (Kyang). Where exposed between the two localities, the contact displays inconclusive shear sense indicators. An explanation of the change in vergence is that the contact does not represent the same structural horizon (i.e. faulting along the contact removed the north-verging section in the north). Alternatively, the south-verging structures at the contact could be the result of a later overprinting thrust.

The Upper Level may have been emplaced upon the Lower Level along the high strain zone between the Lower and Upper Levels. This would juxtapose the two levels which may have been deformed at different structural levels. As described above, D_2 deformation in the contact between levels is interpreted as coeval to D_{2L}. Between Chame and Chhacha, the hanging wall lithology of the Chame detachment changes from Unit E to Unit D. Cross-section and map constraints suggest that the Chame detachment cuts down to the north through Unit E (Figure 3.5C).

Crustal-scale folding and brittle faulting

D_3 is a later crustal scale folding event which controls regional S_1 orientations and outcrop patterns (Schneider and Masch 1993; Coleman 1996). The D_3 folds are of a similar style and scale as other post-metamorphic folds described in the in the Himalaya by Searle et al. (1992) and Grujic et al. (2002). Late, crustal-scale folds have not been previously documented in central Nepal.

The spaced S_4 cleavage is similar to other N-S steeply-dipping spaced cleavage, observed in the Marsyandi valley and in the neighbouring Kali Gandaki valley (Coleman and Hodges 1995; Godin 2003). The S_4 cleavage may be kinematically linked to the Thakkhola graben, and could mark the development of E-W extension of the southern Tibetan Plateau (Coleman and Hodges 1995).

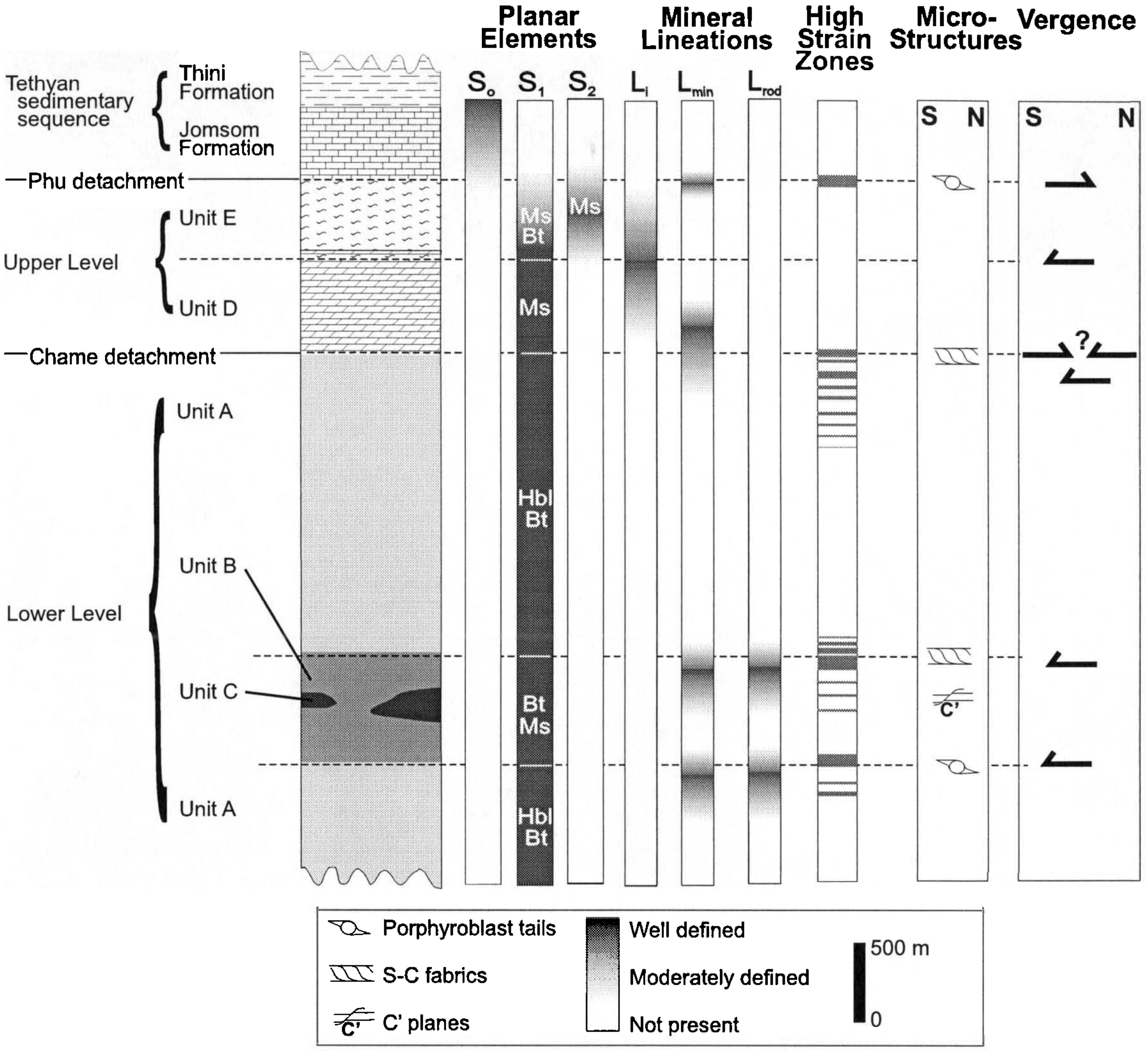

- Figure 3.1. Summary of the microstructures, planar and linear features at different structural levels. High strain zones contain a well developed planar fabric and a weak to moderate lineation. Mesostructures (shown in Figure 4.2) and microstructures (located within high strain zones) together give sense of vergence. Dominant phase of fabric definition at different structural levels are noted with mineral abbreviations after Kretz (1983). L_i, intersection lineation of S_1 and S_2; L_{min}, mineral aggregate lineation; L_{rod}, mineral rod lineation.

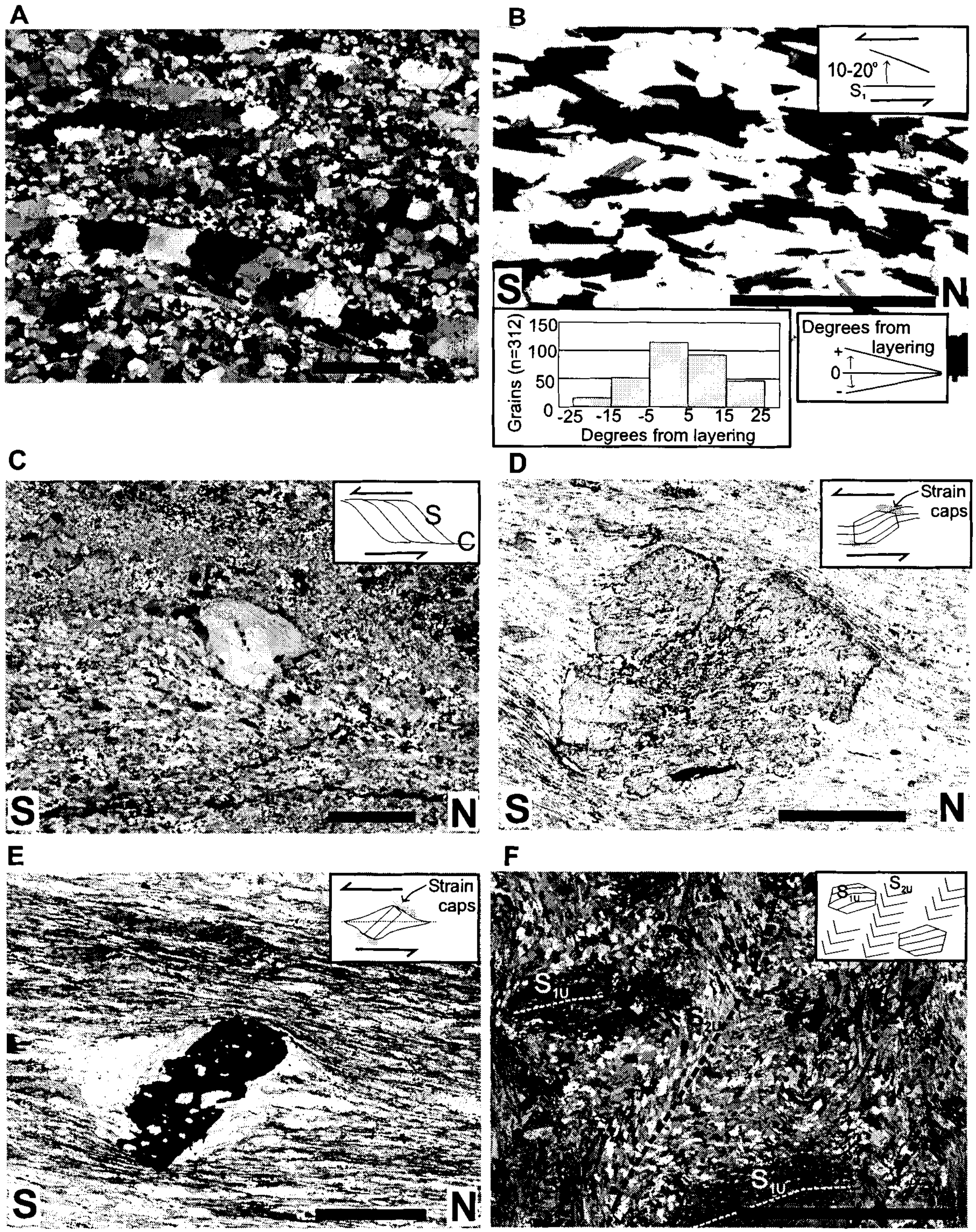

Figure 3.2. Thin section microstructures with geometric and kinematic interpretations. A) quartz ribbons in Unit C; B) biotite composite fabric in Unit B; note histogram of biotite long axes orientation relative to compositional layering; C) moderately developed S-C fabrics in Unit D micaceous marble; D) rotated garnet porphyroblast in Unit E ; E) opaque (replaced echinoderm?) in Unit E; F) S_1 and S_2 fabrics developed in Unit E. All scales are 2 mm. Thin sections A and F are not oriented.

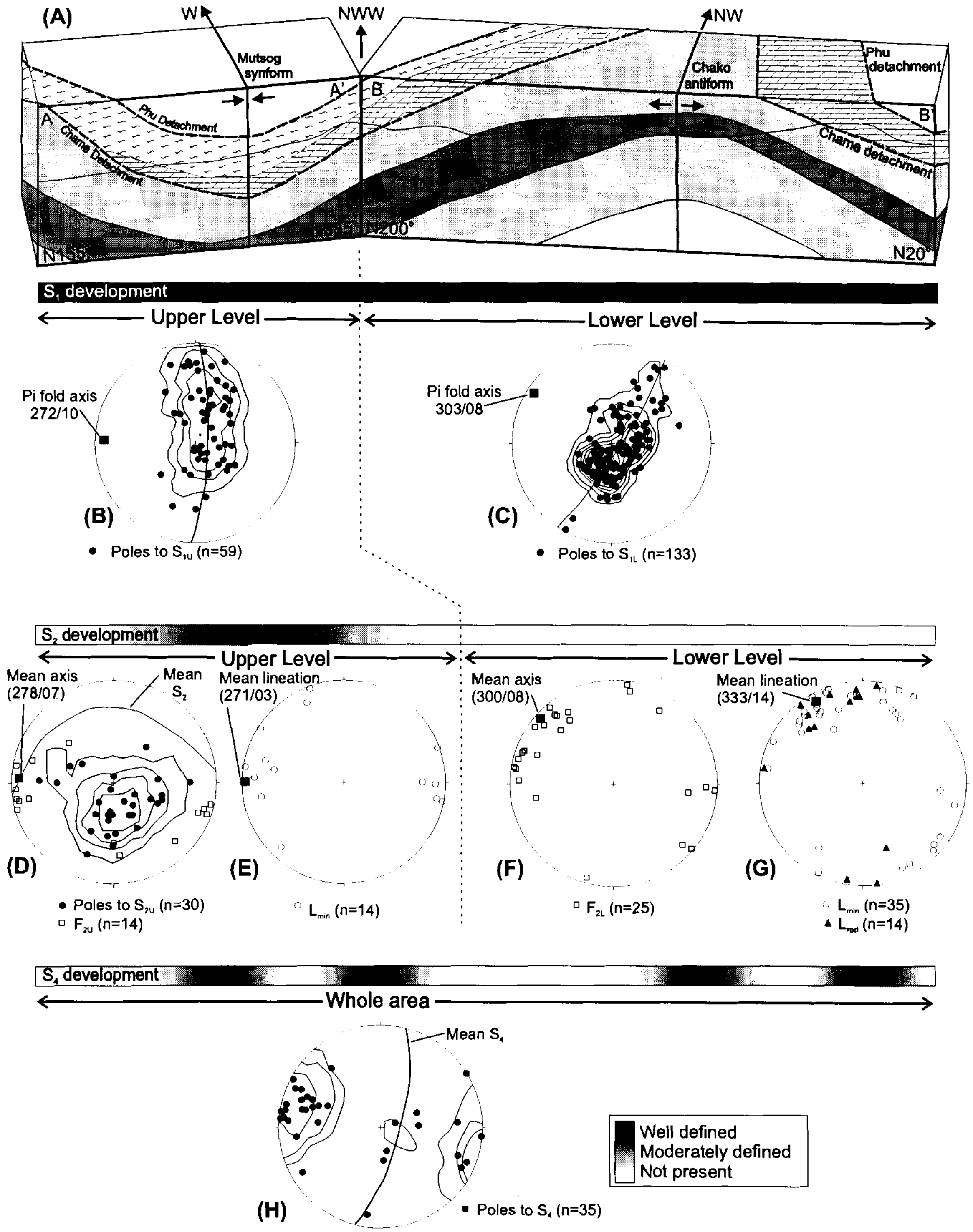

Figure 3.3. A) Composite block diagram of two oblique blocks, looking west, showing down plunge view of the Mutsog synform in the south and the Chako antiform in the north, along the line outlined in Figure 2.1. Length and height same as Figure 3.2. Symbols of lithologies after Figure 3.1. Section parallel location and intensity of fabric development for each phase shown by darkness within each thick bars. Planar features plotted with 2 sigma uncertainty. For the Lower Level, S_{1L} and S_{2L} are parallel and undifferentiated. For the Upper Level, S_{1U} and S_{2U} are oblique and differentiated. Fold axis calculated as mean eigenvectors of F_{2L} and F_{2U} axes or pi poles of S_1 fabrics. Equal area stereonets.

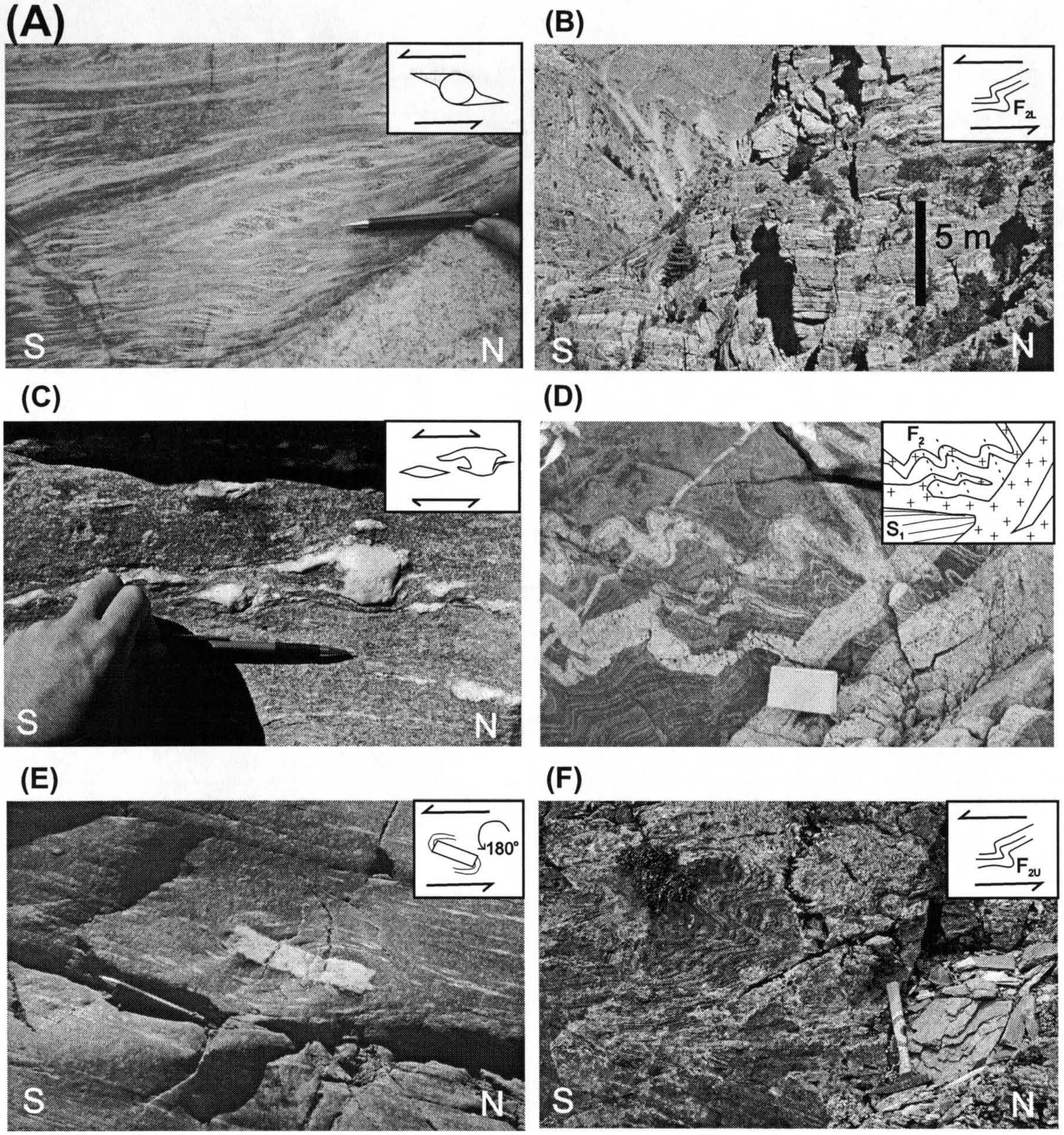

Figure 3.4. Outcrop appearance of mesostructures; all views looking west except D which is unoriented. A) sigma porhyroblasts in Unit A horneblende-biotite schist (photo by L.Godin); B) asymmetric folds in Unit B biotite schist; C) complex and symmetric porphyroblasts at Lower-Upper Level contact near Nar village; D) synkinematic dyke relationships in Unit B near Meta; E) rotated boudin at Lower-Upper Level contact north of Kyang village; F) asymmetric folds within Unit D micaceous marble. Pencil and book are 15 cm length; hammer is 40 cm length; .

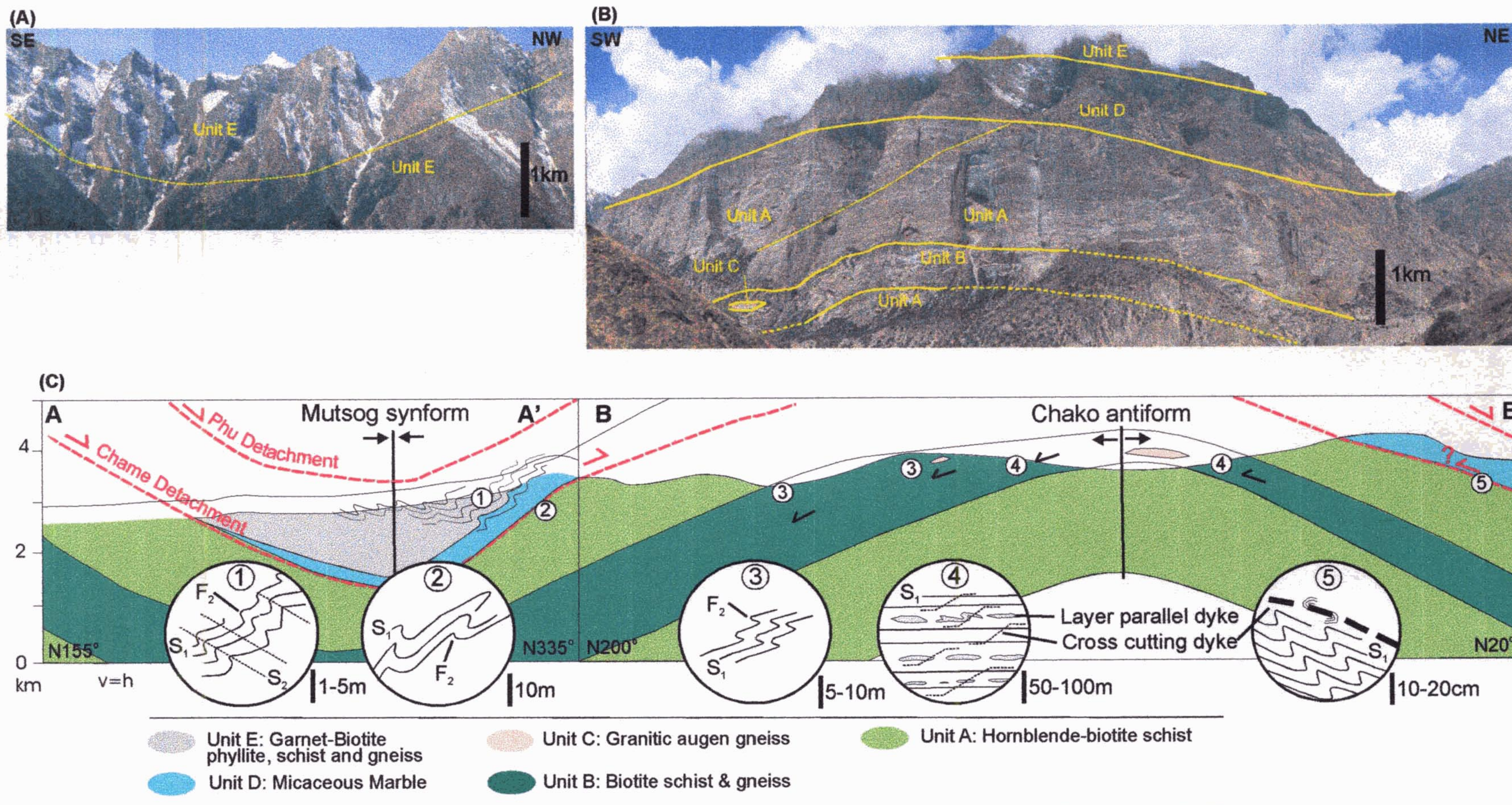

Figure 3.5. Crustal-scale antiform-synform pair and meso-scale D_2 features. A) Mustsog synform with Upper Level rock units in the core; looking south-west from Nayma village towards approximate line of A-A' section; B) Chako antiform with Lower Level rock units in the core; looking northwest from above Chako village towards approximate line of B-B' section; C) composite cross-section (located on Figure 2.1) showing D_3 crustal scale folds and outcrop scale D_2 features in inset circles; note scale of each observation.

CHAPTER 4
METAMORPHIC GEOLOGY

Introduction

The metamorphic evolution of the lower Nar Valley map area is divisible into a peak metamorphic event (M_1) and a retrograde event (M_2). Petrographic constraints on Lower Level metamorphism (M_{1L} and M_{2L}) are presented followed by constraints on Upper Level metamorphism (M_{1U} and M_{2U}). Thermal constraints derived from garnet-biotite thermometry are used constrain peak metamorphic temperatures (Appendix C). Constraints on peak and retrograde metamorphism are discussed and compared with the Greater Himalayan sequence in central Nepal.

Lower Level (M_{1L} and M_{2L})

Metamorphic observations for the Lower Level are based primarily on Unit A (Figure 4.1). The M_{1L} peak metamorphic assemblage consists of Cpx + Qtz + Pl ± Ttn ± Kfs (Figure 4.1). Clinopyroxene, described in the field as diopside, is subprismatic to prismatic. The presence of clinopyroxene may indicate high-grade metamorphism, but the incomplete mineral assemblage precludes thermobarometric studies. The lack of garnet may be controlled by bulk composition constraints or a lower concentration of water (Yardley 1991).

Unit A samples exhibit <5% to 100% replacement of clinopyroxene by retrograde metamorphic minerals (M_{2L}). Incipient replacement of clinopyroxene by hornblende and biotite occurs along fractures. In moderately replaced samples, hornblende and/or biotite enclose the remnant clinopyroxene grains (Figure 4.2A). In completely replaced samples, biotite surrounds hornblende, suggesting that biotite is the final retrograde phase (Figure 4.2B). The M_{2L} assemblage of hornblende and biotite is thus interpreted to have resulted from retrograde metamorphism.

Upper Level (M_{1U} and M_{2U})

Upper Level petrographic constraints are based on Unit E garnet-biotite phyllite and schist. The M_{1U} metamorphic assemblage of Unit E consists of Bt + Qtz + Ms + Grt ± Pl ± Chl. Unit E consists of two distinct textural variants, phyllite and schist. The M_{1U} assemblage of garnet, biotite and muscovite suggests upper greenschist or lower amphibolite facies (Yardley 1991).

Both phyllite and schist are characterised by garnet porphyroblasts. The garnets from within the Unit E phyllite do not display growth zones. The garnets from within the Unit E schist display two distinct growth zones: an inclusion-poor core and an inclusion-rich rim. Within the schist, S_{1U} is folded by S_{2U} crenulation cleavage. The garnets from the schist are considered coeval with the garnets in the phyllite because they display similar curved inclusion trails and they overgrow the same fabric within the same unit. Therefore, all the garnets within Unit E are syntectonic to D_{1U}.

Biotite pseudomorphing garnet grains are interpreted as M_{2U} retrograde metamorphism (Figure 4.2C). Within the same sample, prismatic, unbent, non-undulose biotite and muscovite outlines the S_{2U} crenulation cleavage (Figure 4.5F). Garnet retrogression was thus synchronous to the development of crenulation cleavage. The M_{2U} assemblage of biotite and muscovite is interpreted to be retrograde from the garnet-dominated M_{1U} assemblage.

Thermal constraints

Petrographic observations indicate a crude path from peak to retrograde metamorphism. Various geothermobarometric techniques were investigated to place quantitative constraints on the path from peak to retrograde metamorphism (Table C.1). Garnet-biotite thermometry is the only method amenable to the suite of samples from the lower Nar valley. Garnet-biotite thermometry only constrains the peak metamorphic temperature of M_{1U} because garnets are not observed in the Lower Level. The thermodynamic basis of geothermobarometry and the uncertainties of the garnet-biotite thermometer are discussed in Appendix C.

Methodology

The garnet-biotite thermometer is a cation exchange reaction originally calibrated by Ferry and Spear (1978):

$$KFe_3AlSi_3O_{10}(OH)_2 + Mg_3Al_2Si_3O_{12} = KMg_3AlSi_3O_{10}(OH)_2 + Fe_3Al_2Si_3O_{12}$$

[annite] [pyrope] [phlogopite] [almandine]

Biotite inclusions and adjacent biotite are paired with nearby garnet points (Ferry and Spear 1978). Core temperatures are calculated by pairing biotite inclusions in a garnet porphyroblast with a nearby garnet core point. Rim temperatures are calculated by pairing an adjacent biotite to a rim garnet point (Hodges and Crowley 1985).

Three Unit E samples (Figure 4.1) were analysed on the Cameca SX-50 microprobe at the University of British Columbia. Two samples were garnet-biotite schist (T-105 & N-102) and the other was garnet-biotite phyllite (N-38).

T-105 and N-102 are adjacent stations at the same structural level. N-38 is ~500 m structurally higher and 14 km north of T-105 and N-102. Garnet and biotite microprobe data presented in Appendix C were collected under the supervision of M. Raudsepp.

For each sample, multiple garnets were traversed with perpendicular traverses. Biotite inclusions, adjacent biotite and matrix biotite were analysed for each traversed garnet. Biotite inclusions were paired with nearby core garnet points and adjacent biotites were paired with rim garnet points.

Metamorphic temperatures were calculated manually and using TWEEQU (Berman 1991). Temperatures of representative samples were calculated manually (Appendix C; Table C.5) following the method of Ferry and Spear (1978). Representative pairs were analysed by D. Marshall using TWEEQU (Berman 1991). TWEEQU uses the Berman (1990) garnet activity model and the McMullin et al. (1991) biotite activity model. Temperature ranges from TWEEQU graphs were derived using 9 kbar as a reasonable prograde and peak metamorphic pressure for central Nepal (Vannay and Hodges 1996; Guillot et al. 1999).

Results

The end member compositions of the garnets were calculated to constrain the chemical variability of garnets (Table C.4). X_{Alm} increases towards the rim suggesting lower temperatures at the rims (Figure 4.3). 'Reversed' modal garnet trends were previously documented in central Nepal (Arita 1983). Increased X_{Alm} in the rim is mirrored by decreased X_{Grs}. In the T-105 traverse, X_{prp} increases towards the rim, suggesting higher temperature rims.

Results yielded by the method of Ferry and Spear (1978) reveal upper greenschist to lower amphibolite facies conditions (450-580°C) and internal consistency within samples and between adjacent samples (Table C.6). The results from the Ferry and Spear (1978) method (Table C.6) compare well with the following TWEEQU results (Figure 4.3).

The garnets from the schist (T-105 & N-102) exhibit inclusion-poor cores surrounded by inclusion-rich rims. Temperatures derived from the cores of garnet paired with biotite inclusions suggest core temperatures of 540-550 ± 50°C for sample T-105 (Figure 4.3A). Rim temperatures derived from pairs with adjacent biotite suggest equilibrium at 620-650 ± 50°C (Figure 4.3A). There is internal consistency of five pairs from sample T-105 with five pairs from an adjacent sample (N-102). Therefore garnets grew during prograde metamorphism at temperatures consistent with amphibolite facies. Apparent prograde growth may be due to biotite retrogression but this seems unlikely since other garnets in the nearby Buri Gandaki are documented to have grown in prograde conditions, albeit at higher temperatures (Hodges et al. 1988).

The garnet from the phyllite (N-38) lacks both garnet growth zones and biotite inclusions. Adjacent biotites were paired with garnet core and rim values (Figure 4.3B). Temperatures for the core (460-470 ± 50°C) and rim (500-530 ± 50°C) are within the standard 50°C error of thermometric methods. These results also suggest upper greenschist to lower amphibolite facies conditions. Further discussions are based on the rim temperature because this is the only value that can be reasonably assumed to be in equilibrium (Hodges et al. 1988).

Comparing the rim temperatures of T-105 and N-38 suggests that the entire map area may not have experienced identical peak metamorphic conditions. The garnet rim temperatures of the phyllite (500-530°C) are comparable to the garnet core temperature of the schist (540-550°C). The different rim temperatures thus imply the schist experienced a higher temperature (620-650°C) peak metamorphic event than the phyllite which is supported by textural evidence. There is evidence for two garnet growth zones within the schist, but not in the phyllite. Additionally, there is a difference in the S_{1U} textures (schist vs. phyllite). However, there is no textural evidence that this was a separate event suggesting the schist experienced a higher temperature component of M_{1U} peak metamorphism than the phyllite.

Discussion

Metamorphic correlation of the Lower and Upper Levels

Neohimalayan high grade peak metamorphic conditions characterise the Greater Himalayan sequence (Hodges 2000; Vannay and Grasemann 2001). Guillot et al. (1999) suggested peak Neohimalayan temperatures in central Nepal are constrained to 650-700°C. In the Marsyandi, Unit II exhibits the peak metamorphic assemblage of diopside ± K-feldspar and peak temperatures of >530°C, derived from calcite-dolomite solvus thermometry (Schneider and Masch 1993).

Correlations discussed in Chapter 2 are tested by comparing the Petrographic and thermal constraints of the Lower and Upper Levels to constraints from the Greater Himalayan sequence of the Marsyandi valley. For the Lower Level, Unit A is correlated with Unit II of the Greater Himalayan sequence of the Marsyandi valley and exhibits the same diopside-bearing peak metamorphic assemblage. Temperature constraints are not available for the metamorphism of Unit A. For the Upper Level, temperatures derived for Unit E from garnet-biotite thermometry (500-650°C) are compatible with temperatures derived from calcite-dolomite solvus thermometry (Schneider and Masch 1993). Rim temperatures for the southern samples (620-650°C) compare well with regional peak metamorphic temperatures (650-750°C). Rim temperatures for the northern sample (500-530°C) are considerably lower than regional temperatures. Differences in peak metamorphic temperatures are discussed below. Petrographic constraints and thermometric data are consistent with the interpretation of the Lower and Upper Levels as a part of the Greater Himalayan sequence.

Comparing Lower and Upper Levels

Within the Nar valley, constraints on peak conditions are limited to specific units. The peak assemblages in the Lower Level are clinopyroxene-dominated while the Upper Level assemblage is garnet-dominated. Without thermal constraints for the Lower Level or cross-cutting isograds, it is impossible to determine whether M_{1L} conditions are comparable to M_{1U} conditions. Peak metamorphic assemblages are restricted to specific units, suggesting that peak metamorphic assemblages may not be coeval and that bulk composition may control metamorphic assemblages. However in the Marsyandi valley, biotite and titanite isograds cross-cut units (Schneider and Masch 1993). The lack of observed isograds in the Nar valley may be due to the sparse sampling in the Nar valley versus the 150 samples over a 15 km transect in the Marsyandi valley. More detailed work in the Nar valley, especially in the Upper Level, may reveal isograds.

Metamorphic assemblages suggest that M_{2L} and M_{2U} consist of undifferentiable, lower grade assemblages, interpreted as retrograde assemblages. In the Marsyandi valley, Schneider and Masch (1993) document a similar retrograde assemblage and suggest higher concentration of water during M_2 metamorphism because retrograde minerals (amphibole, titanite, biotite and epitode) are hydrous.

Spatial variation of peak metamorphism

Garnet-biotite thermometry suggests that peak metamorphic conditions vary spatially, from north to south, within the lower Nar valley. Peak temperatures in the south (T-105) are ~120°C higher than peak temperatures to the north (N-38). The difference in structural height between the sample locations is minimal, suggesting a southward increasing thermal gradient. The Upper Level may have been south-dipping during metamorphism, burying the southern sample to a greater depth. Alternatively, there may be an unidentified heat source in the south. The latter seems unlikely because the closest plutonic body, the Manaslu pluton, is to the north.

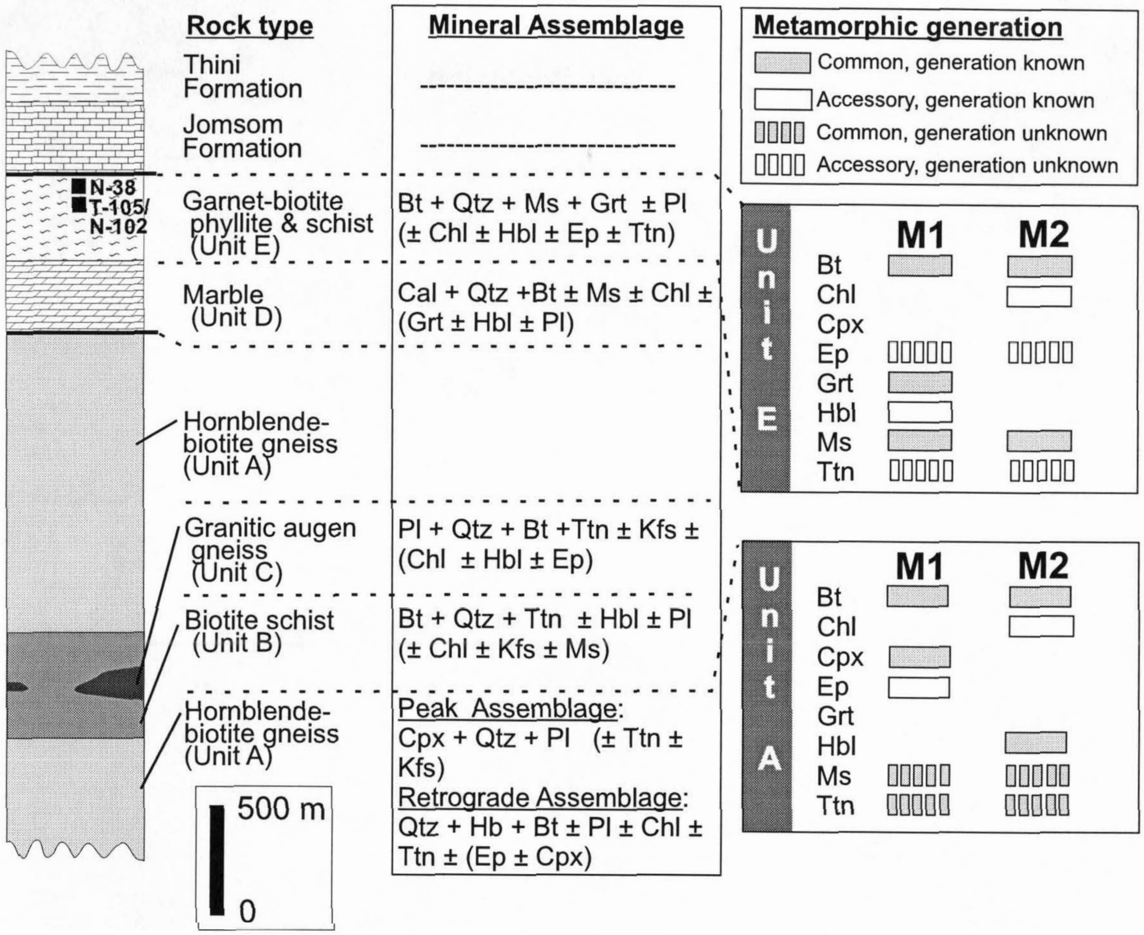

Figure 4.1. Mineral assemblages from the different structural levels with accessory minerals in brackets. Metamorphic generations for each level based on textural relations and evidence for metamorphic reactions. Mineral abbreviations after Kretz (1983).

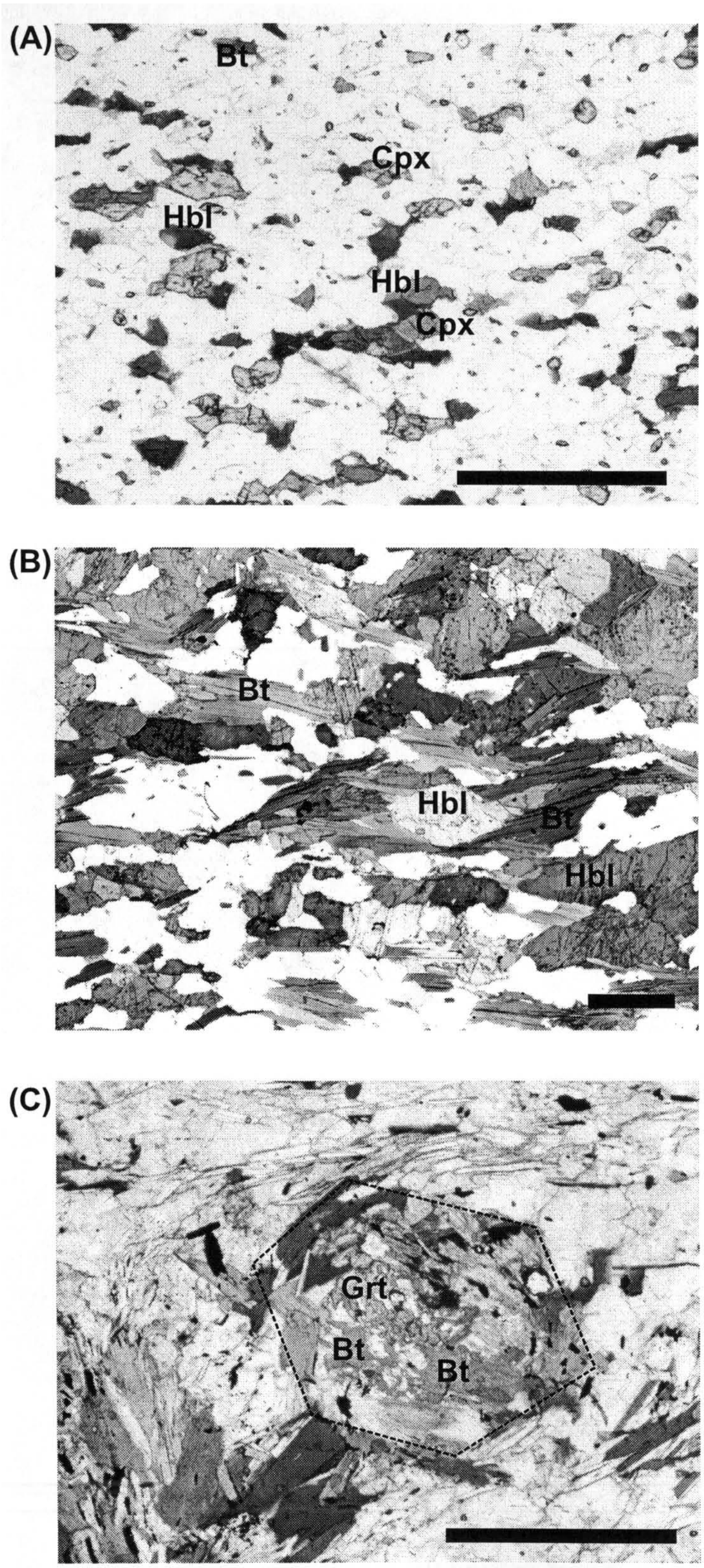

Figure 4.2. Thin sections displaying metamorphic reaction textures. A) T-05 hornblende replacing clinopyroxene in Unit A; B) T-09 biotite enclosing hornblende in Unit A; C) N-102 biotite psuedomorph of garnet in Unit E; all scales are 1 mm.

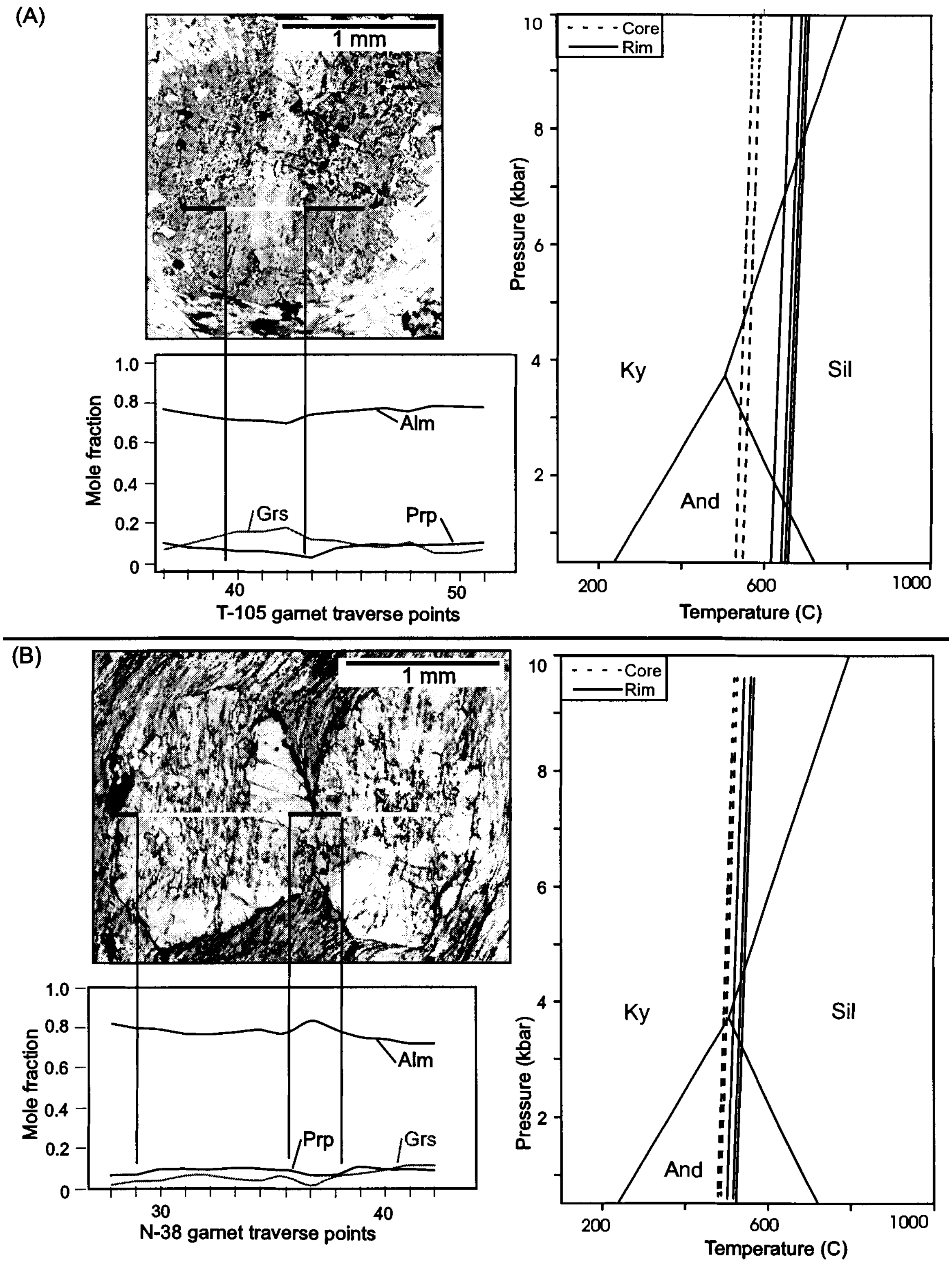

Figure 4.3. Garnet traverses with associated zoning profile. Temperatures calculated using TWEEQU (Berman 1991) for (A) garnet-biotite schist (T-105) and (B) garnet-biotite phyllite (N-38).

CHAPTER 5
DISCUSSION AND CONCLUSIONS

Introduction

Previous interpretations suggested that the lower Nar valley field area consists of a domal core of Greater Himalayan sequence protruding through a mantle of Tethyan sedimentary sequence (Bordet et al. 1975; Colchen et al. 1986). This study divides the map area into a Lower and Upper Level, which are both interpreted as part of the Greater Himalayan sequence in Chapter 2. Integration of lithological, structural and metamorphic data further tests whether rocks from the Lower and Upper Levels belong to the Greater Himalayan sequence.

The Lower and Upper Levels may have experienced different structural and metamorphic histories. They are juxtaposed along an intermediary high strain zone. Both levels are deformed by megascopic folds and affected by late brittle faulting. Age constraints from other studies are introduced to temporally constrain tectonometamorphic evolution models.

Correlations

Lower Level rock units are interpreted to belong to the Greater Himalayan sequence, partially following previous workers (Unit A = Unit II; Unit B = Unit III; Unit C = Unit III) (Colchen et al. 1986; Godin 2001). Structurally, the Lower Level exhibits ductile flow features within high strain zones. Like the Greater Himalayan sequence elsewhere in the Himalaya, the Lower Level records both south-directed simple shear and pure shear deformation (Grujic et al. 1996; Grasemann et al. 1999; Law 2003). The peak and prograde metamorphic grade of the Lower Level is poorly constrained. The predominance of clinopyroxene in peak M_{1L} assemblages suggests high metamorphic grades. The peak metamorphic grade of the Lower Level may be similar to Eohimalayan Greater Himalayan sequence metamorphic grade documented elsewhere (Hodges et al. 1988; Hubbard and Harrison 1989; Vannay and Hodges 1996). Lower Level rock types, structures, and metamorphism therefore all suggest it is part of the Greater Himalayan sequence.

Upper Level rock types cannot be directly correlated with previously described components of the Greater Himalayan sequence. Structurally, the Upper Level does not exhibit high strain zones with ductile flow. The Upper Level does contain abundant south-directed asymmetric folds. Both peak metamorphic assemblages and garnet-biotite thermometry suggest peak metamorphism at amphibolite facies (500-650°C). The Upper Level is therefore interpreted as a previously undescribed component of the Greater Himalayan sequence characterised primarily by its peak metamorphic grade.

Age constraints

Four age constraints from other workers (Figure 1.3) are reviewed: (a) cooling ages of Nilgiri Formation phlogopites from the Marsyandi valley (Coleman and Hodges 1998); (b) U-Th monazite ages from the Manaslu pluton (Guillot et al. 1994; Harrison et al. 1999); (c) a U-Pb age of a dyke near Kyang village (L.Godin and R.Parrish pers. comm. 2002); and (d) a U-Pb age of an undeformed dyke in the Marsyandi valley (Coleman 1998).

Phlogopite-grade metamorphism in the hanging wall of the Chame detachment (Nilgiri Formation) is constrained by Ar-Ar thermochronology (Coleman and Hodges 1998). In the Marsyandi valley, phlogopite outlines S_1 and S_2 axial planar cleavages (Coleman and Hodges 1998). Cooling ages cluster at 29.9 - 27.1 Ma, which is interpreted to provide a minimum age of Eohimalayan deformation and metamorphism (Coleman and Hodges 1998). Oligocene cooling ages can be extrapolated to the Nar valley if the correlation of Unit D with the Nilgiri Formation is correct. Extrapolating Oligocene cooling ages implies that Upper Level deformation, at least in part, is Eohimalayan. D_{1U} and D_{2U} may both be Oligocene if the south-west verging folds in the Marsyandi valley are coeval with F_{2U} in the lower Nar valley. Alternatively, if fold generations are not coeval, D_{1U} and D_{2U} may be Eohimalayan and Neohimalayan, respectively.

To the east of the Nar valley, two phases of magmatism within the Manaslu pluton are 22.9 ± 0.6 Ma and 19.3 ± 0.3 Ma, based on Th-Pb microprobe ages of monazites (Harrison et al. 1999). As described below, the Manaslu pluton is a useful constraint on the age of motion along the Phu detachment.

LGN22b is a sample from a 4-5 m thick leucogranitic dyke which cross-cuts S_{1L} fabrics and early layer parallel dykes (Figure 2.1). It is boudinaged and folded and is interpreted to be a second generation dyke (L. Godin pers. comm. 2002). Elsewhere, second generation dykes are synkinematic to D_{2L} deformation. LGN22b was collected and prepared by L. Godin. It was analysed and interpreted by R. Parrish and L.Godin. This dyke provides two important constraints: maximum age of D_{1L} deformation and M_{1L} metamorphism, and a minimum (and possibly approximate) age of D_{2L} deformation. A date of 19.9 ± 0.1 Ma based on a single concordant zircon (L.Godin and R. Parrish pers. comm. 2002), is interpreted as an age of crystallisation of the dyke. D_{1L} and M_{1L} predate ~20 Ma. D_{2L} at least in part postdates ~20 Ma. The mineralogy and age of the dyke suggests it may be an apophysis of the Manaslu pluton. The Upper Level is devoid of leucogranite dykes. Therefore, the dyke is only a constraint for deformation and metamorphism within the Lower Level. The Upper Level may have a separate deformation and metamorphic evolution.

In the Marsyandi valley, an undeformed leucogranitic dyke which cross-cuts ductile fabrics crystallized at 18.9 ± 0.1 Ma based on U-Pb zircon and monazite age determinations (Coleman 1998). The age of the undeformed dyke provides a minimum age of ~19 Ma for regional amphibolite facies metamorphism and ductile movement along the Chame detachment.

Tectonometamorphic Evolution

Two models of tectonometamorphic evolution are proposed (Figure 5.1). Models differ on the timing of the D_{1U}/M_{1U} and D_{2U}/M_{2U}. Model A suggests that the D_{1U}/M_{1U} is Oligocene while D_{2U}/M_{2U} is Miocene (Figure 5.1A; 5.2). Model B considers both D_{1U}/M_{1U} and D_{2U}/M_{2U} Oligocene (Figure 5.1B). Future thermochronologic data may determine which model is more appropriate for the Nar valley by providing a constraint on Upper Level metamorphism. In both models (Figure 5.1), the timing of D_{1L}/M_{1L} is unconstrained; D_{1L}/M_{1L} may be Oligocene as described elsewhere in the central Nepal (Vannay and Hodges 1996; Godin et al. 2001) or Miocene. Later features of both models include the Phu detachment, late crustal-scale folding and brittle faulting. As described below, Model A is favoured and will be the basis for subsequent discussion (Figure 5.2).

Model A suggests that the D_{1U} is Oligocene while D_{2U} is Miocene (Figure 5.1A; 5.2). Biotite retrograde metamorphism is coeval in Lower and Upper Levels and coeval to the latest movement on the Chame detachment. Model A is favoured because: it explains the metamorphic continuity across the Chame detachment; it is consistent with S_{2U} being kinematically linked to the Chame detachment; and it predicts that the Upper Level is above ~300°C (the biotite closure temperature; Hanes 1991) while being emplaced on the Lower Level during intense Neohimalayan metamorphism rather than being below the biotite closure temperature since Eohimalayan metamorphism. In Model A, the Oligocene deformation and metamorphism of the Nilgiri Formation (Coleman and Hodges 1998) are not extrapolated to the Upper Level of the Nar Valley.

Model B considers the Upper Level deformation and metamorphism to be entirely Oligocene (Figure 5.1B). Model B incorporates the Oligocene constraint for the F_2 folds in the Nilgiri Formation (Coleman and Hodges 1998) and correlates the F_2 folds in the Nilgiri Formation with F_{2U} folds in Upper Level of the Nar Valley. Model B is not favoured because it does not explain the metamorphic continuity across the Chame detachment and because Model B predicts that the Upper Level remains below ~300°C (the biotite closure temperature; Hanes 1991) while being emplaced on the Lower Level during intense Neohimalayan metamorphism.

Before 20 Ma

In the Upper Level, the conditions of the first phase of deformation and metamorphism are well constrained (Figure 5.2A). Synkinematic garnet textures reveal that prograde and peak metamorphism (M_{1U}) is coeval with D_{1U} foliation-producing, south-verging deformation. Metamorphic assemblages and garnet-biotite thermometry suggest M_{1U} is amphibolite facies (500-650°C). The timing of D_{1U}/M_{1U} is only constrained by the extrapolation of cooling ages (29-27 Ma) from the Nilgiri Formation in the Marsyandi valley because the Upper Level is devoid of leucogranitic dykes (Coleman and Hodges 1998). In the Marsyandi valley, phlogopite outlines S_1 and S_2 axial planar cleavage. Possibly, the southward rotated D_{1U} garnets in the Upper Level are coeval to the south-verging Oligocene F_2 folds recorded in the Nilgiri Formation in the Marsyandi valley (Coleman and Hodges 1998), or south-verging pre-Oligocene F_1 found in the Paleozoic levels of the Kali Gandaki valley (Godin et al. 1999b; Godin 2003).

In the Lower Level, the clinopyroxene-bearing M_{1L} assemblages outline S_{1L} and are coeval with D_{1L} (Figure 5.2A). Both D_{1L} and M_{1L} are cross-cut by and older than the ~20 Ma dyke (L.Godin and R. Parrish pers. comm. 2002). In the Marsyandi valley, S_1 fabrics and peak metamorphism are older than ~19 Ma (Coleman 1998).

At ~20 Ma

In the Upper Level, biotite-muscovite retrograde metamorphism (M_{2U}) is coeval to the development of the shallow north-dipping S_{2U} crenulation cleavage (Figure 5.2B). The crenulation cleavage is axial planar to south-verging F_{2U} kinks and outcrop-scale folds. The S_{2U} crenulation cleavage is only developed in the Upper Level and is kinematically compatible with formation in the compressional field of the strain ellipse in the hanging wall of a normal fault.

In the Lower Level, ductile general shear with a south-directed simple shear component characterises D_{2L} deformation. The relationship between D_{2L} and biotite retrograde metamorphism is unconstrained. D_{2L} is (wholly or partially) younger than ~20 Ma because D_{2L} boundinages and folds the LGN22b leucogranitic dyke. The timing, south-verging asymmetry and transpositional nature of D_{2L} suggest that it may be part of the Miocene Neohimalayan extrusive history of the Greater Himalayan sequence.

The Chame detachment is a high strain zone between the Lower and Upper Levels. As discussed in Chapter 3, structural overprinting relationships, fabric transposition and type of ductile structures suggest the Chame detachment may be correlative to D_{2L} deformation. In the Marsyandi valley, the Chame detachment is a ductile, top-to-the-north shear zone that is syn-metamorphic to peak sillimanite-grade through retrograde greenschist facies metamorphism (Coleman 1996). The type and duration of motion suggests that the Chame detachment juxtaposes the Upper Level rock units on the Lower Level rock units at ~ 20 Ma during retrograde metamorphism of both levels. Cross-section and map constraints suggest that the Chame detachment cuts down to the north through Unit E, between Chame and Chhacha (Figure 3.5C).

A recent re-interpretation of the Annapurna region considers the Chame detachment to be wholly within the Greater Himalayan sequence (Searle and Godin 2003). Lithological, structural and metamorphic data presented here support this interpretation. But these same data suggest the Chame detachment juxtaposes two levels of the Greater Himalayan sequence composed of different rock units with different tectonometamorphic histories. The spatial or stratigraphic relationship between the Lower and Upper Levels before motion on the Chame detachment remains uncertain.

After 19 Ma

The Phu detachment (Figure 5.2C) is a recently recognized high strain zone juxtaposing garnet-grade phyllite in its footwall against unmetamorphosed Tethyan sedimentary sequence in its hanging wall (Searle and Godin 2003). The Phu detachment is interpreted as the upper, brittle strand of the South Tibetan detachment system which down cuts through previously folded strata (L.Godin pers. comm. 2003). The Phu detachment cross-cuts the Manaslu pluton (Searle and Godin 2003). Therefore the Phu detachment is younger than the ~19 Ma phase of the Manaslu pluton (Harrison et al. 1999; Searle and Godin 2003).

The Lower and Upper Levels and the overlying Tethyan sedimentary sequence form a cohesive structural block after movement along the Phu detachment ceased sometime after ~19 Ma (Figure 5.2D). The cohesive block of the Lower and Upper Levels and the Tethyan sedimentary sequence is folded by crustal-scale open folds. The Mutsog synform and Chako antiform are a non-cylindrical antiform- synform pair, recording late contraction.

The Mutsog synform and Chako antiform complicate the geometry of the Marsyandi valley-Manaslu area in three ways: they modified the homoclinal geometry of the Greater Himalayan sequence in the Marsyandi and Nar valleys; they produced an apparent dome (Bordet et al. 1975); they generated apparent orogen perpendicular movement along the Chame detachment by folding part of the Chame detachment into a orogen-parallel orientation after it ceased movement (Coleman 1996).

The non-cylindrical geometry of the Mutsog synform and Chako antiform may be partially controlled by pre-existing structures, or structures at depth. The gentle west plunge of the folds may be controlled by the Manaslu pluton to the east. The fold axis of the Chako antiform may have localised around the large pod of Unit C augen gneiss, which is coincident with the hinge of the Chako antiform (Figure 4.2). At a larger scale, the synform-antiform pair may have localised along a ramp in the Main Himalayan thrust or a thrust duplex at depth (Hauck et al. 1998).

At ~14 Ma (?)

Zones of steep north-south meso-scale brittle faults and fractures are the youngest structural feature (D_4) preserved in the Nar valley. Two large scale geographical features may be controlled by steep north-south brittle faults (L.Godin pers. comm. 2003). First, the Nar valley is a north-south drainage. Second, the east face of Chubche is a ~3500 m cliff that is oriented north-south. Small-scale brittle faults cross-cut D_{2L} features and are thus younger than D_{2L} (~20 Ma). The Nar valley drainage and the east face of Chubche cross-cut D_3 megascopic folds suggesting D_4 is younger than D_3 (<19 Ma).

The late, brittle faults are geometrically similar to the set of brittle faults in the Marsyandi valley. Coleman and Hodges (1995) dated hydrothermal muscovite grown synkinematic to late, north-south brittle faulting. A plateau age of 14.3 Ma ± 0.9 Ma was derived using Ar-Ar thermochronology (Coleman and Hodges 1995). The dated minor fault was interpreted by Coleman and

Hodges (1995) to be part of the Thakkhola graben structure and may mark the onset of gravitational collapse of the Tibetan plateau.

Conclusions

1. Lower and Upper Levels are both interpreted as part of the Greater Himalayan sequence. Similar rock types, high-strain zones with south-verging shear-sense indicators, and high-grade metamorphism all suggest that the Lower Level is part of the Greater Himalayan sequence. The Upper Level is interpreted as part of the Greater Himalayan sequence based on high-grade metamorphic assemblages and 500-650°C peak metamorphic temperatures.

2. The meta-sedimentary units of the Lower and Upper Levels may be derived from Lower Paleozoic Tethyan sedimentary sequence. However, differences in structural style and peak metamorphic grade suggest the Lower and Upper Levels may have different tectonometamorphic histories. Upper Level structures suggest it was deformed at higher structural levels than the Lower Level. The lack of cross-cutting isograds or temperature constraints from the Lower Level make it impossible to determine if both levels experienced similar peak metamorphic conditions.

3. The Lower and Upper Levels were juxtaposed along the synmetamorphic Chame detachment at ~20 Ma during retrograde metamorphism. After ~19 Ma, the Phu detachment placed the unmetamorphosed Tethyan sedimentary sequence onto the Upper Level.

4. The Lower and Upper Levels and the Tethyan sedimentary sequence were folded, after 19 Ma, by a non-cylindrical antiform-synform pair with a ~25 km wavelength which created an apparent dome.

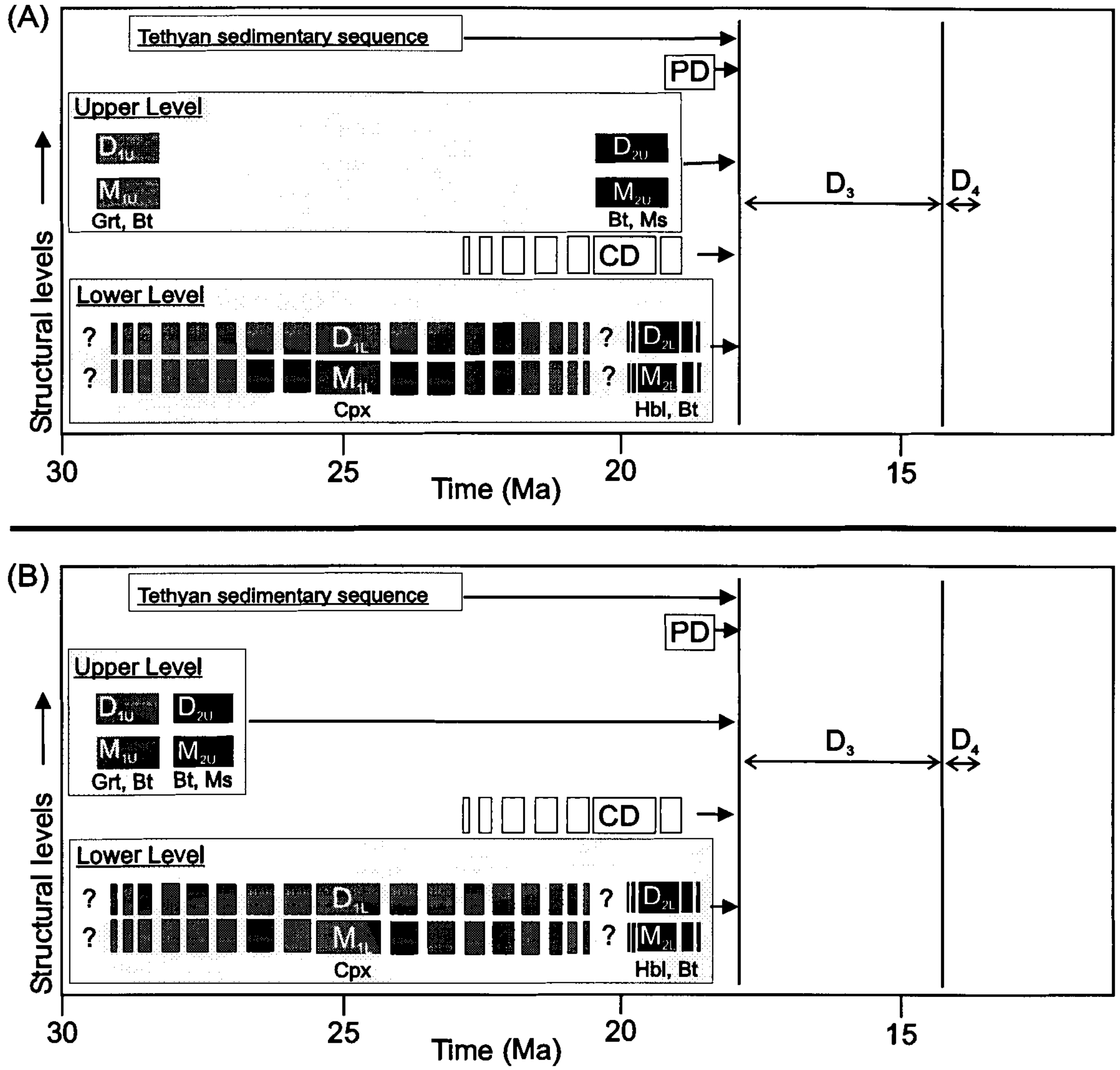

Figure 5.1. Two models for the tectonometamorphic evolution of the lower Nar valley. The Chame detachment (CD) and Phu detachment (PD) mark the level boundaries. Geochronological constraints are discussed in the text. Model (A) considers D_{1U}/M_{1U} Oligocene and D_{2U}/M_{2U} Miocene. Model (B) considers both D_{1U}/M_{1U} and D_{2U}/M_{2U} Oligocene. Differentiation pends Ar-Ar thermometry from the Nar valley.

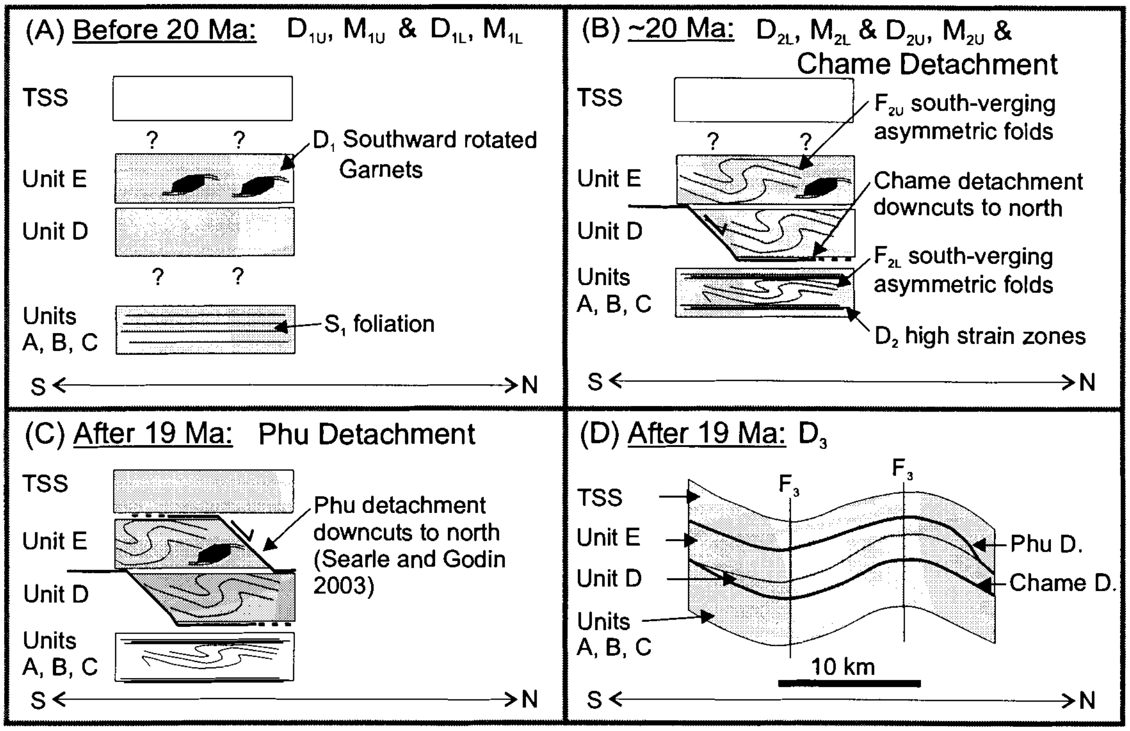

Figure 5.2. Favoured tectonometamorphic evolution model (Figure 5.1a). TSS is the Tethyan sedimentary sequence. All views look west and are scaleless except D. Levels active during time period are in grey. Time constraints discussed in text. (A) Eohimalayan metamorphism and deformation in the Lower (?) and Upper Levels; (B) Neohimalayan deformation in the Lower and Upper Levels coeval to the Chame detachment which emplaces the Upper Level on the Lower Level and downcuts to the north; (C) Phu detachment emplaces the Tethyan sedimentary sequence on the Upper Level and also downcuts to the north; (D) late crustal-scale folding. Late brittle faults are not shown.

CHAPTER 6
IMPLICATIONS AND FUTURE RESEARCH

Implications

This study contributes to the understanding of the Himalaya by characterising the Greater Himalayan sequence in central Nepal, documenting the structure of the Greater Himalayan sequence, and constraining the metamorphic evolution of the upper Greater Himalayan sequence. Previously, the Greater Himalayan sequence was considered a homoclinal slab comprising three formations (LeFort 1975). The results from this study suggest a more lithologicaly diverse Greater Himalayan sequence composed of structural levels that can be lithologicaly differentiated. In the Nar valley, the Lower and Upper Levels experienced polyphase deformation and amphibolite facies metamorphism, though possibly at different stages of Himalayan orogenesis. The study qualitatively documents both general non-coaxial strain and strain partitioning, which is similar to the structures of the upper Greater Himalayan sequence throughout the Himalaya (Grujic et al. 1996; Vannay and Grasemann 2001; Law 2003). In addition, this study supports the recent interpretation by Searle and Godin (2003) of a two-strand South Tibetan detachment system in the Annapurna region and further interprets the Chame detachment as a down-cutting Miocene normal fault within the Greater Himalayan sequence. This study documents late crustal-scale folding which has not been previously documented in central Nepal. This study also derives a critical amphibolite facies metamorphic constraint for the Upper Level, which was previously considered part of the Tethyan sedimentary sequence.

Future Research

Provided here are research questions that remain unanswered, given the available data. Following each question is a potential method that could be used to solve this question in the future:

1) Why does the Chame detachment apparently change vergence directions from north to south? A more detailed microstructural analysis between Kyang and Phu (*i.e.* Law 2003) could elucidate this problem.

2) What is the metamorphic grade of M_{1L}? The Al-in-hornblende geobarometer (Johnson and Rutherford 1989) might constrain the pressure.

3) Is D_2 coeval at different levels? The maximum age of D_{2L} is well constrained. Ar-Ar thermochronology is the only method available to date D_{2U} because the upper level is devoid of leucogranitic dykes. Unit E samples are currently being analysed for muscovite Ar-Ar cooling ages. Muscovite Ar-Ar cooling ages may elucidate which of model A or B (Figure 5.1a or 5.1b) is more appropriate for the Nar valley.

APPENDIX A
MINERALOGY

Seventy-nine thin sections representing the lithological diversity of the entire map area were systematically surveyed (Table A.1). This survey concentrated on the timing and constituents of metamorphic assemblages and how these vary within and between structural levels. Each structural level contains a distinct metamorphic assemblage (Figure 4.1).

A Dualbeam 235 scanning electron microscope (SEM), at the SFU nano-imaging facility, analysed minerals that were difficult to identify using the petrographic microscope (Table A.2). SEM imaging and *in situ* x-ray spectroscopy helped identify accessory minerals and confirmed the paucity of aluminosilicate minerals.

Table A.1. Mineralogy of all samples organised by structural levels: Biotite (Bt), Calcite (Cal), Chlorite (Chl), Clinopyroxene (Cpx), Epidote (Ep), Garnet (Grt), Hornblende (Hbl), K-Feldspar (Kfs), Muscovite (Ms), Plagioclase(Pl), Titanite (Ttn) and Tourmaline (Tur). HS = high strain; Litho = field lithology; Microstructure = microstructural observation.

Sample	Litho	Unit	Camp	Bt	Cal	Chl	Cpx	Ep	Grt	Hbl	Kfs	Ms	Pl	Ttn	Tur	HS	Microstructure
N-006.4b	Leuco	-	Chako			x				x	x		x				
N-014	leuco fracture	-	Chako			?				x		?	x				
N-02D	leuco	-	Kyang			?				x		?	x				
N-06	QFP	-	Chako			x			x		x	x	x				
T-006e	schist (float)	-	Chako		x		x										
T-115	granite	-	Dzonum	x						x			x	x			
N-02TSS	calc-sil gneiss	A	Kyang	x	x		x						x	x			fractures
N-023b	calc-sil gneiss	A	Kyang	x	x	?	x							x			
N-025a	calc-sil gneiss	A	Kyang	x	x		x							x			C-S
N-025b	calc-sil gneiss	A	Kyang	x	x		x							x			C-S
T-0D	calc-sil gneiss	A	Kyang	x	x		x			x			?	x			
N-015b	calc-sil gneiss	A	Chako	x		x	x				x		x	x			
N-017	calc-sil gneiss	A	Chako	x	x		x						x	x			
T-007	calc-sil gneiss	A	Chako	x			x	x		x			x	x			
T-026	upper calc-sil	A	Kyang		x		x							x			
T-028	lower calc-sil	A	Kyang		x		x							x			
T-054	calc-sil gneiss	A	Dharmasal	x	x		x						x	x			
T-101	calc-sil	A	Koto		x		x			?			x				
T-005a	calc-sil gneiss	A	Chako				x			x			x	x			
T-005b	calc-sil gneiss	A	Chako	x			x	x		x	x		x	x			
T-006a	calc-sil gneiss	A	Chako	x		?	x	x		x	?		x	?			
T-006b	calc-sil gneiss	A	Chako	x				x		x			x	x			
T-006c	calc-sil gneiss	A	Chako	x		x		?				x	x	x			
T-01B	bt schist-calc sil	A-B	Chako	x			x	?		x							
T-034	calc sil bt schist	A-B	Chiapa	x			x			x			?	x			
N-006.4a	bt schist	B	Chako	x			x				?		x	x			
N-006.5	bt schist	B	Chako	x						x			x				quartz ribbon
N-01A	bt schist	B	Chako	x				?					x	x			
N-020	bt schist	B	Chako	x									x	x	x		C-S fabrics

Table A.1. Mineralogy of all samples organised by structural levels: Biotite (Bt), Calcite (Cal), Chlorite (Chl), Clinopyroxene (Cpx), Epidote (Ep), Garnet (Grt), Hornblende (Hbl), K-Feldspar (Kfs), Muscovite (Ms), Plagioclase(Pl), Titanite (Ttn) and Tourmaline (Tur). HS = high strain; Litho = field lithology; Microstructure = microstructural observation.

Sample	Litho	Unit	Camp	Bt	Cal	Chl	Cpx	Ep	Grt	Hbl	Kfs	Ms	Pl	Ttn	Tur	HS	Microstructure
N-021	schist	B	Kyang	x		x				x	?		x	?			composite fabrics
N-034	Bt schist	B	Nar	x								x	?				composite fabrics
T-005	bt schist	B	Chiapa	x						x			x				composite fabrics
T-008	bt schist	B	Chako	x		x		x			x		x	x			composite fabrics
T-009a	bt schist	B	Chako	x						x			x				composite fabrics
T-009b	bt schist	B	Chako	x			?			x			x				composite fabrics
T-013	bt schist	B	Chako	x				x			?		x	?			composite fabrics
T-029a	bt schist	B	Kyang				x			x			x	?			
T-029b	bt schist	B	Kyang	x			x			x			x	?			
T-030	bt schist	B	Chiapa	x						?			x				
T-116a	bt schist	B	Dzonum					?		x			x	x			
T-036a	bt schist	B	Chiapa	x						?			x				
N-006.3	augen gneiss	C	Chako	x				x					x	x			porphyroclast
N-009	augen gneiss	C	Chako	x				x			?		x	?			composite fabrics
N-01B	augen gneiss	C	Chako	x				x					x	?			quartz ribbon
N-01C	augen gneiss	C	Chako	x				x					x	?			quartz ribbon
N-108	augen gneiss	C	Chako	x		x				x			x	x			quartz ribbon
N-109	augen gneiss	C	Chako	x		x							x	x			quartz ribbon
N-110	augen gneiss	C	Chako	x		x				x			x	x			quartz ribbon
T-010	augen gneiss	C	Chako	x		x				x			x	x			oblique mica
T-01C	augen gneiss	C	Chako	x		x							x				
T-033	augen gneiss	C	Chiapa	x				x					x	x			quartz ribbon
T-037b	augen gneiss	C	Chiapa	x		x							x	x			composite fabrics
T-02C	bt marble	D	Kyang	x	x				x			x					oblique mica
N-015a	marble	D	Chako	x	x	?				x			x	?			
N-019	marble	D	Chako	x	x	?											
N-027	bt marble	D	Kyang	x	x												composite fabric
N-028	dolomite	D	Kyang		x	x						?					
N-036a	limestone	D	Nar	x	x												

Table A.1. Mineralogy of all samples organised by structural levels: Biotite (Bt), Calcite (Cal), Chlorite (Chl), Clinopyroxene (Cpx), Epidote (Ep), Garnet (Grt), Hornblende (Hbl), K-Feldspar (Kfs), Muscovite (Ms), Plagioclase(Pl), Titanite (Ttn) and Tourmaline (Tur). HS = high strain; Litho = field lithology; Microstructure = microstructural observation.

Sample	Litho	Unit	Camp	Bt	Cal	Chl	Cpx	Ep	Grt	Hbl	Kfs	Ms	Pl	Ttn	Tur	HS	Microstructure
T-047	pink calc	D	Labse K.	x	x							x					
T-048a	calcite layer	D	Labse K.	x	x	x						x					
T-05A	upper ls	D	Namya	x	x	?			x			x					
T-056/N-105	marble	D	ChaCha	x	x							x					
T-117	bt marble	D	Kyang	x	x												
N -105	phyllite	D	ChaCha	x		x						x	x				S_2 crenulation
N-038	gt phyllite	D	Nar	x	x	x			x								Garnet porphyroblast
N-10D	gt schist	D	ChaCha	x		x			x			x	x				S_1/S_2
N-104	gt phyllite	D	Chacha	x		?		x	x			x		x			composite fabric
T-048b	shale layer	D	Labse K.	x	x							x					
T-05B	phyllite	D	Namya	x		?			x			x					
T-10TSS	phyllite	D	ChaCha	x								x	x	x			
T-104a	bt gt schist	D	ChaCha	x						x		x	?				
T-104b	bt gt schist	D	ChaCha	x								x	?				
T-105	phyllite	D	ChaCha	x					x			x					Garnet porphyroblast
T-107b	bt gt schist	D	ChaCha	x					x	x		x					S_1/S_2
T-126b	siltstone	D	Namya	x								x					
T-127	schist	D	Namya	x					x			x					
T-134c	phyllite	D	Namya	x					x			x					Garnet porphyroblast
T-135a	phyllite	D	Namya	x					?								
T-140b	phyllite	D	Nar	x													

Table A.2. Mineral data from SEM.

Sample	Question	Results
T-54	Titanite?	Titanite
T-34	Epidote?	Titanite
T-06c	Titanite?	Titanite
N-109	Epitode?	Titanite
T-33	Epidote?	Epidote
N-104	Kyanite?	Epidote
N-102b	Sillimanite?	Muscovite
	Garnet?	Pyrope garnet
	Biotite?	Phlogopite

APPENDIX B
STRUCTURAL OBSERVATIONS

Field measurements are collated in Table B.1. Microstructural observations are summarized in Chapter 3. Cleavage domains are used to describe S_1 foliation morphology (Passchier and Trouw 1998).

Table B.1. Field measurements. L_a includes macro to meso fold axis. L_{min} are mineral aggregate. L_{rod} are mineral rods. L_{int} are intersections of S_2 on S_1. L_{cren} are crenulations. TSS = Tethyan sedimentary sequence.

Station	Unit	S_0	S_1	S_2	S_3	F_2	L_{min}	L_{rod}	L_{int}
N-102	D		085 70						
N-102	D		280 06						
N-102	D		113 34						
N-103	D		110 32	270 42			100 08		
N-104	D	116 30		295 06					
T-102	D		185 30						
T-103	D		215 34						
T-104	D		092 61	200 41	258 20				262 24
T-104	D		110 25	195 40					
T-104	D		110 55	206 39					
T-106	D		185 24						
T-106	D		190 20						
T-107	D		059 49	204 32		176 29			262 19
T-107	D		054 30	244 41		316 44			
T-107	D		084 37	246 29					
N-102	D		086 66	310 20					
N-102	D		082 66	302 30					
N-102	D		072 71	281 26					
T-108	D		091 68	274 44					
T-108	D			290 65					
T-108	D			271 52					
N-104	D		105 26						
T-124	D		110 29			260 16			
T-124	D		125 45						
T-124	D		130 38						
T-126	D		065 19				090 24		
T-126	D		061 27						
T-133	D		281 05						
T-134	D		248 28	210 19			070 02		
T-134	D		258 13	065 05			091 11		
T-134	D		245 10						
T-134	D		292 24						
T-135	D		240 06	279 24		105 06	101 02		
T-135	D		165 15	270 38		266 05			
N-105	D-D	111 36							119 03
T-48a	D-D		226 06				340 03		
T-48b	D-D		224 12				335 15		
T-56	D-D		106 43						
N-105	D-D	119 25		276 26		109 04			
N-105	D-D	096 26							
T-125	D-D		110 75			285 20			
T-125	D-D		270 56						
T-127	D-D		126 55				280 31		
T-128	D-D		260 46			261 05			
T-128	D-D		111 20			255 02			
T-128	D-D		095 43			259 06			

Station	Unit	S_0	S_1	S_2	S_3	F_2	L_{min}	L_{rod}	L_{int}
T-129	D-D		240 16			280 05			
T-130	D-D		151 33						
T-111	D		105 26						
T-111	D								
N-106	A-D		290 56	306 16		135 16			
N-106	A-D		134 18						
N-106	A-D		095 81						
N-106	A-D		106 44						
T-50	A		100 36				260 19		
T-53	A		130 35				285 21		
T-54	A		128 44				303 03		
T-54	A		318 39						
T-55	A		102 67						
T-55	A		140 37						
T-58	A		118 54						
T-59	A		225 26						
T-101	A		210 37						
T-131	A		221 35						
T-132	A		213 26						
N-106	A-D					103 03			
N-106	A-D					108 09			
N-101	A		185 25				224 12		
N-107	A		121 44				273 13		
N-3	B		175 29						
N-34	B		142 24	231 23					295 20
N-34	B		138 22	243 29					
N-34	B		162 24	246 16					
N-35	B		175 07						
T-30	B		125 82	180 64					
T-30	B		115 51						
T-30	B		160 30						
T-30	B		110 55						
T-30	B		121 65		160 12				
T-32	B					325 25			
T-34	B		145 45				150 10		
T-35	B		200 14						
T-36	B		150 32				321 11		
T-36	B		141 55						
T-36	B		298 88						
T-36	B		134 50						
T-36	B		115 16						
T-38	B		120 26				134 06		
T-38	B		131 31				155 10		
T-39	B		168 23						
T-39	B		194 21						
T-49	B		206 06						
T-113	B		094 24						
T-114	B		195 11						
T-115	B		140 24				338 05		

Station	Unit	S_0	S_1	S_2	S_3	F_2	L_{min}	L_{rod}	L_{int}
T-115	B		110 22				330 03		
T-36	B				020 70	310 14			
T-36	B				021 61				
T-36	B				022 47				
T-36	B				016 57				
T-36	B				019 54				
T-36	B				013 65				
T-36	B				013 66				
T-36	B				003 56				
T-36	B				007 86				
T-36	B				023 67				
T-52	A-B		090 30				214 25		
N-1	A		125 12		025 82		131 10		
N-1	A		118 15						
N-2	A		165 60			290 22			
N-4	A		062 32						
N-5	A		098 24						
N-32	A		204 20				206 03		
N-32	A		206 24			196 06	012 08		
N-33	A		178 24			008 04		172 02	
N-33	A		169 18			320 16		356 09	
N-33	A							008 04	
T-01	A		115 12		202 80				
T-02	A		065 21						
T-02	A		059 33						
T-03	A		165 25						
T-04	A		116 37						
T-05a	A		174 22			320 05		189 06	
T-06	A		199 22				021 03		
T-112	A		220 12				030 02		
T-05	A				029 89				
T-05	A				025 81				
T-05	A				005 88				
T-05	A				205 76				
T-05	A				011 84				
T-05	A				025 76				
N-30	TSS	102 08	298 08		264 25				
N-30	TSS	340 05	274 46			290 11			
N-24	D		282 21			092 12			
N-27	D		325 30	315 29		320 15			
N-28	D	235 25	310 30	080 05			328 22		123 04
T-22	D		284 24						
T-23	D		320 30						
N-6	C		265 30						
N-6	C								
N-9	C		265 32				103 10		
N-9	C		291 35	295 44					
N-6.1	C		278 28	175 35	176 64				
N-6.2	C		280 46		184 88			320 28	

Station	Unit	S_0	S_1	S_2	S_3	F_2	L_{min}	L_{rod}	L_{int}
N-6.3	C		265 31		200 69			322 16	
N-6.4	C		278 16		352 72			358 16	
N-6.4	C		268 28			010 10			
N-11	C		305 15						
N-12	C		275 45		330 82	320 20			
N-12	C		230 30						
N-12	C		220 31						
N-108	C		264 45				315 15		
N-109	C		275 28				342 25		
N-110	C		260 18				330 20		
N-111	C								
T-10	C		281 32		050 64		310 24		
T-17	C		220 21		180 30		313 17		
T-33	C		151 31					160 34	
T-33	C		185 32					316 26	
T-33	C		120 76						
T-33	C		297 75						
T-37	C		311 32						
T-37	C		330 61						
N-7	B		258 28						
N-8	B		246 25						
N-8	B		264 34						
N-10	B		321 25						
N-10	B		186 20						
N-10	B		265 20						
N-10	B		103 31						
N-10	B		095 25				125 10		
N-11	B		334 15						
N-11	B		195 10						
N-13	B		298 16						
N-14	B		292 25				356 14		
N-15	B		360 14			096 28			
N-16	B		315 26						
N-20	B		300 28				030 28		
T-1B	B		295 23				295 05		
T-1C	B		270 30				332 40		
T-12	B		270 32						
T-13	B		285 09				329 15		
T-14	B		262 20						
T-15	B		265 05						
T-29	B		328 16						
T-29	B		225 08						
T-29	B		140 60						
T-29	B		122 76						
T-29	B		145 51						
N-25	A-D		315 20					322 03	
N-25	A-D		290 32						
T-20	A-D		265 45						
T-20	A-D		296 22						

Station	Unit	S_0	S_1	S_2	S_3	F_2	L_{min}	L_{rod}	L_{int}
T-21c	A-D		292 14		005 81		014 19		
T-2C	A-D		280 30						
T-21d	A-D		312 22		014 85		025 25		
T-25	A-D		328 31						
T-57	A-D					305 06			
N-17	A		326 10						
N-18	A		303 28						
N-18	A		345 12						
N-21	A		244 22						
N-22	A		252 22				352 15		
N-23	A		288 20				022 24		
N-23	A		012 19			032 18			
N-26	A		291 18		009 86				
T-18	A		283 12						
T-19	A		341 28				095 26		
T-26	A		300 29		005 85		329 10		
T-28	A						320 14		
T-116	A		174 26				340 03	340 08	
T-116	A		175 22				330 12		
T-116	A		175 30						
T-117	A		313 12						
T-118	A		341 12						
T-119	A		306 20						
T-120	A		210 20		148 90				
T-121	A		232 22						
T-123	A		282 28						
T-123	A		276 20						
T-40	A		215 16					356 16	
T-40	A							351 20	
N-38	TSS		196 14						
N-38	TSS		121 24	132 38					
N-38	TSS		142 15						
T-149	TSS		140 35	002 62		130 02			130 03
T-149	TSS			021 38					133 05
T-149	TSS			000 47					
T-149	TSS			030 30					
T-150	TSS		121 87			285 05			
T-150	TSS		109 83			289 09			
T-150	TSS		261 40						
T-151	TSS		165 29						
T-140	D-TSS		132 17						
T-140	D-TSS		132 20						
T-141	D-TSS		156 22						
T-141	D-TSS		140 27						
T-142	D-TSS	165 35							
T-143	D-TSS	146 35							
T-144	D-TSS	151 31			161 31				
T-152	D-TSS		125 10						
T-138	D					132 12			

Station	Unit	S_0	S_1	S_2	S_3	F_2	L_{min}	L_{rod}	L_{int}
T-138	D					327 17			
T-139	D		134 12						
N-36	D		186 27	304 14		094 03	252 12		
N-36	D		196 20	274 26		272 10			
N-36	D		202 24						
N-36	D		202 10						
N-36	D		222 21						
N-37	D		200 05						
T-45	D		201 27						
T-46	D		220 32						
T-46	D		208 29						
T-46	D		210 08						
T-47	D		155 19				306 13		

Table B.2. Description of S_1 cleavage domains following Passchier & Trouw (1998). For Level D, phyllites were used because S_1 is poorly preserved in the schist.

	Spacing (mm)	Shape	Volume (%)	Spatial relation	Transition to microlithons
Level 1	1-5	Rough	20-70	Parallel to anastomosing	Graditional
Level D	1-2	Rough	10-30	Anastomosing	Gradational
Level D	Continuous	---	---	---	---

APPENDIX C
THERMOMETRY

Various geothermobarometers were investigated to quantitatively constrain peak metamorphic conditions (Table C.1). Garnet-biotite thermometry was the only technique used. Three thin sections were analysed on the microprobe at UBC. The raw data are presented in Tables C.2 and C.3 and are also available from the author. The method is outlined in Chapter 4. Below the thermodynamic basis and uncertainties of the method are discussed. Example of the end member composition calculations (Table C.4) and the Ferry and Spear (1978) method (Table C.5) are included. Results from the Ferry and Spear (1978) method are summarized in Table C.6.

Table C.1. Geothermobarometric methods investigated.

Method	Reason why not used
Garnet-aluminosilicate-silicate-plagioclase geobarometer (Ghent 1976)	No aluminosilicate
Garnet-biotite-muscovite-plagioclase geobarometer (Ghent and Stout 1981; Hodges and Crowley 1985)	Insufficient plagioclase or possibly not in metamorphic equilibrium.
Aluminum-in-hornblende geobarometer (Johnson and Rutherford 1989)	Not applicable to pelitic assemblages because calibrated for volcanic rocks.
Calcite-dolomite solvus geothermometer (Essene 1982)	Insufficient dolomite

Thermodynamics

Geothermobarometry is based on the assumption that classical thermodynamics can be used to describe metamorphic reactions (Hodges 1991). The most fundamental equation of thermodynamics is the Gibb's free energy (ΔG) equation which describes the total internal energy of a closed system (Spear and Selverstone 1983; Hodges 1991). For a reaction at equilibrium, the following integrated form of the equation applies:

$$\Delta G = 0 = \Delta H - T\Delta S + (P-1)\Delta V + RT\ln K$$

where ΔH, ΔS, ΔV are the reaction enthalpy, entropy, and volume changes. R is the Universal Gas constant. The physical variables are temperature (T) and pressure (P). The equilibrium constant (K) is a function of the fluid composition and the composition of solid solution minerals.

Thermometric uncertainties

The garnet-biotite thermometer contains a fundamental assumption and a series of uncertainties. The assumption is that the choosen mineral grains are in chemical equilibrium ($\Delta G = 0$). This assumption is only valid if the mineral grains are in contact and show no signs of retrogression (Hodges 1991). All grains used in this study fit this criteria. Beyond this assumption are four basic uncertainties:

(1) Analytical uncertainty. These result from routine microprobe analysis and are easily quantified and propagated through calculations (Spear 1989; Worley and Powell 2000).

(2) Calibration uncertainty. Each system must be calibrated for ΔH, ΔS, and ΔV in the specified PT field. The garnet-biotite system is calibrated experimentally, which is more accurate than thermodynamic calibration (Ferry and Spear 1978).

(3) Solution modelling uncertainty. The equilibrium constant (K) for each system must be calibrated. For example, K in the garnet-biotite thermometer is strongly affected by the presence of other components such as Ca (Essene 1982). TWEEQU uses the Berman (1990) garnet activity model and the McMullin et al. (1991) biotite activity model.

(4) Retrograde uncertainty. Biotite can be reset during retrograde metamorphism (Essene 1982). This is unlikely because other garnet-biotite analysis in the region also similar garnet growth during prograde conditions (Hodges et al. 1988).

Calibration and solution modelling uncertainties are difficult to quantify (Worley and Powell 2000). For this reason a standard error of ± 50°C is applied to all calculations.

Table C.2. Garnet data from UBC microprobe.

	Na_2O	MgO	Al_2O_3	SiO_2	CaO	TiO_2	Cr_2O_3	MnO	FeO	Total
N38-1	0.00	1.74	21.04	36.57	3.04	0.07	0.01	0.87	36.77	100.11
N38-2	0.00	1.71	20.86	36.12	3.11	0.03	0.06	1.09	36.52	99.51
N38-3	0.02	1.62	20.97	36.23	3.15	0.07	0.03	1.47	35.88	99.44
N38-4	0.00	1.46	20.89	36.02	4.01	0.03	0.02	2.11	35.09	99.62
N38-5	0.00	1.40	20.93	36.31	3.94	0.04	0.00	2.86	34.22	99.70
N38-6	0.00	1.42	21.04	35.88	3.69	0.08	0.00	3.20	34.46	99.76
N38-7	0.01	1.34	21.05	36.13	4.04	0.05	0.02	3.10	33.44	99.18
N38-8	0.01	1.33	20.81	35.73	4.01	0.04	0.00	3.29	33.76	98.98
N38-9	0.02	1.31	20.84	36.01	3.84	0.05	0.02	3.96	33.73	99.78
N38-10	0.01	1.35	20.97	35.52	4.42	0.06	0.00	3.29	33.54	99.16
N38-11	0.00	1.24	20.89	35.75	4.41	0.05	0.00	4.52	32.15	99.00
N38-12	0.00	1.25	21.08	35.41	4.22	0.06	0.02	4.76	32.13	98.92
N38-13	0.00	1.19	21.16	36.54	4.53	0.06	0.05	4.86	32.08	100.46
N38-14	0.03	1.28	21.16	36.21	4.16	0.08	0.00	3.85	33.08	99.85
N38-15	0.02	1.39	21.23	36.56	4.12	0.07	0.02	3.07	33.96	100.45
N38-16	0.00	1.49	21.21	36.07	3.48	0.06	0.00	2.29	34.75	99.35
N38-17	0.00	1.72	21.28	36.43	2.98	0.04	0.00	1.42	36.37	100.25
N38-18	0.03	1.80	21.30	36.16	3.01	0.06	0.01	0.65	36.80	99.83
N38-19	0.00	1.80	21.13	36.09	2.63	0.06	0.04	0.61	37.34	99.69
N38-20	0.00	1.81	21.39	36.50	2.91	0.01	0.00	0.63	36.38	99.62
N38-21	0.00	1.72	21.41	36.27	3.43	0.03	0.06	0.86	36.51	100.29
N38-22	0.00	1.67	21.36	36.09	3.36	0.04	0.01	1.40	35.84	99.76
N38-23	0.00	1.34	21.29	36.61	4.26	0.05	0.02	2.89	33.82	100.29
N38-24	0.01	1.36	21.10	35.55	4.59	0.07	0.01	3.03	33.33	99.04
N38-25	0.02	1.51	21.15	36.15	3.58	0.05	0.04	2.37	35.31	100.18
N38-26	0.02	1.61	21.21	35.64	4.02	0.05	0.01	1.26	35.34	99.16
N38-27	0.01	1.81	21.22	36.19	2.96	0.07	0.05	0.62	36.92	99.85
N38-28	0.00	1.82	21.15	34.85	2.82	0.02	0.01	0.59	37.07	98.35
N38-29	0.01	1.77	21.11	36.03	2.80	0.03	0.05	0.94	36.95	99.69
N38-30	0.01	1.63	21.24	35.53	3.52	0.01	0.03	1.70	35.37	99.05
N38-31	0.02	1.64	21.17	36.14	3.48	0.08	0.02	1.92	35.58	100.05
N38-32	0.02	1.42	21.37	35.90	3.62	0.04	0.02	2.99	34.66	100.04
N38-33	0.00	1.42	21.14	35.94	3.67	0.08	0.01	3.04	34.20	99.51
N38-34	0.01	1.53	21.31	35.95	3.66	0.08	0.04	2.45	35.16	100.20
N38-35	0.02	1.56	21.18	36.12	3.53	0.06	0.00	2.03	35.27	99.76
N38-36	0.00	1.48	21.21	35.79	4.15	0.04	0.04	2.12	34.82	99.65
N38-37	0.00	1.81	21.25	36.07	2.81	0.03	0.01	0.69	37.17	99.84
N38-38	0.00	1.51	21.23	35.89	3.51	0.05	0.00	2.25	34.35	98.80
N38-39	0.00	1.33	21.16	36.14	3.92	0.09	0.02	3.70	33.84	100.19
N38-40	0.01	1.34	21.13	35.60	4.02	0.08	0.02	4.10	33.02	99.32
N38-41	0.02	1.18	21.01	35.90	4.13	0.05	0.00	5.17	31.70	99.17
N38-42	0.00	1.19	21.18	35.50	4.17	0.05	0.05	5.16	31.72	99.01
T105-1	0.05	1.66	21.81	36.47	6.29	0.04	0.00	1.52	30.05	97.89
T105-2	0.04	1.51	21.27	35.40	6.55	0.04	0.03	2.02	32.02	98.87
T105-3	0.00	1.47	21.43	35.97	6.57	0.01	0.00	2.14	31.49	99.08
T105-4	0.01	1.53	21.15	35.81	6.33	0.05	0.00	2.19	31.82	98.88
T105-5	0.00	1.56	21.27	35.75	5.48	0.06	0.00	2.36	32.24	98.73

	Na_2O	MgO	Al_2O_3	SiO_2	CaO	TiO_2	Cr_2O_3	MnO	FeO	Total
T105-6	0.00	1.50	21.35	35.69	6.79	0.07	0.04	2.48	31.42	99.34
T105-7	0.03	2.09	21.26	35.74	3.54	0.05	0.00	2.25	34.42	99.38
T105-8	0.01	1.84	21.51	35.67	5.82	0.02	0.00	1.85	32.20	98.91
T105-9	0.02	1.68	21.52	36.49	7.29	0.06	0.03	1.53	31.16	99.77
T105-10	0.00	1.98	21.11	35.79	6.89	0.04	0.04	1.14	30.93	97.91
T105-11	0.02	2.48	21.45	36.53	4.55	0.02	0.02	1.07	33.40	99.54
T105-12	0.01	2.57	21.52	35.91	4.43	0.03	0.03	1.20	33.09	98.79
T105-13	0.00	2.68	21.56	36.06	3.08	0.02	0.01	1.67	34.41	99.49
T105-14	0.01	2.16	21.42	35.76	5.02	0.01	0.00	1.63	33.31	99.33
T105-15	0.00	1.77	21.36	36.10	5.63	0.07	0.00	2.02	32.71	99.67
T105-16	0.02	1.52	21.10	35.32	6.23	0.03	0.00	2.34	31.95	98.53
T105-17	0.02	1.41	21.26	36.05	6.41	0.04	0.00	2.27	32.07	99.52
T105-18	0.01	1.37	21.28	35.42	6.63	0.05	0.01	2.41	31.81	98.99
T105-19	0.00	1.64	21.39	35.89	6.51	0.10	0.00	1.86	31.79	99.19
T105-20	0.01	2.15	21.17	35.66	5.86	0.04	0.02	1.48	32.11	98.50
T105-21	0.03	1.65	21.38	36.83	6.60	0.08	0.00	1.83	31.30	99.71
T105-22	0.03	1.42	21.48	36.36	6.79	0.07	0.03	2.09	31.41	99.68
T105-23	0.02	1.32	21.55	36.78	7.15	0.09	0.01	2.17	30.89	99.98
T105-24	0.04	1.36	21.49	36.30	6.88	0.04	0.00	2.36	31.46	99.92
T105-25	0.00	1.63	21.35	36.78	5.39	0.03	0.07	2.41	31.76	99.43
T105-26	0.02	1.73	21.56	36.41	6.13	0.06	0.00	2.41	31.79	100.11
T105-27	0.03	1.39	21.55	36.46	6.64	0.04	0.01	2.64	31.14	99.89
T105-28	0.03	1.58	21.33	35.99	6.26	0.04	0.00	2.56	31.20	98.99
T105-29	0.00	1.45	21.44	36.19	6.34	0.05	0.00	2.71	31.23	99.41
T105-30	0.00	1.34	21.18	35.90	6.81	0.05	0.01	2.62	31.33	99.25
T105-31	0.01	1.31	21.01	36.17	6.90	0.07	0.01	2.42	30.90	98.78
T105-32	0.02	1.34	21.21	35.64	6.92	0.07	0.02	2.47	31.43	99.11
T105-33	0.02	1.48	21.28	35.91	6.95	0.05	0.01	1.95	31.22	98.87
T105-34	0.00	2.34	21.14	34.98	4.99	0.05	0.00	1.41	33.02	97.94
T105-35	0.02	2.66	21.28	35.92	3.44	0.00	0.02	1.59	34.46	99.38
T105-36	0.01	2.13	21.18	35.46	3.61	0.06	0.02	2.24	33.89	98.61
T105-37	0.00	2.50	21.25	35.55	3.83	0.02	0.04	1.43	33.77	98.39
T105-38	0.01	2.05	21.13	35.28	4.85	0.02	0.00	1.73	33.48	98.54
T105-39	0.01	1.80	21.17	35.60	5.90	0.06	0.02	1.81	32.09	98.46
T105-40	0.00	1.58	21.22	35.41	6.64	0.01	0.00	1.99	31.73	98.57
T105-41	0.03	1.38	21.21	35.62	6.86	0.05	0.04	2.28	32.00	99.47
T105-42	0.00	1.41	21.39	35.77	6.91	0.06	0.00	2.32	31.29	99.15
T105-43	0.01	2.29	21.38	36.13	4.88	0.00	0.01	1.54	32.84	99.09
T105-44	0.02	2.52	21.67	35.99	4.16	0.01	0.01	1.47	33.96	99.81
T105-45	0.02	2.67	21.51	36.32	3.37	0.02	0.04	1.52	34.25	99.72
T105-46	0.02	2.69	21.48	35.84	3.37	0.02	0.02	1.42	34.49	99.34
T105-47	0.01	2.56	21.40	36.32	3.95	0.05	0.00	1.40	34.18	99.86
T105-48	0.00	2.45	21.24	35.85	3.04	0.01	0.01	1.88	34.22	98.69
T105-49	0.00	2.50	21.31	36.28	2.81	0.02	0.02	1.94	34.14	99.01
T105-50	0.00	2.51	21.57	36.33	2.59	0.03	0.00	2.13	34.80	99.96
T105-51	0.02	2.11	21.44	35.93	7.06	0.03	0.03	0.00	32.22	98.83
T105-52	0.00	2.06	21.30	35.73	6.61	0.04	0.01	0.03	33.08	98.86
T105-53	0.00	2.11	21.23	35.61	5.34	0.01	0.01	0.12	34.01	98.44
T105-54	0.00	1.77	21.13	34.86	5.77	0.04	0.03	0.17	33.82	97.60

	Na_2O	MgO	Al_2O_3	SiO_2	CaO	TiO_2	Cr_2O_3	MnO	FeO	Total
T105-55	0.00	1.77	21.10	35.64	5.59	0.04	0.02	0.17	33.90	98.22
T105-56	0.00	1.53	21.05	34.48	5.97	0.05	0.00	0.18	34.14	97.41
T105-57	0.00	1.24	21.01	34.99	6.79	0.04	0.00	0.22	33.48	97.76
T105-58	0.01	1.10	20.70	34.44	6.70	0.10	0.00	0.30	33.91	97.26
T105-59	0.01	1.17	20.81	34.59	6.86	0.06	0.03	0.34	33.44	97.32
T105-60	0.00	1.39	20.80	34.35	6.01	0.02	0.01	0.14	33.81	96.54
T105-61	0.02	1.51	20.78	34.62	6.23	0.07	0.02	0.14	33.59	96.96
T105-62	0.00	1.85	20.62	33.58	5.55	0.02	0.01	0.11	33.61	95.36
T105-63	0.02	1.87	20.73	33.79	5.51	0.05	0.00	0.14	33.88	95.98
T105-64	0.00	1.92	20.64	33.53	5.81	0.00	0.00	0.14	33.14	95.17
T105-65	0.02	2.10	20.05	33.01	5.10	0.77	0.00	0.08	32.81	93.94
T105-66	0.00	2.33	20.57	33.35	3.69	0.00	0.00	0.09	34.50	94.53
N102-67	0.00	2.05	20.82	34.52	2.93	0.01	0.00	0.23	36.86	97.41
N102-68	0.02	2.25	20.81	34.17	3.37	0.00	0.01	0.15	35.36	96.16
N102-69	0.00	2.19	21.18	35.00	6.16	0.03	0.05	0.09	33.06	97.76
N102-70	0.00	1.84	20.93	34.37	5.99	0.03	0.04	0.12	33.36	96.67
N102-71	0.00	1.85	20.93	34.56	5.56	0.02	0.00	0.15	33.66	96.74
N102-72	0.00	1.51	21.05	34.17	6.43	0.05	0.00	0.16	33.68	97.05
N102-73	0.00	1.18	20.77	34.61	6.76	0.05	0.01	0.36	33.11	96.84
N102-74	0.00	1.09	20.79	34.24	6.20	0.03	0.02	0.30	34.27	96.94
N102-75	0.02	1.15	20.63	34.60	6.54	0.08	0.02	0.29	33.70	97.03
N102-76	0.02	1.18	20.69	34.11	6.85	0.06	0.01	0.30	33.33	96.56
N102-77	0.00	1.58	20.96	34.72	6.11	0.03	0.02	0.23	33.86	97.50
N102-78	0.01	2.37	20.73	34.67	3.89	0.16	0.02	0.08	34.71	96.64
N102-79	0.00	2.24	20.95	34.86	3.85	0.00	0.02	0.22	35.11	97.26
N102-80	0.00	2.33	20.70	34.02	3.33	0.01	0.00	0.20	35.15	95.74
N102-81	0.02	2.22	20.64	34.14	4.39	0.00	0.00	0.12	34.22	95.75
N102-82	0.00	2.05	20.91	34.27	5.36	0.01	0.06	0.12	34.02	96.80
N102-83	0.02	1.88	20.80	34.54	4.90	0.07	0.00	0.17	34.76	97.13
N102-84	0.00	1.74	20.75	34.11	5.14	0.03	0.02	0.18	34.48	96.45
N102-85	0.03	1.62	20.94	34.86	5.99	0.05	0.00	0.15	34.09	97.73
N102-86	0.00	1.51	20.76	34.55	6.12	0.06	0.02	0.21	34.17	97.41
N102-87	0.02	1.16	15.31	22.41	3.33	0.03	0.00	0.09	25.38	67.74
N102-88	0.02	1.54	20.93	34.84	5.60	0.04	0.01	0.11	34.68	97.77
N102-89	0.01	1.64	20.89	35.18	5.28	0.02	0.02	0.20	34.91	98.15
N102-90	0.01	1.61	21.05	35.12	5.66	0.04	0.02	0.19	34.56	98.26
N102-91	0.00	2.19	21.42	35.86	5.60	0.04	0.05	0.05	34.08	99.29
N102-92	0.00	2.42	21.15	35.54	4.93	0.21	0.00	0.05	33.97	98.28
N102-93	0.02	2.25	21.44	36.15	5.84	0.02	0.00	0.03	33.72	99.46
N102-94	0.00	2.25	21.44	36.18	6.33	0.02	0.04	0.02	32.97	99.25
N102-95	0.00	2.17	21.50	36.34	6.66	0.06	0.05	0.04	32.59	99.42
N102-96	0.02	2.35	21.09	34.97	6.44	0.05	0.04	0.07	32.39	97.42
N102-97	0.02	2.17	21.24	35.40	6.82	0.07	0.04	0.01	32.31	98.08
N102-98	0.01	2.11	21.18	34.65	6.89	0.06	0.03	0.04	32.19	97.15
N102-99	0.01	1.83	20.94	34.91	5.52	0.02	0.00	0.09	34.39	97.72
N102-100	0.00	1.49	20.97	34.58	6.23	0.05	0.03	0.18	33.88	97.42
N102-101	0.00	1.40	20.75	34.57	5.87	0.05	0.00	0.26	34.05	96.95
N102-102	0.01	1.29	20.80	34.99	5.65	0.05	0.03	0.43	34.70	97.94
N102-103	0.02	1.14	20.93	34.56	5.20	0.05	0.02	0.74	35.20	97.86

	Na_2O	MgO	Al_2O_3	SiO_2	CaO	TiO_2	Cr_2O_3	MnO	FeO	Total
N102-104	0.00	1.11	20.81	34.34	5.34	0.02	0.05	0.81	35.17	97.65
N102-105	0.01	1.06	20.99	34.81	5.72	0.01	0.02	1.01	34.33	97.97
N102-106	0.00	1.40	20.85	34.88	4.71	0.05	0.04	0.87	35.31	98.10
N102-107	0.00	2.05	20.87	35.02	3.73	0.01	0.03	0.47	35.72	97.91
N102-108	0.00	2.38	20.99	34.78	3.40	0.01	0.00	0.25	35.49	97.30
N102-109	0.02	2.39	21.07	35.15	3.25	0.01	0.09	0.27	35.55	97.81

Table C.3. Biotite data from UBC microprobe.

	Na_2O	MgO	Al_2O_3	SiO_2	K_2O	CaO	TiO_2	Cr_2O_3	MnO	FeO	F	Total
N38-3	2.00	10.31	31.02	37.66	0.01	1.26	0.84	0.03	0.04	3.61	0.17	86.95
N38-4	2.09	10.56	30.56	37.56	0.02	1.44	0.75	0.03	0.07	3.60	0.54	87.21
N38-5	2.00	6.70	31.14	36.82	0.00	1.12	0.86	0.03	0.07	7.86	0.32	86.92
N38-6	0.74	2.01	11.79	77.31	0.01	0.19	0.38	0.01	0.04	3.87	0.17	96.53
N38-7	1.86	5.57	31.58	36.37	0.01	0.63	0.99	0.03	0.14	9.77	0.34	87.27
N38-8	0.21	7.84	18.88	34.43	8.58	0.03	1.71	0.08	0.02	22.13	0.35	94.25
N38-9	0.23	7.54	18.79	34.23	8.57	0.02	1.61	0.04	0.05	22.14	0.40	93.61
N38-10	0.25	7.33	18.61	34.18	8.53	0.01	1.69	0.09	0.02	21.92	0.42	93.04
N38-11	0.24	7.34	19.38	33.74	8.39	0.04	1.68	0.04	0.00	22.20	0.28	93.33
N38-12	0.21	7.21	18.59	33.51	8.12	0.02	1.30	0.07	0.00	23.47	0.27	92.78
N38-13	0.22	7.77	18.54	33.62	8.56	0.03	1.80	0.08	0.00	21.68	0.35	92.65
N38-14	0.24	7.90	18.75	33.54	8.43	0.01	1.88	0.05	0.01	21.91	0.41	93.12
N38-15	0.26	7.75	18.86	33.71	8.48	0.00	1.85	0.00	0.00	21.75	0.26	92.92
N38-16	0.26	7.81	18.88	33.63	8.62	0.01	1.93	0.02	0.04	21.80	0.38	93.37
N38-17	0.15	8.12	18.92	32.62	7.89	0.00	1.79	0.02	0.00	23.03	0.38	92.93
N38-18	0.21	7.71	18.67	33.75	8.70	0.05	1.89	0.03	0.02	21.71	0.52	93.25
N38-19	0.13	9.00	19.42	30.54	6.03	0.01	1.57	0.02	0.03	23.86	0.39	91.00
N38-20	0.23	8.13	19.01	33.09	8.28	0.01	1.82	0.05	0.04	21.55	0.46	92.67
N38-21	0.20	7.62	18.72	33.34	8.42	0.03	1.95	0.03	0.03	21.78	0.23	92.36
N38-22	0.49	7.45	18.47	34.87	7.43	0.27	1.95	0.06	0.00	21.29	0.20	92.48
N38-23	1.74	6.79	20.69	35.83	0.23	1.08	0.05	0.04	0.00	22.28	0.09	88.81
N38-24	0.10	6.89	16.17	44.21	0.23	0.20	0.06	0.05	0.00	22.43	0.02	90.37
N38-25	1.18	6.31	21.74	30.73	0.28	1.35	0.15	0.08	0.15	26.82	0.00	88.80
N38-26	1.08	0.41	33.40	49.17	8.80	0.16	0.21	0.05	0.00	1.15	0.17	94.60
N38-27	1.00	0.47	35.60	46.24	9.44	0.06	0.21	0.06	0.00	1.18	0.04	94.30
N38-28	0.93	0.49	35.66	46.00	9.76	0.03	0.24	0.02	0.06	1.25	0.07	94.53
N38-29	0.98	0.47	35.57	45.76	9.39	0.01	0.22	0.06	0.00	1.29	0.17	93.93
N38-30	0.93	0.42	34.41	46.63	9.50	0.03	0.23	0.04	0.00	1.38	0.02	93.61
N38-31	1.14	0.44	33.34	48.18	8.89	0.17	0.19	0.03	0.03	1.72	0.07	94.22
N38-32	0.28	7.71	19.78	35.68	8.56	0.09	1.57	0.07	0.00	21.10	0.50	95.35
N38-33	0.24	7.71	19.23	34.54	8.30	0.11	1.53	0.04	0.03	21.72	0.32	93.76
N38-34	0.27	7.73	18.89	34.49	8.29	0.08	1.49	0.03	0.04	21.48	0.35	93.15
N38-35	0.28	7.70	18.97	34.37	8.01	0.16	1.60	0.04	0.01	21.56	0.28	92.98
N38-36	0.28	7.90	19.07	34.43	8.17	0.11	1.54	0.05	0.00	21.87	0.41	93.84
N38-37	0.29	7.74	19.15	34.87	8.80	0.06	1.55	0.06	0.00	20.74	0.50	93.77
N38-38	0.19	7.66	19.13	34.07	7.80	0.11	1.61	0.08	0.05	21.59	0.33	92.62
N38-39	0.25	7.66	19.27	35.01	8.68	0.11	1.66	0.06	0.00	20.70	0.39	93.79
N38-40	0.33	7.60	19.30	35.06	8.53	0.10	1.74	0.06	0.01	20.94	0.44	94.10
T105-1	0.17	7.32	18.18	34.66	9.10	0.02	2.89	0.01	0.08	21.95	0.42	94.80
T105-2	0.17	7.57	18.70	34.75	9.29	0.03	2.83	0.03	0.06	21.63	0.44	95.49
T105-3	0.16	7.44	18.84	34.84	9.19	0.01	2.97	0.00	0.07	21.37	0.32	95.20
T105-4	0.17	7.43	18.64	34.88	9.14	0.00	2.84	0.05	0.04	21.79	0.31	95.30
T105-5	0.17	7.44	18.97	35.29	9.28	0.02	2.82	0.02	0.05	21.53	0.36	95.95
T105-6	0.18	7.57	18.86	35.08	9.37	0.00	2.82	0.03	0.06	21.43	0.47	95.87
T105-7	0.12	7.44	18.89	34.96	9.19	0.03	2.60	0.04	0.08	21.04	0.25	94.64
T105-8	0.15	7.69	19.04	34.82	9.02	0.00	2.02	0.00	0.08	21.07	0.36	94.27
T105-9	0.22	7.04	17.57	34.41	8.51	0.21	2.10	0.06	0.28	20.64	0.28	91.33

	Na_2O	MgO	Al_2O_3	SiO_2	K_2O	CaO	TiO_2	Cr_2O_3	MnO	FeO	F	Total
T105-11	0.24	7.17	18.40	34.62	8.97	0.09	2.57	0.06	0.20	21.13	0.34	93.79
T105-12	0.21	7.03	18.50	33.69	9.20	0.09	2.95	0.02	0.09	20.64	0.32	92.74
T105-13	0.14	7.61	18.71	35.25	9.44	0.02	2.77	0.03	0.02	21.03	0.35	95.38
T105-14	0.12	7.52	18.70	35.57	9.30	0.00	2.97	0.00	0.08	21.35	0.26	95.89
T105-15	0.13	7.62	18.46	35.27	9.40	0.01	2.97	0.00	0.09	22.12	0.39	96.48
T105-16	0.13	7.47	18.40	34.94	9.23	0.00	2.95	0.04	0.07	21.66	0.24	95.13
T105-17	0.10	7.53	18.70	35.43	9.31	0.02	2.89	0.01	0.03	21.68	0.36	96.06
T105-18	0.56	0.57	34.78	45.81	10.27	0.01	0.84	0.02	0.00	1.46	0.17	94.48
T105-20	0.14	7.83	18.80	35.13	9.19	0.02	2.02	0.00	0.04	21.57	0.27	95.01
T105-21	0.15	7.29	19.19	34.95	9.16	0.03	2.46	0.04	0.06	21.82	0.42	95.56
T105-22	0.14	7.50	19.08	34.52	9.26	0.00	2.48	0.07	0.10	21.89	0.25	95.30
T105-24	0.12	7.61	18.90	34.77	9.33	0.02	2.41	0.05	0.04	21.83	0.36	95.43
T105-25	0.15	7.54	19.36	35.20	9.33	0.03	2.30	0.06	0.09	21.05	0.33	95.45
T105-27	0.15	7.61	19.33	35.34	9.25	0.02	2.35	0.02	0.09	20.72	0.15	95.02
T105-29	0.14	7.59	19.15	35.39	9.26	0.02	2.41	0.04	0.05	21.42	0.33	95.79
T105-30	0.13	7.37	19.26	35.51	9.12	0.02	2.35	0.03	0.09	20.94	0.38	95.20
T105-32	0.17	7.53	19.35	34.90	9.33	0.04	2.33	0.00	0.09	21.03	0.32	95.10
T105-33	0.00	1.94	20.91	37.68	0.02	4.09	0.06	0.00	2.46	32.64	0.00	99.80
T105-34	0.16	7.37	19.60	35.53	9.22	0.02	2.45	0.03	0.06	20.62	0.31	95.37
T105-35	0.15	7.53	19.41	35.52	9.23	0.00	2.45	0.04	0.02	21.29	0.25	95.88
T105-36	0.14	7.52	19.50	35.47	9.18	0.01	2.41	0.04	0.06	21.30	0.32	95.95
T105-39	0.18	7.03	21.33	35.98	8.81	0.02	2.23	0.00	0.10	20.20	0.29	96.15
T105-40	0.17	7.51	19.41	35.45	9.18	0.04	2.35	0.02	0.08	21.43	0.30	95.93
T105-42	0.17	7.85	19.01	34.77	8.95	0.01	2.30	0.00	0.05	21.45	0.18	94.74
T105-44	0.17	7.91	19.08	35.39	9.26	0.00	2.30	0.03	0.10	20.78	0.38	95.40
T105-45	0.16	8.12	19.03	35.32	9.18	0.03	2.23	0.00	0.06	21.27	0.41	95.80
T105-46	0.18	8.24	19.00	35.09	9.04	0.02	2.07	0.01	0.09	20.74	0.39	94.87
T105-48	0.16	8.20	18.91	35.26	9.01	0.03	2.26	0.01	0.09	21.06	0.30	95.29
T105-49	0.13	7.76	19.14	35.24	9.27	0.03	2.45	0.00	0.09	21.27	0.22	95.59
T105-50	0.15	7.66	18.80	34.92	9.26	0.00	2.47	0.00	0.12	21.28	0.33	95.02
N102-51	0.13	7.65	18.83	34.89	9.29	0.00	2.72	0.00	0.06	21.52	0.39	95.47
N102-52	0.14	7.67	19.01	35.33	9.33	0.01	2.66	0.02	0.07	21.06	0.36	95.66
N102-53	0.17	7.74	18.86	35.05	9.37	0.02	2.65	0.01	0.05	21.19	0.25	95.35
N102-54	0.16	7.59	18.95	35.38	9.26	0.03	2.60	0.00	0.00	20.96	0.23	95.16
N102-55	0.11	7.64	19.00	35.27	9.43	0.00	2.63	0.00	0.09	20.71	0.40	95.27
N102-56	0.20	7.57	18.63	35.58	9.04	0.03	3.02	0.02	0.05	21.07	0.23	95.44
N102-57	0.21	7.39	18.46	35.08	9.01	0.06	2.93	0.05	0.09	21.85	0.27	95.40
N102-58	0.23	7.13	18.25	34.68	9.03	0.10	2.93	0.03	0.18	21.00	0.32	93.86
N102-59	0.20	7.22	18.27	34.75	8.87	0.06	2.96	0.02	0.09	21.29	0.37	94.10
N102-60	0.19	7.27	18.42	34.78	9.17	0.05	3.03	0.00	0.11	21.71	0.30	95.03
N102-61	0.19	7.27	18.25	34.83	9.18	0.06	3.00	0.05	0.11	21.38	0.22	94.53
N102-62	0.17	7.52	18.84	35.46	9.12	0.04	3.07	0.05	0.08	20.93	0.29	95.57
N102-63	0.17	7.41	18.69	35.21	9.19	0.01	3.04	0.03	0.10	21.38	0.20	95.42
N102-64	0.19	7.39	18.78	35.15	9.11	0.02	3.07	0.06	0.07	21.24	0.36	95.44
N102-65	0.19	7.36	18.64	35.52	9.10	0.03	3.19	0.00	0.05	21.42	0.28	95.78
N102-66	0.17	7.39	18.55	35.47	9.15	0.05	3.21	0.04	0.02	21.06	0.35	95.45
N102-67	0.13	6.32	18.66	34.63	9.06	0.03	2.72	0.03	0.01	22.99	0.32	94.90
N102-68	0.17	6.34	18.74	34.67	9.31	0.04	2.84	0.03	0.01	23.03	0.30	95.48
N102-69	0.16	6.29	18.62	34.90	9.25	0.03	2.76	0.00	0.04	22.94	0.52	95.52

	Na_2O	MgO	Al_2O_3	SiO_2	K_2O	CaO	TiO_2	Cr_2O_3	MnO	FeO	F	Total
N102-70	0.16	6.49	18.64	34.88	9.28	0.00	2.78	0.04	0.02	23.44	0.28	96.02
N102-71	0.16	6.44	18.62	34.93	9.08	0.02	2.73	0.02	0.00	22.96	0.31	95.26
N102-72	0.12	6.33	18.84	35.09	9.13	0.02	2.83	0.03	0.00	22.49	0.37	95.26
N102-73	0.17	6.45	18.74	34.69	9.19	0.02	2.59	0.01	0.03	22.88	0.37	95.15
N102-74	0.15	6.47	18.58	34.88	9.35	0.03	2.65	0.06	0.05	22.88	0.22	95.31
N102-75	0.16	6.36	18.90	34.66	9.22	0.02	2.74	0.06	0.01	23.09	0.29	95.52
N102-76	0.10	6.42	18.64	34.82	9.13	0.03	2.77	0.00	0.00	22.85	0.23	94.99
N102-77	0.17	6.30	18.63	34.44	9.23	0.03	2.87	0.00	0.00	22.73	0.19	94.59
N102-78	0.12	6.37	18.63	34.34	9.19	0.01	2.89	0.00	0.03	23.16	0.25	95.00
N102-79	0.13	6.34	18.48	34.64	9.32	0.02	2.92	0.04	0.00	23.47	0.18	95.52
N102-80	0.16	6.41	18.69	34.31	9.24	0.03	2.86	0.04	0.00	23.01	0.37	95.11
N102-82	0.12	6.39	18.25	34.16	9.15	0.02	2.96	0.02	0.04	23.21	0.26	94.58
N102-83	0.12	6.44	18.52	35.04	9.43	0.00	2.89	0.03	0.00	22.94	0.35	95.77
N102-84	0.12	6.38	18.28	34.68	9.48	0.00	2.98	0.00	0.00	22.79	0.34	95.05
N102-85	0.10	6.34	18.38	34.78	9.39	0.00	2.90	0.07	0.03	22.98	0.28	95.26
N102-86	0.12	6.47	18.58	34.87	9.30	0.01	2.90	0.05	0.00	22.97	0.27	95.53
N102-87	0.13	6.39	18.52	34.48	9.28	0.00	2.91	0.00	0.00	23.02	0.31	95.05
N102-88	0.12	6.39	18.46	34.67	9.19	0.00	2.92	0.02	0.00	22.83	0.31	94.90
N102-89	0.15	6.36	18.71	34.82	9.23	0.03	2.87	0.00	0.03	22.62	0.30	95.11
N102-90	0.12	7.78	21.11	23.86	0.04	0.30	0.25	0.00	0.01	33.92	0.00	87.38
N102-95	0.15	7.56	19.67	23.47	0.02	0.36	0.32	0.04	0.05	32.81	0.04	84.49
N102-98	0.25	6.06	18.98	34.13	8.97	0.12	2.58	0.02	0.00	23.06	0.18	94.34
N102-99	0.22	6.26	18.92	34.14	8.76	0.13	2.79	0.05	0.03	23.39	0.24	94.93
N102-100	0.27	6.16	19.07	34.51	8.94	0.15	2.70	0.02	0.02	23.41	0.29	95.53
N102-101	0.10	7.01	18.65	33.92	8.80	0.01	2.05	0.02	0.02	23.71	0.27	94.57
N102-103	0.10	6.73	18.47	34.18	8.61	0.01	2.23	0.00	0.02	24.17	0.26	94.78
N102-104	0.06	7.77	18.57	32.32	6.93	0.01	1.87	0.00	0.00	24.86	0.24	92.65
N102-105	0.10	6.48	18.38	34.83	9.29	0.00	2.58	0.03	0.00	23.26	0.27	95.23
N102-106	0.13	6.49	18.37	34.73	9.14	0.01	2.59	0.06	0.00	23.46	0.34	95.34
N102-107	0.12	6.33	18.33	34.03	8.69	0.02	2.81	0.09	0.02	23.52	0.22	94.18
N102-108	0.08	6.43	18.39	34.40	9.08	0.00	2.63	0.04	0.01	23.86	0.29	95.20
N102-109	0.08	6.33	18.77	34.75	9.33	0.03	2.82	0.03	0.04	23.29	0.36	95.82
N102-112	0.10	6.36	18.41	34.37	9.29	0.00	2.75	0.01	0.04	23.50	0.27	95.10
N102-113	0.10	6.48	18.47	34.52	9.19	0.03	2.65	0.04	0.00	23.39	0.14	95.02
N102-114	0.58	0.53	35.14	45.95	10.71	0.01	0.70	0.02	0.02	1.62	0.10	95.38
N102-119	0.09	6.45	18.21	33.98	9.37	0.02	2.64	0.00	0.01	23.67	0.30	94.75
N102-120	0.12	6.69	18.20	34.31	9.04	0.02	2.48	0.01	0.02	23.22	0.25	94.36
N102-121	0.08	7.30	18.39	33.66	8.49	0.02	2.49	0.06	0.00	23.73	0.29	94.52
N102-122	0.10	6.63	18.19	34.57	9.26	0.00	2.77	0.07	0.00	23.12	0.22	94.94
N102-123	0.12	6.78	18.24	35.10	9.48	0.01	2.84	0.00	0.00	23.38	0.40	96.36
N102-124	0.14	6.56	18.24	35.08	9.16	0.01	2.82	0.00	0.01	23.46	0.36	95.84
N102-125	0.10	6.63	18.31	34.61	9.27	0.00	2.48	0.03	0.00	22.71	0.29	94.42
N102-126	0.14	6.59	18.10	35.00	9.16	0.00	2.85	0.01	0.02	23.50	0.39	95.76
N102-127	0.11	6.58	18.06	34.53	9.31	0.00	2.83	0.04	0.00	23.35	0.35	95.14
N102-128	0.11	6.87	18.39	34.56	9.28	0.01	2.64	0.06	0.00	23.29	0.31	95.52
N102-129	0.17	6.59	18.54	34.42	9.12	0.01	2.63	0.05	0.00	23.16	0.24	94.95
N102-130	0.15	6.75	18.82	34.41	9.23	0.00	2.31	0.03	0.00	23.26	0.23	95.19
N102-131	0.13	6.62	18.46	34.18	9.26	0.02	2.79	0.04	0.04	23.54	0.14	95.21
N102-132	0.13	6.71	18.23	33.65	8.72	0.00	2.79	0.04	0.04	23.76	0.17	94.24

End Member Compositions

The garnets were characterised by calculating the end member compositions of each point along a traverse and then plotting these points. The methodology is summarized below and in Table C.4.

Methodology:

1. Molecular proportion of oxides = weight % oxide/molecular weight
2. Atomic proportion of oxides = molecular proportion of oxides * number of oxygens
3. Atomic proportion of cations = molecular proportion of oxides * number of cations
4. Number of cations in formula = atomic proportion of cations * conversion factor [conversion factor = 24/(sum of all atomic proportions of cations)]. Fe_2O_3* is calculated by assuming total oxide is 100%; Fe_2O_3* = (100% -total %). This is an iterative process but in most cases the first iteration yielded reasonable results and oxide totals approaching 100% (see Total*).
5. End member calculation followed methodology of Deer et al. (1992).

Table C.4. Example of end member calculation.

T105-44	Na_2O	MgO	Al_2O_3	SiO_2	CaO	TiO_2	Cr_2O_3	MnO	FeO	Total	Fe_2O_3*	FeO*	Total*	
Weight % of oxide	0.02	2.52	21.6	35.9	4.16	0.01	0.01	1.47	33.9	99.8	0.1533	33.8	99.90	
Formula weight of oxide	61.98	40.3	101	60.0	56.07	79.88	152	70.9	71.9		159	71.8		
1. Molecular proportion	0	0.06	0.21	0.59	0.074	9 E-05	0	0.02	0.47		0.001	0.47		
2. Oxides	0	0.06	0.63	1.19	0.074	0.0001	0	0.02	0.47		0.0029	0.47	Con.	9.725
3. Cations	0	0.06	0.42	0.59	0.074	9 E-05	0	0.02	0.47		0.0019	0.47	A site	6.118
4. Cations in formula	0	0.60	4.13	5.82	0.721	0.0009	0	0.20	4.6		0.0188	4.58	B site	3.979
													T site	6
5. End members	Prp	Adr	Alm	Uva	Sps	Grs	Total							
	9.95	0.46	75.1	0.00	3.30	11.33	100							

Ferry and Spear (1978) method

Various garnet biotite-pairs were analysed using the original methodology of Ferry and Spear (1978). This is summarised below and using Table C.5. The results of these calculations (Table C.6) can by compared to analysis using TWEEQU (Figure 4.3).

Methodology (for T-105 pair 1):

1. Calculate mean Mg/Fe for chosen garnet and biotite.
2. Calculate k = $(Mg/Fe)_{Grt}/(Mg/Fe)_{Bt}$
3. Calculate temperature (K) = 2109/(0.782 – *ln*k).

Table C.5. Example calculation using Ferry and Spear (1978) methodology.

1. Adjacent biotite (T-105 25-32) and garnet traverse (T-105 37-46)					
Garnet			Biotite		
Mg	Fe	Mg/Fe	Mg	Fe	Mg/Fe
2.50	33.77	0.074	7.54	21.05	0.36
2.05	33.48	0.061	7.61	20.72	0.37
1.80	32.09	0.056	7.59	21.42	0.35
1.58	31.73	0.05	7.37	20.94	0.35
1.38	32.00	0.043	7.53	21.03	0.36
1.41	31.29	0.045	2. Mean Bt =		0.36
2.67	34.25	0.078			
2.69	34.49	0.078			
2.56	34.18	0.075			
2. Mean Grt =		0.066			
3. k =		0.18			
4. T (K)		852.0			
T (°C)		578. 5			

Table C.6. Results from calculation using Ferry and Spear (1978).

Garnet – biotite pair	T (°C) (Ferry and Spear 1978)	T (°C) TWEEQU(Berman 1991)
T-105 pair 1	578.5	570
pair 2	585.8	650
pair 3	555.8	610
N-38 pair 1	452.0	490
pair 2	463.9	520
pair 3	447.0	490

REFERENCE LIST

Arita, K. 1983. Origin of the inverted metamorphism of the lower Himalayas, central Nepal. Tectonophysics, **95**:43-60.

Berman, R.G. 1990. Mixing properties of Ca-Mg-Fe-Mn garnets. American Mineralogist, **75**:328-344.

Berman, R.G. 1991. Thermobarometry using multi-equilibration calculations: a new technique, with petrological applications. Canadian Mineralogist, **29**:833-855.

Bordet, P., Colchen, and Le Fort, P. 1975. Recherches géologiques dans l'Himalaya du Népal: région du Nyi-Shang. Centre National de la Recherche Scientifique, Paris, France.

Bouchez, J.L., and Pêcher, A. 1981. The Himalayan Main Central thrust pile and its quartz-rich tectonites in central Nepal. Tectonophysics, **78**:23-50.

Brown, R.L., Journeay, J.M., Lane, L.S., Murphy, D.C., and Rees, C.J. 1986. Obduction, backfolding and piggyback thrusting in the metamorphic hinterland of southeastern Canadian Cordillera. Journal of Structural Geology, **8**:255-268.

Brown, R.L., and Nazarchuk, J.H. 1993: Annapurna detachment fault in the Greater Himalaya of central Nepal. *In* Himalayan Tectonics. *Edited by* P.J. Treloar and M.P. Searle, Geological Society Special Publication 74, pp. 461-473.

Brunel, M. 1986. Ductile thrusting in the Himalayas: shear sense criteria and stretching lineations. Tectonics, **5**:247-265.

Burchfiel, B.C., Chen, Z., Hodges, K.V., Liu, Y., Royden, L.H., Deng, C., and Xu, J. 1992. The South Tibetan Detachment System, Himalaya Orogen: Extension contemporaneous with and parallel to shortening in a collisional mountain belt. Geological Society of America Special Paper 269, pp. 41,

Burchfiel, B.C., and Royden, L.H. 1985. North-south extension within the convergent Himalayan region. Geology, **13**:679-682.

Colchen, M., Le Fort, P., and Pêcher, A. 1986. Annapurna-Manaslu-Ganesh Himal. Centre National de la Recherche Scientifique, Paris.

Coleman, M., and Hodges, K. 1995. Evidence for Tibetan plateau uplift before 14 Myr ago from a new minimum age for east-west extension. Nature, **374**:49-52.

Coleman, M.E. 1996. Orogen-parallel and orogen-perpendicular extension in the central Nepalese Himalayas. Geological Society of America Bulletin, **108**:1594-1607.

Coleman, M.E. 1998. U-Pb constraints on Oligocene-Miocene deformation and anatexis within the central Himalaya, Marsyandi valley, Nepal. American Journal of Science, **298**:553-571.

Coleman, M.E., and Hodges, K.V. 1998. Contrasting Oligocene and Miocene thermal histories from the hanging wall and footwall of the South Tibetan detachment in the central Himalaya from 40Ar/39Ar thermochronology, Marsyandi valley, central Nepal. Tectonics, **17**:726-740.

Copeland, P., Harrison, T.M., Hodges, K.V., Maruéjol, P., LeFort, P., and Pêcher, A. 1991. An Early Pliocene thermal disturbance of the Main Central Thrust, central Nepal: Implications for Himalayan tectonics. Journal of Geophysical Research, **96**:8475-8500.

Davis, G.H., and Reynolds, S.J. 1996. Structural geology of rocks and regions. John Wiley and Sons, New York.

Deer, W.A., Howie, R.A., and Zussman, J. 1992. An introduction to the rock-forming minerals. Longman, Essex.

Essene, E.J. 1982. Geologic thermometry and barometry. Reviews of Mineralogy, **10**:153-206.

Ferry, J.M., and Spear, F.S. 1978. Experimental calibration fo the partitioning of Fe and Mg between biotite and garnet. Contributions to Mineralogy and Petrology, **66**:113-117.

Gansser, A. 1964. Geology of the Himalayas. John Wiley and Sons, London, pp. 289.

Garzanti, E. 1999. Stratigraphy and sedimentary history of the Nepal Tethys Himalaya passive margin. Journal of Asian Earth Sciences, **17**:805-827.

Garzanti, E., Gorza, M., Martellini, L., and Nicora, A. 1994. Transition from diagenesis to metamorphism in the Paleozoic to Mesozoic succession of the Dolpo-Manang Synclinorium and Thakkhola graben (Nepal Tethys Himalaya). Eclogae Geologicae Helvetica, **87**:613-632.

Ghent, E.D. 1976. Plagioclase-garnet-Al_2SiO_4-quartz: a potential geobarometer-geothermometer. American Mineralogist, **61**:710-714.

Ghent, E.D., and Stout, M.Z. 1981. Geobarometry and geothermometry of plagioclase-biotite-garnet-muscovite assemblages. Contribution to Mineralogy and Petrology, **76**:92-97.

Godin, L. 2001. The Chako dome: an enigmatic structure in the hanging wall of the South Tibetan detachment, Nar valley, central Nepal. Journal of Asian Earth Sciences, **19**:22-23.

Godin, L. 2003. Structural evolution of the Tethyan sedimentary sequence, central Nepal Himalaya. Journal of Asian Earth Sciences, **in press**

Godin, L., Brown, R.L., and Hanmer, S. 1999a: High strain zone in the hanging wall of the Annapurna detachment, central Nepal Himalaya. *In* Himalaya and Tibet: Mountain roots to mountain tops. *Edited by* A.M. Macfarlane, Sorkhabi, R. and Quade, J., Geological Society of America Special Paper 328, pp. 199-210.

Godin, L., Brown, R.L., Hanmer, S., and Parrish, R. 1999b. Backfolds in the core of the Himalayan orogen: An alternative interpretation. Geology, **27**:151-154.

Godin, L., Parrish, R.R., Brown, R.L., and Hodges, K. 2001. Crustal thickening leading to exhumation of the metamorphic core of the central Nepal Himalaya: Insight from U-Pb geochronology and 40Ar/39Ar thermochronology. Tectonics, **20**:729-747.

Gradstein, F.M., von Rad, U., Gibling, M.R., Jansa, L.F., Kaminski, M.A., Kristiansen, I.-L., Ogg, J.G., Rohl, U., Sarti, M., Thorow, J.W., Westermann, G.E.G., and Wiedmann, J. 1992. The Mesozoic continental margin of central Nepal. Geologisches Jahrbuch, **77**

Grasemann, B., Fritz, H., and Vannay, J.-C. 1999. Quantitative kinematic flow analysis from the Main Central thrust zone (NW-Himalaya, India): implications for a decelerating strain path and the extrusion of orogenic wedges. Journal of Structural Geology, **21**:837-853.

Grujic, D., Casey, M., Davidson, C., Hollister, L.S., Kündic, R., Pavlis, T., and Schmid, S. 1996. Ductile extension of the Higher Himalayan Crystalline in Bhutan: evidence from quartz microfabrics. Tectonophysics, **260**:21-43.

Grujic, D., Hollister, L.S., and Parrish, R. 2002. Himalayan metamorphic sequence as an orogenic channel: insights from Bhutan. Earth and Planetary Science Letters, **198**:177-191.

Guillot, S., Cosca, M., Allemand, P., and Le Fort, P. 1999: Contrasting metamorphic and geochronologic evolution along the Himalayan belt. *In* Himalaya and Tibet: Mountain roots to mountain tops. *Edited by* A.M. Macfarlane, R. Sorkhabi and J. Quade, Geological Society of America Special Paper 328, pp. 117-128.

Guillot, S., Hodges, K., LeFort, P., and Pêcher, A. 1994. New constraints on the age of the Manaslu leucogranite: evidence for episodic tectonic denudation in the central Himalayas. Geology, **22**:559-562.

Hanes, J.A. 1991. K-Ar and 40Ar/39Ar Geochronology: Methods and Applications. *In* Short Course Handbook On Applications Of Radiogenic Isotope Systems To Problems In Geology. *Edited by* J.N. Ludden, Mineralogical Association of Canada, Toronto. pp. 27-57.

Hanmer, S. 1984. Strain insensitive foliations in polymineralic rocks. Canadian Journal of Earth Sciences, **21**:1410-1414.

Hanmer, S., and Passchier, C. 1991. Shear-sense indicators: a review. Geological Survey of Canada Paper 90-17,

Harrison, T.M., Grove, M., McKeegan, K.D., Coath, C.D., Lovera, O.M., and Le Fort, P. 1999. Origin and episodic emplacement of the Manaslu intrusive complex, central Himalaya. Journal of Petrology, **40**:3-19.

Hauck, M.L., Nelson, K.D., Brown, L.D., Zhao, W., and Ross, A.R. 1998. Crustal structure of the Himalayan orogen at ~90° east longitude from Project INDEPTH deep reflection profiles. Tectonics, **17**:481-500.

Hodges, K. 1991. Pressure-temperature-time paths. Annual Review of Earth and Planetary Sciences, **19**:207-236.

Hodges, K., and Crowley, P.D. 1985. Error estimation and empirical geothermobarometry for peletic systems. American Mineralogist, **70**:702-709.

Hodges, K.V. 2000. Tectonics of the Himalaya and southern Tibet from two perspectives. Geological Society of America Bulletin, **112**:324-350.

Hodges, K.V., Hubbard, M.S., and Silverberg, D.S. 1988. Metamorphic constraints on the thermal evolution of the central Himalayan Orogen. Philosophical Transactions of the Royal Society of London, **A326**:257-280.

Hodges, K.V., Parrish, R.R., and Searle, M.P. 1996. Tectonic evolution of the central Annapurna Range, Nepalese Himalayas. Tectonics, **15**:1264-1291.

Hubbard, M.S., and Harrison, T.M. 1989. $^{40}Ar/^{39}Ar$ age constraints on deformation and metamorphism in the Main Central Thrust Zone and Tibetan Slab, eastern Nepal Himalaya. Tectonics, **8**:865-880.

Johnson, M.C., and Rutherford, M.J. 1989. Experimental calibration of the aluminum-in hornblende geobarometer with application to Long Valley caldera (California) volcanic rocks. Geology, **17**:837-841.

Kretz, R. 1983. Symbols for rock-forming minerals. American Mineralogist, **68**:277-279.

Law, R.D. 2003: Strain, deformation temperatures and vorticity of flow at the top of the High Himalayan slab, Everest massif, Tibet. 18th Himalaya-Karakoram-Tibet Conference Abstracts Volume, Ascona, Switzerland 73-74.

LeFort, P. 1975. Himalayas: the collided range. Present knowledge of the continental arc. American Journal of Science, **275**:1-44.

LeFort, P., Guillot, S., and Pêcher, A. 1999: Une carte géologique de l'Himlung Himal, massif du Manaslu. *In* La Montagne et Alpinisme. *Edited by* Club alpin francais, Paris. pp. 22-27.

McMullin, D., Berman, R.G., and Greenwood, H.J. 1991. Calibration of the SGAM thermobarometer for pelitic rocks using data from phase equilibrium experiments and natural assemblages. Canadian Mineralogist, **29**:889-908.

Najman, Y., Pringle, M., Godin, L., and Oliver, G. 2001. Dating of the oldest continental sediments from the Himalayan foreland basin. Nature, **410**:194-197.

Passchier, C.W., and Trouw, R.A.J. 1998. Microtectonics. Springer, Berlin.

Schneider, C., and Masch, L. 1993: The metamorphism of the Tibetan Series from the Manang area, Marsyandi valley, central Nepal. *In* Himalayan Tectonics. *Edited by* P.J. Treloar and M.P. Searle, Geological Society Special Publication 74, pp. 357-374.

Searle, M.P., and Godin, L. 2003. The South Tibetan detachment system and the Manaslu leucogranite: a structural re-interpretation and restoration of the Annapurna - Manaslu Himalaya, Nepal. Journal of Geology, **111**:in press.

Searle, M.P., Waters, D.J., Rex, D.C., and Wilson, R.N. 1992. Pressure, temperature and time constraints on Himalayan metamorphism from eastern Kashmir and western Zanskar. Journal of the Geological Society, London, **149**:753-773.

Searle, M.P., Windley, B.F., Coward, M.P., Cooper, D.J.W., Rex, A.J., Rex, D., Tingdong, L., Xuchang, X., Jan, M.Q., Thakur, V.C., and Kumar, S. 1987. The closing of Tethys and the tectonics of the Himalaya. Geological Society of America Bulletin, **98**:678-701.

Spear, F.S. 1989: Relative thermobarometry and metamorphic P-T paths. *In* Evolution of Metamorphic Belts. *Edited by* J.S. Daly, R.A. Cliff and B.W. Yardley, Geological Society Special Publication 43, Oxford. pp. 63-81.

Spear, F.S., and Selverstone, J. 1983. QuantitativeP-T Paths from zoned minerals: theory and tectonic application. Contribution to Mineralogy and Petrology, **83**:348-357.

Stephenson, B.J., Searle, M.P., Waters, D.J., and Rex, D.C. 2001. Structure of the Main Central Thrust zone and extrusion of the High Himalayan deep crustal wedge, Kishtwar-Zanskar Himalaya. Journal of the Geological Society, London, **158**:637-652.

Vannay, J.-C., and Grasemann, B. 2001. Himalayan inverted metamorphism and syn-convergence extension as a consequence of a general shear extrusion. Geological Magazine, **138**:253-276.

Vannay, J.-C., and Hodges, K.V. 1996. Tectonometamorphic evolution of the Himalayan metamorphic core between the Annapurna and Dhaulagiri, central Nepal. Journal of Metamorphic Geology, **14**:635-656.

Weismayr, G., and Grasemann, B. 2002. Eohimalayan fold and thrust belt: Implications for the geodynamic evolution of the NW-Himalaya (India). Tectonics, **21**:8-1 - 8-18.

Worley, B., and Powell, R. 2000. High-precision relative thermobarometry: theory and a worked example. Journal of Metamorphic Geology, **18**:91-101.

Yardley, B.W. 1991. An introduction to metamorphic petrology. Longman Scientific and Technical, Essex.

Yin, A., and Harrison, T.M. 2000. Geologic evolution of the Himalayan-Tibetan orogen. Annual Reviews in Earth and Planetary Science, **28**:211-280.